BERGISCHE UNIVERSITÄT WUPPERTAL

Application of Density Functional Theory to Dye-sensitized Solar Cells and Hydroxyapatites

Dissertation

zur Erlangung des akademischen Grades
Doktor der Naturwissenschaften (Dr. rer. nat.)

vorgelegt von
Dejan Gemeri

Bergische Universität Wuppertal
Physikalische und Theoretische Chemie
unter der Anleitung von Prof. Dr. Hilke Bahmann

Wuppertal, 2024

To my brother, Dino.

Erklärung

Ich versichere, die Arbeit selbstständig verfasst zu haben, nur die in der Dissertation angegebenen Hilfsmittel benutzt und alle wörtlich oder inhaltlich übernommenen Stellen als solche gekennzeichnet zu haben, und dass die Dissertation in der gegenwärtigen oder einer anderen Fassung noch keiner anderen Fakultät, keiner Gesamthochschule und keiner anderen wissenschaftlichen Hochschule vorgelegen hat.

Wuppertal, 2024.   Dejan Gemeri

Acknowledgments

Almost three years ago, I left my home, family and secure job in order to pursue science and gather new knowledge. Here I am, at the end of this amazing journey, enriched with new experiences and I want to thank everyone who helped me along the way.

First and foremost, I would like to thank my mentor and supervisor, Hilke Bahmann. When I first came to Saarbrücken, I didn't know what to expect, being completely alone and you helped me to make that transition as painless as possible. You always made sure that I was well, have everything needed and that I could seek help and advice from you at any time. I learned a lot from you and still do. In addition to the great knowledge of DFT that I tried to absorb from you, you taught me that being nice to people in academia is far more important. At the end of the day, among all smart people in the room, kindness is the one that makes the difference. Please stay as you are and don't change too much.

Many thanks to my friend and colleague, Aleksandar Živković. Three months with you in the Netherlands helped me a lot at the very beginning of my PhD, especially with the technical details and how to be precise when using DFT. Our scientific discussions continue to this day and know that I appreciate them very much. For opening the door to electron dynamics, I would like to thank Jean Christophe Tremblay, I often say that you are my scientific role model, always calm and smiling. Helen King, for introducing the world of hydroxyapatites and great collaboration on the project. Tobias Henkes, for a valuable friendship that we maintain, even though we don't work together any more. Finally, I would like to thank the entire PTC group here in Wuppertal, not sure if I will ever be able to repay you for the warm welcome and all the help you gave me when I moved. Especially Robin and Niklas, I couldn't survive a day without you two.

Last but not least, thank you to my parents and brother, without your big support and faith, I wouldn't be able to achieve anything. Maja, as an already attached member of the family, you also sacrificed a lot for me, thank you for your patience and immense love. I am home now.

Summary

Dye-sensitized solar cells (DSSCs) represent a great challenge in the world of photovoltaics, both in experimental and theoretical domain. Their specific structure and the way of operating have been troubling scientists for almost three decades in order to find the best solutions. The most important thing is to find an overall efficiency of the solar cell as a combination of several factors which work together, like light harvesting, transport of electrons and holes, hybridization of the molecule-metal oxide interface, charge transfer behaviour from the dye to the conduction band (CB) of the semiconductor and lastly, the way in which the cell regenerates itself. To answer some of the mentioned issues, this cumulative thesis includes two published works in this area, focusing in the dye-semiconductor interface for a smoother transition. Density functional theory (DFT) and linear-response time-dependent density functional theory (LR-TDDFT) are the main methods to capture essential properties while studying systems separately (dye and semiconductor alone) and combined. Our focus goes beyond the standard and already known ruthenium complexes and it is directed towards organic dyes which are combined with titanium-dioxide (TiO_2) as a semiconductor. We looked into several typical D-π-A push-pull dyes, but also the ones with two donor groups (D-D-π-A) in order to capture optical properties and energy level alignments. Since we already know that the choice of the exchange-correlation functional is extremely important, we tried a different approach from standardized convention, using the new flexible family of local hybrid functionals with global and range-separated hybrids as a comparison. Range-separated hybrid functionals provide an overall good description of excited states when it comes to the dyes alone, but fail in dye-semiconductor systems yielding wrong and nonphysical description of energy level alignments which is proved in several cases during this study. We also used laser-induced electron injection with the hybrid LR-TDDFT and configuration interaction methodology (CI) to obtain information on photon-to-current conversion mechanism. For this we used already obtained energies and coefficients from LR-TDDFT for each functional. Electron dynamics revealed more than 60% of efficiency in most of the examined cases and strong hybridization of the lowest-unoccupied molecular orbital (LUMO) with TiO_2, while delocalization of the density is spotted through the whole cluster.

The second part of the thesis covers research on hydroxyapatites (OHAp), a calcium phosphate mineral which is the main component of human hard tissues, like bone and enamel. It is an abiotic compound and the closest we can find among minerals that resembles the structure of biological apatites, which then form hard tissues. The problem occurs when these minerals change their structure with different substitutions, leading to changes in the chemical properties and mineralization, and at the end evolving some diseases, such as osteoporosis. Our main focus was on the pristine hydroxyapatite and three different substitutions for the carbonated apatites, A-type, B-type and AB-type. The first substitution includes incorporating the carbonate ion for the two OH groups, second is when we insert carbonate instead of the phosphate and the last one

is just the combination of these two. In order to understand changes within the structure, we used two main methods used in the vibrational spectroscopy: Infrared (IR) and Raman. Using these methods we can understand the chemical properties and percentage of carbonate inside the specific types, as well as the importance of the orientation of the sample with respect to the laser (light) source. Also, we probed the information about the surface phonons in nanosized hydroxyapatite, detecting them in the visible spectra and distinguishing from their bulk counterpart. Raman spectra is especially important since it is more sensitive to the carbonate ions. When it comes to the orientation dependencies, our results are very well matched with the experimental investigations showing a great orientational dependency by looking at the specific bands, especially in the zz-direction which shows the highest sensitivity. Surface phonons are located as a shift on higher and lower wavenumbers in comparison to the bulk and it all depends on the surface termination and orientation. Since we compared different slab thicknesses, one must be careful because the phonons can be observed and have impact even on the nanometer scale. All shifts regarding the surface presence are measured with both, IR and Raman spectroscopy.

Contents

1 Introduction

In order to discover the secrets that nature holds, we must understand the complex, yet powerful concept of quantum mechanics. This is the only language that nature speaks and a real model of reality. If we overcome this obstacle and master the language of nature, an exciting journey awaits us in understanding the world in which we live in. Quantum mechanics is often counter-intuitive and the governing laws are quite difficult to imagine. Since it mostly deals with atoms, it is very easy to find an example to confirm the previous statement. If we look around, we won't really find anything that could be closely compared with atoms. Their dimension is so small it is practically unimaginable. First thing that could come to people's mind is a spider web, but it is also incomparable considering that it's 100 000 times larger than the largest diameter of an atom.

Good news is that since the birth of quantum mechanics (between two world wars) until today, science has made great strides and brought us many useful methods through which we can investigate the phenomena that surround us. One of them is the popular density functional theory, firstly introduced by two Hohenberg-Kohn theorems (1964) and later refined for practical use with the Kohn-Sham equations, which will be presented in detail in the next Chapter (1965)[1, 2].

This dissertation is divided into two parts. The first part is dealing with the discoveries in the field of the new, third-generation of solar cells, called Dye-sensitized solar cells (DSSCs), invented and designed by Michael Grätzel and Brian O'Regan in 1991[3]. In comparison to the first-generation solar cells based on silicon, DSSCs are showing a great alternative potential, because they are environmentally friendly, based on organic materials, cheap for production and work very efficiently under diffused light[4, 5, 6, 7, 8]. In our work we focus on metal-free organic DSSCs with different structures. We are particularly intersted on the dye structure alone, composed of one and two donor groups, while we stick with the titanium dioxide (TiO_2), which is the most used and the most efficient semiconductor[9]. Dyes are connected to the semiconductor via acceptor group which will carry the charge and injection to the interface. Density functional theory can help us to better understand the optical and electronic properties of free and combined dyes. We focus on the performance of the local hybrid density functionals and electron dynamics. The main goal is to understand the transition energies of the lowest excited states, absorption spectra, energy level alignments at the dye-semiconductor interface, charge injection efficiency and population dynamics of the selected states. All of this with respect to the local hybrid functionals which are still not investigated on this subject. The mentioned properties can be effectively compared to the experimental values which can help us determine the most accurate approach. Results in our both papers showed a great accuracy using local hybrid functionals and wrong description of energy level alignments with the popular range-separated functionals like CAM-B3LYP, coming from the band gap overestimation. Looking at the electron dynamics, there is a significant charge injection of more than 60% and strong hybridization. More on the structure, working principle, efficiency

and advantages of DSSCs will be further introduced and discussed in detail later in the Chapter 3.

The second part is the work on the orientation effects and surface phonons of biological apatite, which is the main component of hard tissues like bones, dentine and enamel[10, 11, 12]. Specifically, calcium apatite mineral, hydroxyapatite (OHAp), is examined. This mineral can exhibit different substitutions in its own structure which significantly change their properties. That is why we investigate the type-A substitution in which carbonate ions replace hydroxyl group, type-B substitution where carbonate takes place of the phosphate and type-AB which is the combination of both. In order to detect changes and chemical properties, we use vibrational spectroscopy methods: Infrared (IR) and Raman spectroscopy. Looking at the different vibrational bands and their intensity in respect to the orientation of the sample can help us to discover the chemical environment and ions percentage in the specific types of the structures. Also, identifying the surface phonons in spectra and the specific sites which they occupy can't be observed with the experiments, thus we use DFT to find an answer on the visibility of the phonons inside a finite sized, nano OHAp. Obtaining accurate infrared and Raman spectra is of critical importance for comparison with real samples and for the generation and testing of substituted structures. Thus, with the DFT framework we aim to model pristine OHAp (without substitutions) and later type-A, type-B and type-AB. The critical input parameters are found in the literature and they show experimental vibrational spectra in similar systems. This allows us to validate our models as well as test the two main questions we want to answer: What is the extent of orientation dependence on the relative intensities of the carbonate and phosphate bands in vibrational spectroscopy data? Do measured differences originate entirely from the applied incoming light source direction or does preferred growth morphology and nanometre size of the crystals, i.e. dominance of surface over bulk phonon signatures, also result in spectral changes?

Results showed great sample orientation dependency with respect to the incoming laser source. There will be almost no band intensity when the laser is perpendicularly oriented to the crystal, while the z-axis orientation has the largest sensitivity for the phosphate and carbonate groups. Surface phonons are found on both, higher and lower wavenumbers in comparison to the bulk and it will depend on the surface termination. Most importantly, we proved that surface properties can be detected with both IR and Raman spectroscopy methods up to a nanometre thickness of our generated slab. Chapter 4. will provide more theoretical details about morphology, structure, function and possible substitutions of this mineral.

2   Density Functional Theory (DFT)

Studying any quantum mechanical system requires solving the complex Schrödinger equation, which is nearly impossible, except for the hydrogen atom[13]. Density functional theory (DFT) provides an approximate solution to the many-body Schrödinger equation by reformulating the problem in terms of the electron density, rather than directly solving the complex Schrödinger equation. This provided a smart escape routine, but at the same time having fairly accurate solutions when studying certain properties of individual systems. The idea behind DFT is simple and effective. Sometimes, one could wonder how it is actually working, since the essence of the whole theory lies in the fact that all the properties of the observed system can be determined if we know the electron density.

As it is already mentioned in the previous Chapter, DFT was born in 1964 by Pierre Hohenberg and Walter Kohn who gave the science community two basic theorems[1]. The first theorem states that the energy is a functional of the electron density

$$E = F[\rho]. \tag{1}$$

This means that the ground-state energy depends only on the density and it can directly regulate the Hamiltonian which consists of all possible interactions between the particles in the system. The second theorem makes sure that if we minimize the proposed functional over all possible densities, we would be able to find exact ground-state density and particular energy. As our focus lies exclusively on the behavior of electrons within the observed system, we employ the Born-Oppenheimer approximation. This approximation is particularly valuable when dealing with systems involving electrons and nuclei, as it allows us to treat the electronic and nuclear motions separately. In the Born-Oppenheimer approximation, the motion of the electrons is considered much faster than that of the nuclei, enabling us to treat the electronic configuration as if the nuclei were stationary. Specifically, in the context of the Coulomb potential, we treat the nuclei as fixed and their Coulomb potential as an external field experienced by the electrons. This approximation is justified by the significant difference in mass between electrons and nuclei. Consequently, the Born-Oppenheimer approximation simplifies the complex quantum mechanical problem by decoupling the electronic and nuclear motions, facilitating a more tractable analysis of the electronic behavior within the system[14]. This is important to mention, because we can say that, when summed up, the electron density determines the external potential, which, in turn, determines the many-electron wavefunction, and, ultimately, the total energy is a functional of the many-body wavefunction.

A year after (1965), Walter Kohn and Lu Jeu Sham gave the practical framework so the electronic structure problem can be solved through a set of one-electron equations[2]. The fundamental idea behind the Kohn-Sham equations in (DFT) is to address the interaction of numerous electrons within a system by introducing a set of auxiliary, non-interacting electrons. Despite being conceptual and not physically real, these auxiliary electrons serve as a practical

computational tool. It's important to emphasize that, while these electrons are introduced for computational convenience, the electron density derived from their wavefunctions faithfully mirrors the true electron density of the interacting system. The Kohn-Sham approach allows us to reformulate the complex many-body problem into a set of equations involving non-interacting electrons, simplifying the computational treatment of electron-electron interactions. In principle, we have pseudo-eigenvalue equations for a single-particle system, resembling the Schrödinger equation in which electrons don't interact. Instead, they are a subject to an effective potential determined by our key ingredient, electron density. The energy functional in the Kohn-Sham frame has several terms

$$
\begin{aligned}
E = \int \rho(\mathbf{r}) V_\rho(\mathbf{r}) d\mathbf{r} - \sum_i \int \phi_i^*(\mathbf{r}) \frac{\nabla^2}{2} \phi_i(\mathbf{r}) d\mathbf{r} \\
+ \frac{1}{2} \int \int \frac{\rho(\mathbf{r})\rho(\mathbf{r}\,')}{|\mathbf{r} - \mathbf{r}\,'|} d\mathbf{r} d\mathbf{r}\,' + E_{XC}[\rho].
\end{aligned}
\tag{2}
$$

From left to right, the first term represents the external potential, the second the kinetic energy through the Kohn-Sham orbitals, ϕ_i, the third the Hartree energy and the last term is the exchange correlation energy. All of these terms, except the kinetic energy, depend explicitly on the electron density. That's why this kind of formulation gives us a better overview. They are all known terms, except the last one. The challenge lies in the absence of an exact form for this functional. However, the promising aspect is the acknowledgment of its existence, granting us the latitude to seek the most suitable approximation method. The quest for finding an approximation which will give us the universal solution for every system and property is still open.

Usually, one starts with the same approach by dissecting the exchange correlation energy functional in two parts

$$
E_{XC}[\rho] = E_X[\rho] + E_C[\rho].
\tag{3}
$$

The exchange energy term, $E_X[\rho]$, arises due to the fermionic nature of electrons (Pauli exclusion principle), i.e. antisymmetry requirement of wavefunctions. The second term, The correlation energy, denoted as $E_C[\rho]$, accounts for the electron-electron interactions beyond the exchange term. Specifically, it quantifies the reduction in Coulombic repulsion due to the correlated motion of electrons. In other words, it represents the deviation of the true electron-electron interaction from the mean-field approximation provided by the exchange term, capturing the effects of electron correlation on the overall energy of the system. Usually, the correlation part is a magnitude smaller, while exchange energy is dominating, especially when we deal with smaller systems where interactions between the electrons are not so complex[15]. For closed- and open-shell systems the exchange energy can be calculated exactly with the help of the Slater determinant, as the difference between exact energy and Hartree-Fock, neglecting correlation effects[16, 17]. In this specific case, only the correlation energy

needs to be approximated. In practice, using DFT, we are approximating both parts.

Constructing an exchange correlation functional is everything but an easy task. In the last 40 years, hundreds of different functionals were constructed and developed by various groups of theoretical physicists and chemists. Since there is no unique and universal approximation that could give us the solution for every property of the system, people usually choose the approximation which is already proven to give satisfactory results for some specific attribute.

The story begins with the simplest model developed by Llewellyn Thomas and Enrico Fermi in 1930s, called Thomas-Fermi model of the uniform electron gas, which was introduced before formal introduction of DFT, but provides a great starting point for approximations and models which came later[18, 19]. This model provides an exact approximation for an infinite uniform electron gas, where the density is constant and homogeneous. One could be harsh, and say that this model has a lot of flaws and it can't be so useful, but if we go back, it is easy to notice how Thomas-Fermi laid a great central idea for the later DFT creation. Emphasising the important role of the electron density as a crucial and main quantity which determines all other properties of a many-electron system. The biggest drawback of the model was the impossibility of describing the chemical bonds between the atoms, which was improved by future DFT approximations.

Moving on, constructing exchange-correlation functionals can be done non-empirically and semi-empirically[20, 21]. The non-empirical route means that for the construction one must use theoretical principles without any experimental data. The main idea is to satisfy exact constraints with a parametrized mathematical form. Semi-empirical methods use experimental data together with theoretical assumptions. This approach is more flexible, based on physical ingredients and coefficients which can be fitted to some reference values. It is worth to mention how density functionals can be constructed using both methods combined which will be described more in detail later in this chapter[22].

During the development of a new functional, natural logic would be to include as many parameters we can in our approximations in order to make it more accurate. But this is not the case. Systematic increase of the new ingredients aren't promising in improving the description of interactions between the particles inside a system[15].

In order to make our lives easier, one of the most influential physicists and chemists in the DFT community, John Perdew, constructed an already popular concept of hierarchy of computational methods and efficiency through Jacob's ladder (Fig. 1). Each step on the ladder will include more ingredients inside a functional formalism. Before we step on the first rung and start with our journey, everything is in the Hartree world where we don't have any exchange or correlation included[23, 24]. The Schrödinger equation is solved as a combination of single electron equations which yields the electron density, thus the probability to find an electron at some point in space. Improving the accuracy of the electronic structure calculations begins with the first rung of exchange and correlation functionals, called Local Spin-Density Approximation (LSDA)[25].

5

This approximation includes the local electron density and the spin polarization. Here, the exchange and correlation energy depends only on the local electron density and doesn't take into account variations which evolve around the local region. LSDA works well for the uniform electron gas, but fails badly for producing molecular properties, such as band-gap underestimation, chemical reactivity and binding.

$$E_{XC}^{LSDA}[\rho] = \int e_{XC}^{UEG}[\rho](\mathbf{r})d\mathbf{r}. \tag{4}$$

Equation 4 clearly shows that the exchange-correlation energy density, $e_{XC}[\rho](r)$, depends only on the electron density, ρ.
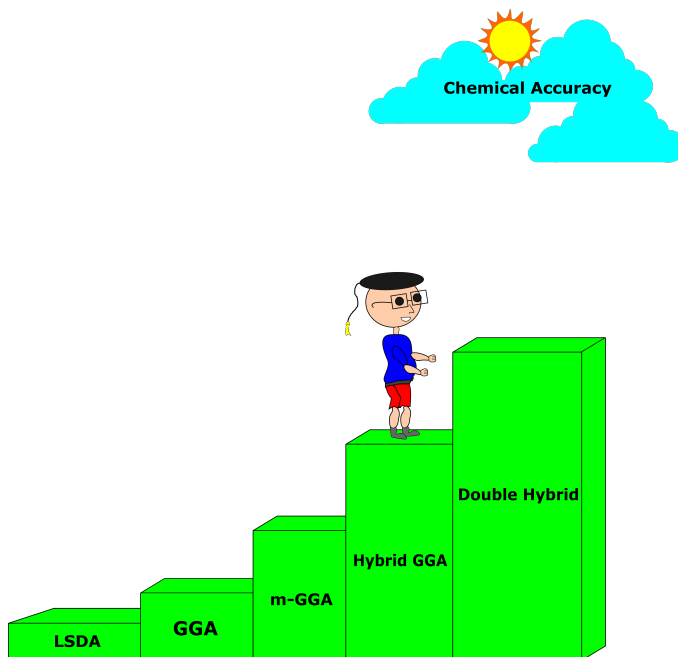
Figure 1: Perdew's Jacob's ladder constructed with five rungs. Starting from no exchange and correlation to the rest of the rungs. Local Spin-Density Approximation (LSDA), Generalized Gradient Approximation (GGA), meta-GGA (m-GGA), Hybrid GGA and Double Hybrid. As we climb through the rungs, we add new physical constraints (parameters) and the computational cost increases.

The systems are rarely homogeneous and an improvement is necessary in order to catch the electron correlation effects when the density is fluctuating. That's why the next rung is introducing a density gradient, $\nabla\rho$, as a new physical ingredient. This second rung is called Generalized Gradient Approximation (GGA) and it is allowing the spatial variations of the electron density[26].

$$E_{XC}^{GGA}[\rho] = \int e_{XC}[\rho, \nabla\rho](\mathbf{r})d\mathbf{r}. \qquad (5)$$

GGA improved upon bong lengths and reaction barriers, but it is still lacking for some properties such as weak dispersion forces and has it's difficulty to cope with strongly correlated systems.

At this point, DFT showed some great promises for the future of the quantum chemical calculations and its popularity significantly increased. The next step was to include either the kinetic energy density, τ, or Laplacian of the electron density, $\nabla^2\rho$, or both. This inclusion lead to the third rung named meta-GGA and improved calculations for a wide range of different systems and properties, such as better description of non-local effects, chemical bonding, band-gap predictions and reduced self-interaction error[27].

$$E_{XC}^{mGGA}[\rho] = \int e_{XC}[\rho, \nabla\rho, \tau, \nabla^2\rho](\mathbf{r})d\mathbf{r}. \qquad (6)$$

Functionals from this rung require more computational power, but their biggest advantage is the removal of the one-electron self-interaction error. Between these two new parameters, the kinetic energy is used more because it requires only first derivatives, while the Laplacian is numerically less stable and needs second derivatives of the basis functions.

The scientific community understood that going to the higher derivatives of the density is not that beneficial. The main problems were self-interaction error (SIE), dispersion interaction and strong correlation[15]. Self-interaction error is something that occurs because the exchange correlation functional is not exact and it is leading to wrong results and unphysical bahaviour[28]. This happens when an electron is interacting with its own charge distribution which has serious impact to the electron wavefunction. Second, dispersion interaction happens when we want to capture and understand the correlation effects at long distances. It is coming from the Coulomb repulsion between electrons. Functionals up to this point can't really cope with dispersion forces and van der Waals interactions, since they are built up on local or semi-local parameters[29]. Lastly, strong correlation problem needs to be treated accordingly. For example, when we have a system constructed of transition metals, electrons may localize and thus increase the Coulomb repulsion and correlation[30]. The aforementioned problems are still ongoing research and the day-by-day larger DFT community is working on new methods in order to find solutions.

After the realization of these problems, a little stagnation followed as far as the develompment of the DFT is concerned. That was interrupted by a remarkable idea from Axel Becke to combine exact exchange (Hartree-Fock) together with density functionals[21]. This type of mixing opened the door for a new family of functionals on the fourth rung called hybrid functionals.

$$E_{XC}^{GH} = cE_X^{HF} + (1-c)E_X^{DFT} + E_C^{DFT}. \qquad (7)$$

The universal mixing fraction, c, will determine how much exact exchange there is in some hybrid functional. It goes from 0% to 100%, but the most popular functionals have between 20% and 25%. The idea was to partially treat exchange interaction between the electrons as exact and to take care of the non-local behaviour. Also, the important problem of SIE is partially corrected with the appropriate amount of exact exchange, typically from 10% to 30% which leads to more accurate results for band gaps, excited states, and charge transfer properties.

Since one part of this thesis is dealing with local hybrid functionals, it should be stated that they belong to the fourth rung[31, 32]. They represent a separate family of functionals with more flexible exact exchange admixture. In local hybrids, the mixing fraction becomes real-space dependent and it depends on the local chemical environment. The mathematical formulation of the local hybrid functionals includes a mixing of exchange energy densities, e_X, instead of semi-local and exact exchange integrated energies like in global hybrids.

$$E_{XC}^{LH} = \int [a(\mathbf{r})e_X^{HF}(\mathbf{r}) + (1 - a(\mathbf{r}))e_X(\mathbf{r}) + e_C(\mathbf{r})]d\mathbf{r}. \tag{8}$$

An important ingredient is the local mixing function (LMF), $a(r)$, which is responsible for the exact exchange admixture. LMFs are built upon some theoretical constraints and often contain at least one empirical parameter. The most popular versions are the ones based on the kinetic energy (t-LMF) and s-LMF, based on the dimensionless density gradient s[33],

$$a_\delta^{t-LMF}(\mathbf{r}) = b\frac{\tau_\delta^W(\mathbf{r})}{\tau_\delta(\mathbf{r})}. \tag{9}$$

$$s_\delta^{s-LMF}(\mathbf{r}) = \frac{1}{k}\frac{\gamma_{\delta\delta}^{\frac{1}{2}}(\mathbf{r})}{\rho_\delta^{\frac{4}{3}}(\mathbf{r})}. \tag{10}$$

Equations 9 and 10 are representing the t- and s-LMF, respectively. The first is based on the ratio of the von-Weizsäcker, $\tau_\delta^W(r)$, and conventional kinetic energy density, $\tau_\delta(r)$, while b stands for the optimal scaling factor. The second one is constructed from the dimensionless reduced spin-density gradient, where k is the prefactor and the $\gamma_{\delta\delta}$ square of the spin-density gradient. Later, s_δ is reformulated and has to be mapped onto the [0,1] interval with the error function $g_\delta = erf(bs_\delta)$.

3 Linear Response TDDFT (LR-TDDFT)

When it comes to the excited states, describing the properties is getting more problematic and we need to find an adequate balance between the computational cost and accuracy for our systems. While the ground state exists in isolation, separate from other states, excited states often exhibit similarities at higher energies, involving more than one electronic state. As the calculation evolves

over time, the chemical picture, encompassing all possible properties, may vary. Still, the usual and pretty accurate method for calculating excited states is linear-response time-dependent DFT (LR-TDDFT)[34, 35]. Of course, like every other method, it has a lot of flaws and it is not perfect, especially for charge-transfer states, strongly-correlated systems and it has difficulty dealing with excitations in open-shell species[36, 37, 38]. In general, TDDFT arises from the two principle theorems given by E. Runge and E. K. U. Gross in 1984, as an extension of the already known two Hohenberg-Kohn theorems with the time-dependent framework for the external potentials[35]. They explained how the entire system evolves in time when you apply some small perturbation or a fully time-dependent potential, starting from the ground-state density.

The entire TDDFT is reflected through the Kohn-Sham framework, as a construction of the non-interacting system which can be related to the interacting one, but both are time-dependent.

$$i\hbar\frac{\partial\phi_i(r,t)}{\partial t} = \widehat{H}^{KS}[\rho](t)\phi_i(r,t). \tag{11}$$

In the equation, $\phi_i(r,t)$ are the time-dependent Kohn-Sham spin orbitals and $\widehat{H}^{KS}$ is the Hamiltonian expressed as a function of the time-dependent density. The Hamiltonian is following the time-dependent external potential, hartree potential and exchange-correlation potential. Among these potentials, only exchange-correlation is depending non-locally to the all densities which evolved through the time, while other are local.

Equation 11 can be solved in two ways, using the real-time integration or with the linear-response theory, which is the main focus of our research[39, 40]. Using the real-time integration solution we can directly simulate how our quantum system evolve after the applied perturbation, while in the linear-response theory we are focused on the system reaction on a weak electric field, without following the whole motion. That's why the linear-response is much more useful when we try to understand, for example, how some molecules absorb light. The linear response of the density to a small time-dependent perturbation in the non-interacting system is represented as

$$\delta\rho(r,t) = \int_{-\infty}^{t} dt' \int dr' \zeta(r,r',t-t')\delta v_{ext}(r',t'). \tag{12}$$

where ζ is the response function and v_{ext} the external potential. Applying the Fourier transformation we can write the response function depending on the Kohn-Sham orbitals, ϕ, and eigenvalues, ϵ

$$\zeta(\omega) = \lim_{\eta\to 0^+} \sum_{pq}(f_q - f_p)\frac{\phi_p\phi_p^*\phi_q\phi_q^*}{\omega - (\epsilon_q - \epsilon_p) + i\eta}. \tag{13}$$

where f_p and f_q are occupation numbers. The next step is to substitute the external potential from eq. 12 and get to the form of the Dyson equation in which we can define the exchange-correlation kernel, f_k,

$$(1 - \zeta(\omega)f_k(\omega))X(\omega) = \omega X(\omega). \tag{14}$$

X is representing the eigenvector, and the kernel can be expressed as

$$f_k(\omega) = \frac{\delta v_H(\omega)}{\delta \rho(\omega)} + \frac{\delta v_{xc}(\omega)}{\delta \rho(\omega)}. \tag{15}$$

This popular equation for the LR-TDDFT is usually represented through the Casida formulation with the expansion on the Kohn-Sham orbitals.

$$\begin{bmatrix} A & B \\ B^* & -A \end{bmatrix} \begin{bmatrix} X \\ Y \end{bmatrix} = \omega \begin{bmatrix} X \\ Y \end{bmatrix}. \tag{16}$$

A and B are matrices containing the response function, difference in eigenvalues and exchange-correlation kernel[34, 37].

$$A_{ia,jb}(\omega) = \delta_{ij}\delta_{ab}(\epsilon_a - \epsilon i) + (ia|\widehat{f}_k(\omega)|bj). \tag{17}$$

$$B_{ia,jb}(\omega) = (ia|\widehat{f}_k(\omega)|jb). \tag{18}$$

Since our work is concentrates mostly on local hybrid functionals, local hybrid exchange kernel integrals will be used for the LR-TDDFT calculations. For these extensions, one can check the equations 22 and 23 from the Ref. [41].

This approach allows us to reveal how an excited electron is promoted from one orbital to the other, and to calculate some properties like dipole moments and oscillator strengths. It gives us a tool to analyze and describe the nature of electronic excitations in molecules and materials. The interested reader can take a look at the Ref. [42] for more detailed explanation of the TDDFT methods in general.

4 Dye-Sensitized Solar Cells (DSSCs)

In today's world there is no need to emphasise further how things need to change when we talk about energy consumption. Natural gas and fossil fuels take around 80% on a daily basis, the amount of cabon dioxide emission rises every day which at the end causes global warming, greenhouse effects, polar vortex and so many issues, threatening to destroy the quality of our lives if we don't react properly[43, 44, 45, 46]. We need to find an alternative way using sustainable energy sources that have good efficiency, that are cheap and thus available to all households, and finally something that can be renewed. Using energy from the sun and converting it into electrical energy is the way to go. This can be done by solar cells and photovoltaic technology. The first example of a solar cell was designed in 1954. by a team of scientists at the Bell Laboratories with a silicon p-n junction. This was a breakthrough which opened the door for the developments and finding a way to somehow increase the efficiency, since they reported it around 6%[47]. Scientists continued working on silicon

solar cells and by the newest reports achieved a laboratory highest efficiency of 26.6%[48]. Overall, this has been a great advancement in the photovoltaic technology, but there are three major problems with silicon solar cells concerning environmental impact, high costs and manufacturing complexity. Firstly, production of cells results in emission of greenhouse gases while mining and refining silicon. Second, the cost is high, they are more expensive than fossil fuels and people will always choose a cheaper option. Lastly, they include very complex manufacturing process with crystal growth, doping and high-temperature treatments with expensive and very precise tools.

This is the reason why over the last decades scientists are intensively investigating the third generation of solar cells, called dye-sensitized solar cells (DSSCs), which are a promising alternative from the efficiency and low-cost point of view. They were introduced by Michael Grätzel and Brian O'Regan, as was already mentioned earlier[3]. The first reported energy conversion efficiency was 7.1% and this increased to 13% in 2014[49]. The operation mechanism of DSSCs is very clever and simple. It is constructed from five different parts: transparent conductive oxide (TCO) glass substrate, semiconductor layer (TiO_2), sensitizer (dye), electrolyte and a counter electrode deployed on another TCO glass substrate (Platinum) (Fig. 2).

One side represents a photoanode consisting of a mesoporous oxide (TiO_2) and the dye sensitizer which is covalently bonded to the mesoporous layer. All of this is deployed onto a TCO glass substrate. The other side is representing a counter electrode, usually made of platinum which has a great electrical conductivity and catalytic activity (other alternatives can be silver or carbon). At the end, the entire structure is sealed with an electrolyte with some redox couple (usually iodide/triiodide). The working principle of DSSCs is divided in four different steps (see Fig. 2). At the beginning, solar energy from the sun falls onto a photoanode which will absorb the incident energy. With all of this energy, electrons are excited from the ground to an excited state. In the context of the one-electron or mean-field approximation, this means that the electrons jump from their highest occupied molecular orbital (HOMO) to the lowest unoccupied molecular orbital (LUMO), and this is the first step. It is important to note that in reality we have a more complex picture, where electronic excitations are more like a collective behaviour of all electrons in the present system, where electron can distribute its charge density over multiple orbitals. The second step involves an oxidation of the dye, thus electrons jump to the conduction band (CB) of the semiconductor (TiO_2). At the third step we go back and "fill the gaps". The process requires the lost electrons to be replaced accordingly and the electrolyte will donate the electrons to the dye and regenerate it to its initial state. At the end, the catalytic counter electrode is returning an electron to the electrolyte through reduction process and external circuit.

The most important part of DSSCs is the dye sensitizer. They are responsible for the efficiency enhancement through absorption of light in the visible and infrared spectrum and strong covalent binding with the semiconductor layer. In principle, the LUMO of the dye needs to be at the higher energy then CB of
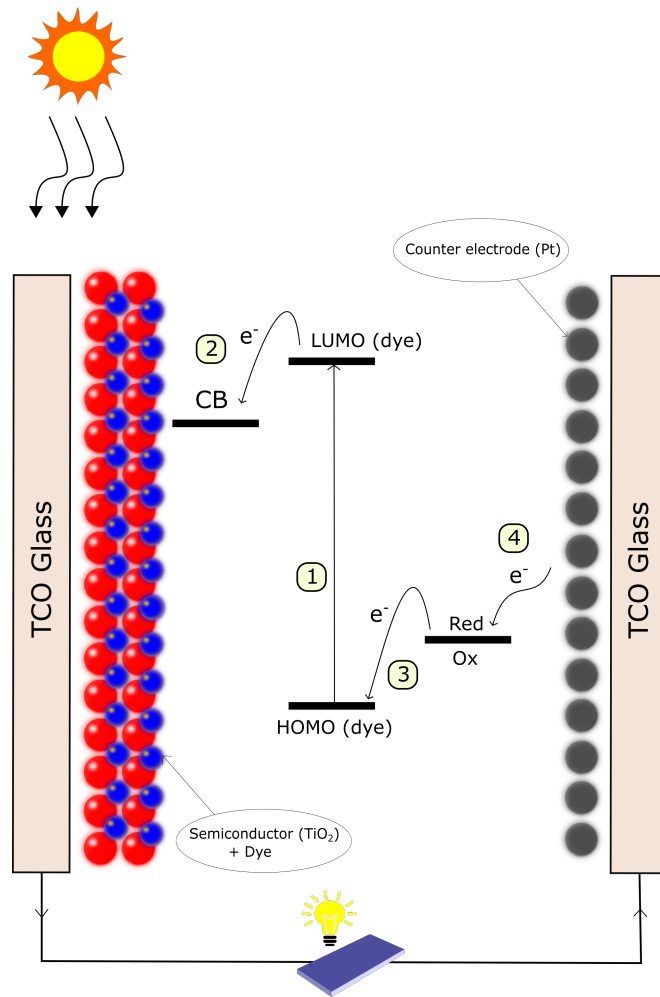
Figure 2: Shematic structure and working principle of DSSCs.

the semiconductor and the HOMO must have a smaller energy then the redox couple. This is the basic requirement for the device to have a proper charge injection and regeneration and to work efficiently. Until now, ruthenium (Ru) - polypyridyl-complexes achieve the highest efficiency of 11%, but they are not the best choice because of their toxicity and easy degeneration in combination with some electrolyte, like water[50, 51, 52]. The focus is rather on organic and metal-free type of dyes which can work efficiently under diffuse light and be completely eco-friendly.

Organic dyes have donor-π-conjugated spacer-acceptor (D-π-A) structures. This constellation allows us to alternate and change different parts of the dye in order to make improvements. Donor groups should be electron rich and the π-linker is in most cases build from thiophene units because of their great charge transfer features, plus so far, the acrylic acid group is found as the most promising acceptor unit[53]. DSSCs based on organic dyes are still not as efficient as the ruthenium one but there is more room for improvement since they have more flexible structure, which can be altered.

When it comes to the semiconductor, a large surface area is needed to adsorb the dye and accept the excited electrons during the process. In most of cases, several metal oxides are used (TiO_2, ZnO and SnO_2)[54, 55]. After some time, experiments showed that the best option is TiO_2, while the other two in comparison produced lower efficiency[55, 56, 57]. The most studied structure of TiO_2 is anatase, providing satisfactory results, including a wide band-gap of $3eV$ which makes the structure more chemically stable[58, 59]. It has more surface area to adsorb the dye molecule, reduced chances for the recombination process with faster electron transport and high stability, avoiding corrosion and material deterioration.

The most used electrolytes are liquid, but in the recent times solid-state and quasi-solid gained attention as the alternative choices and they are still an ongoing research. The electrolyte should receive electrons from the counter electrode and it is responsible for the whole process of the regeneration. They need to be thermally and electrochemically stable and should not overlap with the dye absorption spectrum. Experiments showed that the iodide/triodide redox couple has the slowest recombination rate, although the main problem of the liquid electrolyte remains a significant leakage after some time of usage[60, 61].

The counter electrode regenerates the electrolyte and platinum is the most used one. It is very conductive, a good catalyst, chemically inert and has low charge transfer resistance[62]. The only problem is that platinum has high costs and this forced research with some other materials, like graphite and graphene, but both of them exhibit lower effciency in comparison to platinum[63, 64].

Improving the DSSCs efficiency is still one of the most important challenges in the photovoltaic community. The manufacturing costs are very low and this knowledge alone could change the way how people use energy sources. It could provide a path to a cleaner world if the efficiency increase, at least to the level of silicon solar cells. Every mentioned component needs advancement in order to massively commercialize these type of solar cells on the market and offer to

people for long-term use.

5 Electronic structure, optical properties, and electron dynamics in organic dye-sensitized TiO$_2$ interfaces by local hybrid density functionals

CRediT authorship contribution statement

Dejan Gemeri: Conceptualization, Calculations, Data curation, Writing - original draft.

5.1 Abstract

In this work, we present theoretical investigations of dye-sensitized solar cells (DSSCs) using linear response time-dependent density functional theory (LR-TDDFT) and electron dynamics within the hybrid TDDFT/ configuration interaction methodology. To evaluate the potential of local hybrid density functionals for such hybrid systems, we study the electronic properties of two organic dyes, both isolated and anchored on a typical semiconductor substrate (TiO$_2$). The implemented strategies can accurately predict electronic structures, optical properties, and energetic alignments of the investigated dye@TiO$_2$ systems. The accuracy of charge transfer excited states and the hybridization between the interfacial states depend appreciably on the used exchange correlation functional. This work emphasizes the performance of local hybrid functionals in comparison to the most commonly used global hybrid and range-separated hybrid functionals. Investigation of laser-induced charge migration dynamics sheds light on the effect of hybridization between the dye and the substrate at the interface on both the population transfer dynamics and the charge injection rate.

5.2 Introduction

As our daily global consumption of energy is ten thousand times smaller then what earth receives from the sun[65], harvesting solar en- ergy through photovoltaic (PVs) devices is the natural, promising choice for a sustainable development. Within PV technologies, dye-sensitized solar cells (DSSCs) represent

an appealing and cheaper alternative to traditional silicon-based solar cells, offering the advantage of being flexible, transparent and working with diffused light[3, 7, 8].

The peculiar feature of DSSCs is that light harvesting, electron transport, and hole transport are operated by different components in the cell. As a matter of fact, the overall cell performance is governed by a number of interplaying factors[66], such as the optical and electronic properties of dye sensitizers and semiconductors, the structure of the hybrid molecule/metal oxide interface, the efficiency of the electron transfer from the redox mediator to the oxidized dye, and of the electron injection into the conduction band (CB) of the semiconductor substrate. Focusing on the charge injection, the two key quantities dictating the kinetic of the process are the electronic coupling between the donor (dye) and the acceptor (semiconductor), that is the extent of hybridization between the interfacial states, and the driving force, which is related to the alignment of dye/semiconductor energy levels. In particular the excited state oxidation potential of the dye should be higher (more negative) than the CB edge of the semiconductor[67, 68, 69]. Concerning the regeneration process, the energetic requirement is that the ground state oxidation potential of the dye is lower (more positive) than that of the redox couple[70]. In order to realize an efficient and unidirectional charge transfer, organic sensitizers are usually built following a push–pull (D-π-A) architecture, with the donor group (D) being an electron-rich unit, connected via a conjugated bridge (π) to the electron acceptor group (A), which is covalently bound to the semi- conductor surface, usually through a carboxylic or cyanoacrylic function.

In the last decades, theoretical and computational studies have provided fundamental information and atomistic understanding of DSSCs materials and processes, useful to assist experiments toward boosting the device efficiencies[71, 72, 73, 74, 75, 76, 77, 78]. Due to the complexity of the systems, density functional theory (DFT) and its linear response time-dependent density functional theory (LR-TDDFT) represent the methods of choice to describe most of the important properties of the individual dye/semiconductor systems and of their hybrid interfaces. However, while standard LR-TDDFT approaches can accurately describe the optical properties and the system energy level alignment of Ru(II)- complexes grafted on the TiO$_2$ surfaces, the characterization of the excited state properties of push–pull organic dyes and of the corresponding dye-sensitized TiO$_2$ interfaces is problematic[79, 80, 81]. This is the result of the erratic description by conventional exchange–correlation (XC) functionals of the charge transfer excitations, which characterize the visible absorption of typical (D-π-A) organic dyes and consequently of the related dye-sensitized interfaces.

Some of us have shown that available LR-TDDFT methods are not capable to deliver at the same time a balanced description of the dye-TiO$_2$ excited states and of the alignment of the dye excited states with the semiconductor manifold of unoccupied states[82]. Indeed, standard B3LYP provides the correct alignment of the dye/semiconductor Kohn–Sham energy levels along with a wrong dye's excitation energy, stronger hybrids or long-range corrected hybrids deliver the accurate prediction of the dye's excitation energy with an nonphys-

ical description of the relative Khon-Sham eigenvalues. These results are the consequence of a different and unbalanced description of the dye and semiconductor excited (or unoccupied) states. Reliable energetics for bulk materials as well as for charge transfer excited states in organic dyes have been obtained resorting to many-body Green's functions theory within the GW approximation and the Bethe–Salpeter equation (BSE). As the computational cost of GW and GW-BSE calculations is significantly higher than that of DFT and LR-TDDFT simulations, their application to problems of such a large size and complexity has been rather limited and only recent advances in algorithms have allowed a wider utilization[83, 84, 85, 86, 87, 88, 89, 90, 91, 92].

A recent and promising new family of DFT functionals, whose flexibility seems to be favourable for the description of hybrid organic–inorganic DSSC interfaces, are local hybrid density functionals[32, 33, 93, 94, 95, 96]. As we shall detail in subsection 4.3, in the construction of a local hybrid functional, different amounts of exact exchange are used at each point in space, thus allowing much more flexibility with respect to global hybrid and long-range corrected functionals. To the best of our knowledge, the performance of local hybrid approaches in predicting the interfacial energy level alignment and the optoelectronic properties of dye-sensitized-TiO_2 systems has not been assessed so far.

Here we tackle this issue and, following the work of Ref. [82], consider two prototypical organic dye sensitizers[97], and their interface with an anatase $(TiO_2)_{82}$ slab. Titanium dioxide exhibits a large band gap and high CB edge energy, which can lead to higher efficiencies[9, 7]. While a large band gap reduces the light which can be absorbed, it can increase the oxidation power of electrons by moving the valence band to the higher energy level relative to the redox potentials[98]. In order to accurately represent the CB structure we used a $(TiO_2)_{82}$ anatase cluster established in previous works. This three-layer slab represents the electronic structure equally well as a larger $(TiO_2)_{82}$ cluster[72, 99, 100].

The two dyes investigated in this work are shown in Fig. 3. They have markedly different electronic structure and charge transfer properties: the indoline D102 dye has a moderate push–pull character and is connected to the TiO_2 surface via an unconjugated rhodadine-3-acetic acid anchoring group, while the JK2 sensitizer is characterized by a strong charge separation in the lowest singlet excited state. JK2 also exhibits a sizeable coupling with the TiO_2 CB states, induced by the conjugated cyanoacrylic anchoring group. As discussed in Ref. [82] the different electronic structure and optical properties of the chosen dye-TiO_2 systems require different fraction of exact exchange to get a reliable estimation of the optical absorption spectrum, which may result in an unphysical description of the relative energy level alignment at the dye-sensitized semiconductor interface.
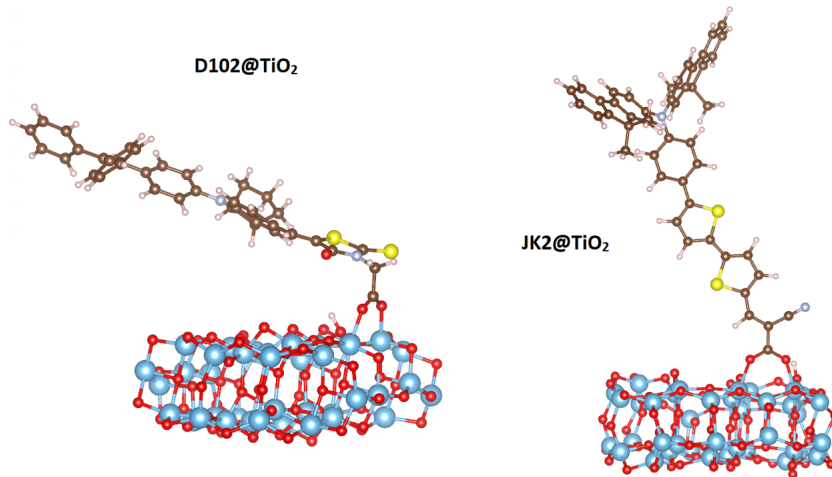
Figure 3: Representation of the D102@TiO$_2$ and JK2@TiO$_2$ structures. Titanium atoms in blue, oxygen in red, carbon in tan, hydrogen in white, sulfur in yellow.

5.3 Theory

5.3.1 Density functionals

The most general form of a global hybrid functional is given by

$$E_X^{GH} = a_0 E_X^{ex} + (1 - a_0) E_X^{sl}, \tag{19}$$

where a fixed fraction a_0 of the exact exchange energy E_X^{ex} is combined with a seminumerical approximation E_X^{sl}[101]. This fraction is a compromise between the cancellation of self-interaction error (SIE) and static (nondynamic) correlation which is associated with semi-local exchange functionals. Inherently, many molecular and solid-state properties depend on the amount of exact exchange (excitation energies, magnetic properties and band gaps)[102]. Consequently, for different kind of systems the amount of exact exchange is frequently adjusted and many different global hybrid functionals are available. This strategy becomes, however, unpractical in donor–acceptor systems or at interfaces where the optimal a_0 may vary strongly for a given subsystem.

A related problem is the description of charge-transfer excitations with linear response time-dependent DFT (LR-TDDFT). Semilocal functionals typically fail here and the use of global hybrid functional leads to limited improvement[103, 104, 105]. With the introduction of range-separated or long-range corrected functionals, accurate characterization of charge transfer states became possible within LR-TDDFT[36, 106]. In these functionals the interaction is separated into a short and a long-range part. For molecular systems exact exchange is

used at long range to yield the correct asymptotic behaviour of the XC potential and cancel self-interaction error in the asymptotic region, thereby improving the description of Rydberg states and long-range charge-transfer. The distance at which these functional switch from short- to long range is dictated by a fixed parameter and its optimal value is distinctly system-dependent.

Clearly, heterogeneous systems, such as the DSSC models studied here, require a more flexible approach regarding the fraction of exact exchange, as the one offered by the more recently introduced local hybrids functionals. The main idea is to use different amounts of exact exchange at each point in space by introducing a local mixing function (LMF) $a(r)$.

$$E_X^{LH} = \int a(r)\epsilon_X^{ex}(r)dr + \int (1 - a(r))\rho(r)\epsilon_X^{sl}(r)dr. \tag{20}$$

Here, on the right-hand side we distinguish the exact exchange energy density ϵ_X^{ex} , the semi-local exchange energy density ϵ_X^{sl} and a local mixing function $a(r)$. The local mixing function is the central element and in this work we focus on two main types, namely t- and s- LMFs[107, 108, 109]. The first is based on the ratio of the von-Weizsäcker and the conventional, orbital-dependent kinetic energy density. This quantity identifies regions dominated by one orbital to remove the self-interaction through exact exchange. The s-LMF on the other hand employs the dimensionless density gradient which is related to the detection of regions of the r-space where static correlation is important. Both contain one empirical parameter that has been fit to basic chemical properties. In case of the t-LMF it is a simple prefactor determining the maximum amount of exact exchange used in one-orbital regions. The parameter in the s-LMF is buried inside the error function that is used to project the reduced density gradient onto the interval between 0 and 1, and thus dictates the slope of the LMF between these limiting values.

The overall task of the LMF is to balance cancellation of self-interaction error through exact exchange while retaining static correlation mimicked through semi-local exchange (second term on the right- hand side in Eq. 20). Local mixing functions based on the kinetic energy (t-LMF) are currently the most effective ones. They satisfy the limit of homogeneous densities and exhibit a steep increase in the intermediate region[109, 96]. The intermediate region is the transition between valence and asymptotic region, which was found to be crucial for the accuracy of calculated excitation energies and has been an important part for the description of charge-transfer in long-chain-donor–acceptor systems[110]. As mentioned above, this fine balance between exact and approximate exchange is far more important than complete elimination of the self-interaction error[33]. The s-LMF, on the other hand, has a slower increase in the intermediate region but satisfies and corrects the asymptotic limit. This is not guaranteed with the currently used versions of the t-LMF[111, 112].

Several local hybrids have shown remarkable accuracy for excitation energies, magnetic properties and other basic molecular properties[111]. Special attention was paid to the correction and removal of self-interaction error (SIE) in the density functional. One way to deal with errors brought by the LDA correlation

functional is to separate it into a short- and long-range part and apply self-interaction correction only at short interelectronic distances. This retains the error cancelation between LDA exchange and correlation at long range where it is most effective[113]. Removing, or at least significantly reducing, the self-interaction error at short range in the correlation functional allows for higher prefactors in the definition of the t-LMF and, thus, leads to overall increased exact-exchange admixtures in the functional. By readjusting the parameter in the exchange part, two new local hybrid functionals have been obtained, one with self-interaction-free (sif) and one with self-interaction reduced LDA correlation (sir) at short range. In the latter, only as much one-electron SIE in the short-range correlation is removed as the maximum amount of exact exchange determined through the prefactor in the t-LMF. In the following, we will investigate the potential of these local hybrids to reproduce the electronic structure of excited states in challenging hybrid materials – organic dyes@TiO_2 – which were previously found to be inaccurately described by LR-TDDFT with all available functionals. The development of local hybrid functionals has also been extended to periodic systems with a plane-wave basis. A symmetrized LMF based in the reduced density gradient was employed showing promising results for level alignments at solid interfaces[114].

5.3.2 Many-electron dynamics

We simulate laser-induced electron injection in the model DSSC using the hybrid time-dependent density functional theory/configuration interaction methodology (TDDFT/CI)[115, 116, 117], in the reduced density matrix formulation (ρ-TDCI)[118, 119, 120]. The reduced density matrix evolves according to the time-dependent Liouville-von Neumann equation

$$
\begin{aligned}
\partial_t \hat{\rho}(t) = & -\frac{i}{\hbar}\left[\left(\hat{H}_{\mathrm{el}} - \hat{\mu}\cdot\mathcal{F}(t)\right), \hat{\rho}(t)\right] - \frac{1}{\hbar}\left[\hat{W}_{\mathrm{el}}, \hat{\rho}(t)\right]_+ \\
& -\frac{1}{2}\sum_{mn}\left(\left[\hat{C}_{mn}\hat{\rho}(t), \hat{C}_{mn}^\dagger\right] + \left[\hat{C}_{mn}, \hat{\rho}(t)\hat{C}_{mn}^\dagger\right]\right)
\end{aligned}
\tag{21}
$$

where $\hat{H}_{\mathrm{el}}$ is the field-free many-electron Hamiltonian and the interaction with an external electric field $\mathcal{F}(t)$ is treated in the semi-classical dipole approximation, with the molecular dipole $\hat{\mu}$. The anti-commutator $[\hat{W}_{\mathrm{el}}, \hat{\rho}(t)]_+$ describes the coupling of the many-electron wave function with the TiO_2 bulk. Lindbald operators[121, 122, 123], $\hat{C}_{mn} = \frac{\sqrt{\Gamma_{nm}}}{2}|\Phi_n\rangle\langle\Phi_m|$, account for energy exchange between electronic states m and n at a rate Γ_{nm}. It is due to electron-vibration coupling in the titanium cluster. To drive the photo-induced injection electron dynamics, an external electric field with polarization along the cluster-dye direction is used

$$
\mathcal{F}(t) = F_0 \sin^2(\pi t/T)\sin\left(\omega_0(t - T/2)\right)
\tag{22}
$$

The frequency ω_0 is chosen for each functional to be resonant with the transition from the ground to the first optically active excitation. Realistic laser pulse

duration $T = 20 fs$ and amplitude $F_0 = 15 MV/cm$ are used throughout.

The many-body reduced density matrix operator $\hat{\rho}(t)$ is represented as a combination of many-body excited states, $\hat{\rho}(t) = \rho_{nm}(t)|\Phi_n\rangle\langle\Phi_m|$. The energies and coefficients of the many-body states are obtained from LR-TDDFT[115, 116, 117], which retain a pseudo-CIS structure. This hybrid TDDFT/CI method yields good balance between accuracy and computational efficiency. We introduce in this work a new quantitative measure of the electron injection rate into the titanium oxide bulk. A complex absorbing potential (CAP) is used to impose outgoing boundary conditions to the one-electron density. First, we represent each excited state using natural transition orbitals (NTO), obtained by singular value decomposition of the transition density matrix. This allows to define particle and hole orbitals for state n, which are then combined to form NTO particle ($\rho^{(n)}(\mathbf{r}_H)$) and hole ($\rho^{(n)}(\mathbf{r}_P)$) densities.

The NTO densities are used to quantify the coupling between an excited state to the TiO$_2$ bulk. The hole density in the systems studied is completely localized on the dye. Thus, only injection of the particle density is considered. The injection rate for a given many-electron state is evaluated as the expectation value of a transmission-free CAP over the particle density

$$W_n = \int \rho_p^{(n)}(\mathbf{r}_P)\Big(\frac{1}{1 - \zeta^4(\mathbf{r}_P)} - 1\Big) d\mathbf{r}_P \tag{23}$$

The CAP is defined from the surface normal $\mathbf{S_n}$ to the TiO$_2$ cluster boundaries, $\zeta(\mathbf{r}_P) = \big((\mathbf{r}_P \cdot \mathbf{S_n} - r_{\min})/(r_{\max} - r_{\min})\big)$. The parameters $\{r_{\max}, r_{\min}\}$ define the end of the integration grid along a given direction and the end of the cluster – here the titanium atom furthest from the interaction region.

The non-adiabatic coupling rates Γ_{mn} in Eq. (21) are approximated from first-order time-dependent perturbation theory [124, 125]

$$\Gamma_{mn} = \Big(\frac{\eta}{\hbar}\Big) L(\Delta_{mn}, \eta) P_m^{(\mathrm{cls})} P_n^{(\mathrm{cls})} \tag{24}$$

with Lorentzian broadening $L(\Delta_{mn}, \eta) = \frac{(\eta/2)^2}{(\Delta E_{mn})^2 + (\eta/2)^2}$, and the transition energies E_{mn} between states $|\Phi_n\rangle$ and $|\Phi_m\rangle$. A phonon broadening ranging from $\eta = \{0.1, 0.2, 0.3\}$ eV is chosen for all simulations. Vibrationally-induced relaxation occurs most efficiently via the TiO$_2$ vibrations within the cluster. Hence, the Lorentzian is multiplied by the projector of the particle on the cluster, $P_n^{(\mathrm{cls})}$, computed from the NTO particle densities as

$$P_n^{(\mathrm{cls})} = \int_{\mathrm{cluster}} \rho_p^{(n)}(\mathbf{r}_P) d\mathbf{r}_P \tag{25}$$

Dynamical simulations are performed using in-house codes [126, 118, 127, 119, 120]. For a more detailed description of the method, the reader is referred to the Supporting Information.

5.4 Computational Details

All electronic structure calculations were performed with the TURBOMOLE[128] modular program suite for *ab initio* quantum-chemical and condensed-matter simulations. The DFT and LR-TDDFT calculations were performed with seven different exchange-correlation functionals: PBE0 [22, 129], a modified PBE-based hybrid functional with 35% of exact exchange (referred to as PBE35), CAM-B3LYP[130], Lh12ct-SsirPW92[111], Lh12ct-SsifPW92[111], Lh07t-SVWN[96], and Lh07s-SVNW[108]. In our calculations we employed the def2-SVP basis set[131] and m3 grid size[132]. The dye- and dye@TiO$_2$-structures were taken from Ref. [82]. Additional optimizations were performed for the dyes with PBE0. Solvation effects are treated in the conductor-like screening model, COSMO, with standard settings for water as a solvent. All LR-TDDFT calculations for the D102@TiO$_2$ and JK2@TiO$_2$ systems are performed with all orbitals below the HOMO frozen, thus allowing for excitations from the HOMO only. Post-processing of the TURBOMOLE data for the subsequent electron dynamics calculations was performed with ORBKIT[133, 134, 135], a parallel Python program for post-processing wave function data from standard quantum chemical programs.

5.5 Results

5.5.1 Static

A reliable protocol for the characterization of DSSC models should provide results with the same accuracy for the separate systems, i.e. the dyes and the TiO$_2$ cluster, and their combination. We compare therefore three different energetic properties calculated with the local hybrid functionals and some more usual ones as a benchmark to experimental values: the first lowest-energy excitation in the dye alone and when grafted on the semiconductor, the HOMO-LUMO gap in the TiO$_2$ cluster, and the level alignment from LR-TDDFT calculations in the dye@TiO$_2$-system. To get insight into the effect of solvation on the energetics, we also present results in the gas phase.

Table 1: Absorption maxima (in eV) from LR-TDDFT calculations for the free D102 dye and for D102@TiO2, in the gas phase and including solvent effects via COSMO. Results are showing the lowest dye - dye excited state. The amount of exact exchange for Lh07s-SVWN is given in parenthesis. Experimental results are taken from Refs. [136] and [97], respectively.

	gas phase		in water	
	D102	D102@TiO2	D102	D102@TiO2
PBE0	2.59	1.95	2.36	2.51
PBE35	2.80	3.10	2.58	2.79
CAM-B3LYP	2.92	3.49	2.80	3.32
Lh12ct-SsirPW92	2.66	2.70	2.42	2.53
Lh12ct-SsifPW92	2.71	2.85	2.48	2.66
Lh07t-SVWN	2.50	2.42	2.27	2.22
Lh07s-SVWN (0.22)	2.51	2.63	2.28	2.45
Lh07s-SVWN (0.10)	2.22	1.91	1.99	/
Lh07s-SVWN (0.30)	2.67	2.74	2.44	2.62
exp.			2.53	2.30

Starting with the D102 dye, Table 1 reports the calculated lowest-energy excitation energies for the isolated and TiO_2-anchored dye molecule for different XC functionals, in comparison to experimental values obtained in EtOH. Overall, the range-separated functional CAM-B3LYP yields the highest excitation energies for the dye and the dye@TiO_2 system. Increasing the amount of exact exchange in a global hybrid functional (from 25 to 35% in PBE0 and PBE35, respectively) leads, as expected, to larger excitation energies. This is in agreement with the well-known requirement to include exact exchange to describe CT-like excitations. Inclusion of the solvents through the COSMO model leads to consistently decreasing excitation energies of roughly 0.2 eV. Here, the smallest effect is observed for CAM-B3LYP which is probably due to smaller hybridization between dye and cluster orbitals. In water, the best agreement of the excitation energy with the experimental value is obtained with PBE35, while it is significantly overestimated with CAM-B3LYP. All other functionals underestimate the excitation energy as compared to the experimental value. Keeping in mind that CAM-B3LYP uses between 65% exact exchange (at large interelectronic distances) and 19% (at short interelectronic distances) with a range-separation parameter of 0.33 Bohr^{-1}, it probably uses overall more exact exchange than PBE35, especially in regions relevant to describe the interface between the organic dye and the TiO_2 cluster. Focusing on the results with local hybrids, we observe that for the D102 dye in water, the t-LMF performs clearly better than the s-LMF. For both types, a trend similar to global hybrids can be observed: the calculated excitation energy decreases with the maximum amount of exact exchange used in the core and asymptotic regions. In the t-LMF based functionals it is largest in the Lh12ct-SsifPW, followed by Lh12ct-SsirPW and then Lh07-SVWN with values of 0.709, 0.646, and 0.48, respectively.

Table 2: Absorption maxima (in eV) from LR-TDDFT calculations for the free JK2 dye and for JK2@TiO$_2$, in the gas phase and including solvent effects via COSMO. Results are showing the lowest dye - dye excited state. The amount of exact exchange for Lh07s-SVWN is given in parenthesis. Experimental results are taken from Refs. [136] and [97], respectively.

	gas phase		in water	
	JK2	JK2@TiO2	JK2	JK2@TiO2
PBE0	2.04	1.94	1.87	1.81
PBE35	2.25	2.29	2.10	2.14
CAM-B3LYP	2.56	3.09	2.43	3.00
Lh12ct-SsirPW92	2.11	2.05	1.93	1.88
Lh12ct-SsifPW92	2.16	2.14	2.00	2.01
Lh07t-SVWN	1.94	1.72	1.76	1.53
Lh07s-SVWN (0.22)	1.95	1.79	1.78	1.67
Lh07s-SVWN (0.10)	1.66	1.33	1.48	1.05
Lh07s-SVWN (0.30)	2.12	2.13	1.95	1.99
exp.			2.84	2.70

Looking at the combined dye-semiconductor systems, the most accurate results are obtained with the Lh07t-SVWN functional. It underestimates the experimental excitation energy by only 0.08 eV, while all other functionals (except the one with a modified s-LMF) overestimate it. The CAM-B3LYP functional yields the largest deviation of roughly 1 eV from the experimental result. An optimal amount of exchange to describe the lowest excitation in the D102@TiO$_2$ system would be significantly below 25 % but close to 35 % for the dye alone. It becomes clear from the local hybrid results, that in particular the optimal prefactor in the t-LMF should be lower for the combined systems than for the dye. Yet, the local hybrids with reduced self-interaction (Lh12-SsirPW92 and Lh12-SsifPW92) provide a good compromise although it was initially optimized for thermochemical ground state properties of small molecules.

Turning to the larger dye, JK2 (cf. Table 2), we observe a general underestimation of the lowest excitation energy with all functionals. This is even more pronounced with the solvation model, as it lowers all energies, although to a smaller extent than for the smaller dye. CAM-B3LYP yields the closest value to the experiment but with a rather large deviation of more than 0.4 eV. A possible explanation for this failure of all functionals may be an unreasonable structure used for the dye alone, which was here obtained by simply removing the cluster from the optimized dye@TiO$_2$ geometry. For the lowest excitation energy in the dye attached to the TiO$_2$ cluster, CAM-B3LYP performs best but with a considerable overestimation of the transition energy of 0.3 eV. All the other functionals severely underestimate the excitation energy, with deviations between 0.7 and 0.8 eV for the two best local hybrids (SI-free and SI-reduced local correlation at short range). Judging from the PBE0 and PBE35 (35% of exact exchange) results, a much larger amount of exact exchange would be

Table 3: Absorption maxima (in eV) from LR-TDDFT calculations for the free D102 and JK2 dyes, in the gas phase and including solvent effects via COSMO. The ground state geometry has been reoptimized at the PBE0/def2-SVP level of theory, with and without solvent. Results are showing the lowest dye - dye excited state. The amount of exact exchange for Lh07s-SVWN is given in parenthesis. Experimental results taken from Refs. [136, 137]. The amount of exact exchange in the Lh07s-SVWN is given in parenthesis.

	gas phase		in water	
	D102	JK2	D102	JK2
PBE0	2.65	2.19	2.45	2.06
PBE35	2.89	2.47	2.69	2.35
CAM-B3LYP	3.05	2.86	2.88	2.76
Lh12ct-SsirPW92	2.72	2.28	2.51	2.15
Lh12ct-SsifPW92	2.77	2.35	2.57	2.22
Lh07t-SVWN	2.57	2.08	2.36	1.93
Lh07s-SVWN (0.22)	2.57	2.09	2.36	1.95
Lh07s-SVWN (0.10)	2.29	1.73	2.09	1.57
Lh07s-SVWN (0.30)	2.74	2.31	2.53	2.17
exp.			2.53	2.84

required to obtain reasonably accurate results with a global hybrid functional.

To shed light on the origin of the large deviations in the lowest excitation energy of the JK2 dye, we have reoptimized the structure of both dyes with PBE0 in water. The corresponding excitation energies obtained with all XC functionals are shown in Table 3. For the smaller dye, the effect on the resulting energies is less pronounced. All excitation energies are increased by approximately 0.1 eV and the best agreement with the experiment is now obtained by the local hybrid with reduced SI in the correlation (Lh12-SsirPW92). The increase in the excitation energies is more distinct in case of the JK2 dye. After optimization, CAM-B3LYP provides an excitation energy of 2.76 eV which is in good agreement with the experimental value of 2.84 eV.

Semilocal XC functionals famously underestimate the band gap in semiconductors and a certain amount of exact exchange is usually needed to obtain reasonable band gaps with DFT.[139, 140] To assess the performance of local hybrids for the semiconductor part of our DSSC models, we compare the calculated HOMO-LUMO gaps to the experimental band gap of TiO_2 in Table 4. First, we note that with COSMO, the HOMO-LUMO gaps are by 0.3 to 0.4 eV larger than in the gas phase. This is probably due to the finite size of the cluster. In the gas phase, the best agreement with the experimental band gap of 3.2 eV is accomplished with Lh07s-SVWN (3.50 eV). This particular local hybrid uses a LMF based on the (reduced) density gradient which in turn has been used before to estimate a 'local' band gap in a series of semiconductors and insulators.[141] This kind of LMF seems to be therefore particularly suited for the semiconductor. The s-LMF contains one parameter (set to 0.22 by default)

Table 4: Experimental and theoretical band gap (in eV) for the semiconductor TiO_2 in ground state gas phase (gas) and solvent (sol). Experimental results from Ref. [138]. The adjusted parameter in Lh07s-SVWN is given in parenthesis.

	TiO_2^{gas}	TiO_2^{sol}
PBE0	3.78	4.15
PBE35	4.68	5.08
CAM-B3LYP	6.76	7.09
Lh12ct-SsirPW92	4.20	4.57
Lh12ct-SsifPW92	4.45	4.83
Lh07t-SVWN	3.54	3.88
Lh07s-SVWN (0.22)	3.50	3.82
Lh07s-SVWN (0.10)	2.51	2.79
Lh07s-SVWN (0.30)	4.16	4.51
exp.	3.20	3.20
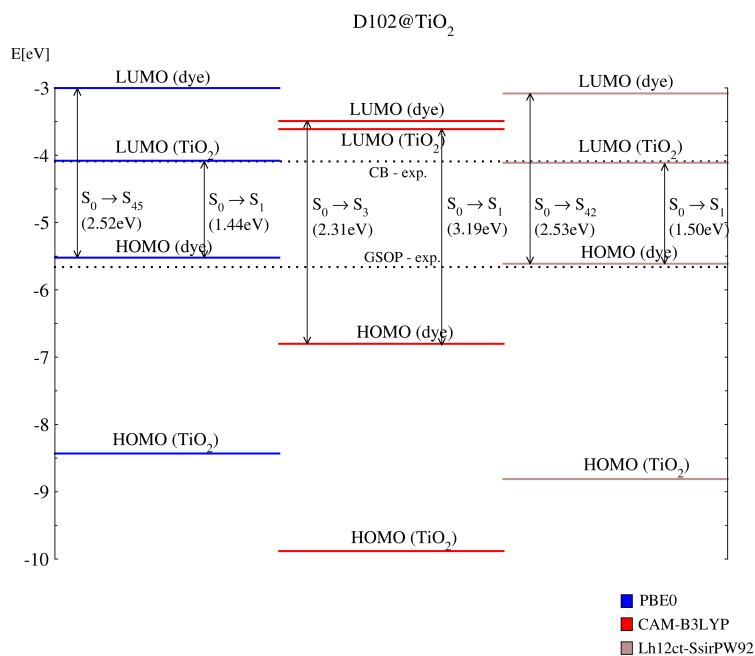
Figure 4: Alignment of the energy levels in the D102@TiO$_2$ system in water from LR-TDDFT-COSMO calculations with three different functionals labeled in the figure: PBE0, CAM-B3LYP and Lh12ct-SsirPW92. Black dotted lines indicate the experimental TiO$_2$ CB edge and dye's ground state oxidation potential (GSOP).

related to the slope of the LMF between the limiting values of 0 and 1. The larger the parameter the more exact exchange is used on average. Consequently, the HOMO-LUMO gap opens, as confirmed by additional calculations with a modified parameter inside the s-LMF. The respective band gaps are 2.79 eV and 4.51 eV with the parameter set to 0.1 and 0.3. An optimal value for the TiO_2 would thus lie somewhere between 0.22 and 0.1. We have also recalculated the properties of the dyes with these two modified local hybrids based on the s-LMF. The one with 0.3 yields exactly the experimental excitation energy of the smaller D102 dye and is also among the best local hybrids for the larger JK2 dye alone and in combination with the TiO_2 cluster.

After assessing the functionals for the properties of the individual constituents of our DSSC model systems, we chose three representatives to analyse the level alignment at the dye-semiconductor interface. The level alignment is visualized in Figs. 4 and 5 for the PBE0 as a standard global hybrid, CAM-B3LYP as a standard range-separated hybrid, and the local hybrid functional Lh12ct-SsirPW92. The latter provides the best balance in the description of the D102 dye alone and in combination with the semiconductor. For the JK2 dye it performs similarly to the best local hybrid Lh12ct-SsifPW92. The level alignment with the latter is comparable (see supporting information). In both figures, we note that the local hybrid gives HOMO energies in excellent agreement with the experimental ground state oxidation potentials (GSOP). The energy of the LUMO located on the TiO_2 (corresponding to the first excited state in the LR-TDDFT calculation for the combined system) is also very close to the experimental CB edge with PBE0 and the local hybrid. Although our calculations showed an underestimation of the first excitation energy in the case of JK2 alone and JK2@TiO_2, still the correct level alignment is obtained. The performance of the local hybrid is similar to PBE0. The number of the TDDFT excitations required to reach the lowest dye-dye excitation is significantly smaller in the case of JK2@TiO_2, for the same functional, as can be seen from the Fig. 4 and Fig. 5. From Fig. 5 we can notice that CAM-B3LYP yields a wrong level alignment at the interface between JK2 and the semiconductor: the dye-HOMO lies below the TiO_2-LUMO, confirming previous findings.[82] As will be shown below, this will have a strong influence on the laser excitation and charge injection dynamics.

JK2@TiO$_2$

E[eV]

-3

LUMO (TiO$_2$)

LUMO (dye)   LUMO (dye)   LUMO (dye)
LUMO (TiO$_2$)   LUMO (TiO$_2$)

-4

CB - exp.

$S_0 \to S_{12}$ $S_0 \to S_1$ $S_0 \to S_2$ $S_0 \to S_1$ $S_0 \to S_{12}$ $S_0 \to S_1$
(1.81eV)   (1.41eV)   (3.53eV)   (2.99eV)   (1.88eV)   (1.48eV)

-5

HOMO (dye)

GSOP - exp.

HOMO (dye)

-6

HOMO (dye)

-7

HOMO (TiO$_2$)

-8

HOMO (TiO$_2$)

-9

HOMO (TiO$_2$)

-10

■ PBE0
■ CAM-B3LYP
■ Lh12ct-SsirPW92
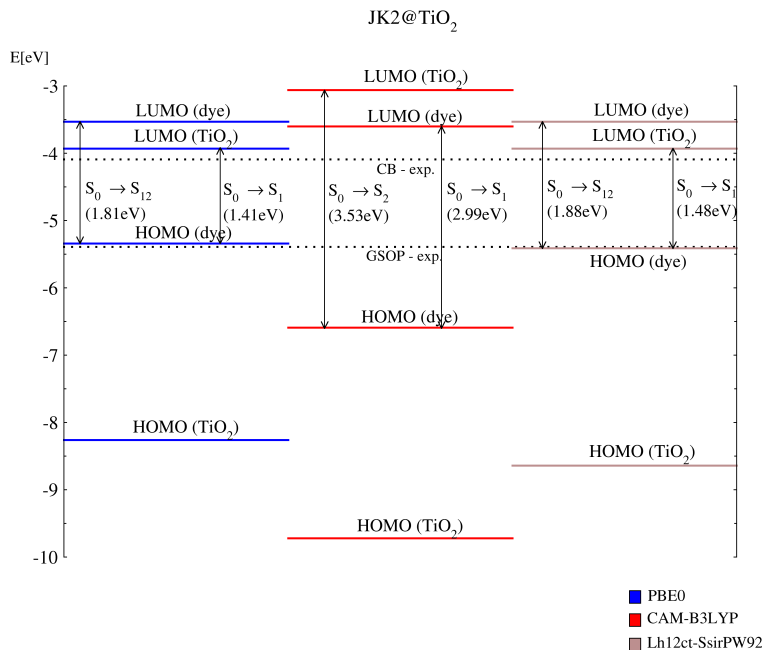
Figure 5: Alignment of the the energy levels in the JK2@TiO$_2$ system in water from LR-TDDFT-COSMO calculations with three different functionals labeled in the figure: PBE0, CAM-B3LYP and Lh12ct-SsirPW92. Black dotted lines indicate the experimental TiO$_2$ CB edge and dye's ground state oxidation potential (GSOP).

5.5.2 Dynamics

To shed light on the effect of the level alignment on the photoinduced charge injection, we investigate the dynamics upon excitation by a short laser pulse. To this end, the CAM-B3LYP and Lh12ct-SsifPW92 functionals are used. As described above, the former shows a poor alignment of the TiO$_2$ conduction band to the first optically accessible band corresponding to the HOMO-LUMO excitation located on the dye. The poor description of TiO$_2$ using the range-separated hybrid shifts the conduction band upwards, and the first bright state of the dye does not hybridize strongly with the titanium dioxide cluster. As will be shown below, this also has an influence on vibration-induced population of the TiO$_2$ conduction band. On the contrary, the level alignment is much more realistic using the Lh12ct-SsifPW92 functional, with a more pronounced dye-cluster hybridization.

The pulse parameters are described in the caption of Figs. 6 and 7 and chosen to represent a realistic experimental setup. The relatively low field amplitude of $F_0 = 15\,\mathrm{MV/cm}$ leads to a peak intensity of $I_{\mathrm{peak}} = 0.5c\varepsilon_0 F_0^2 =$
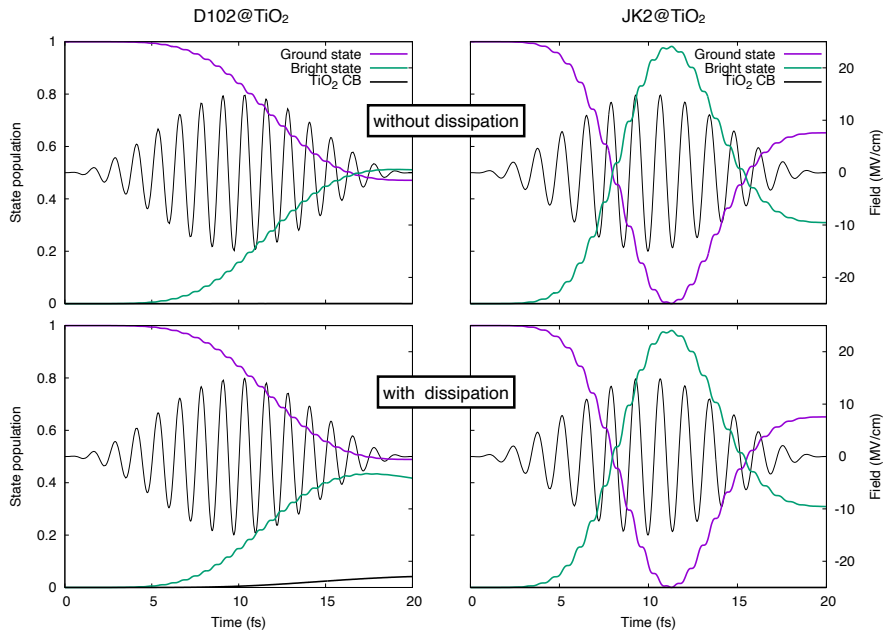
Figure 6: Population dynamics of selected states upon excitation of two dyes (D102 and JK2) on titanium dioxide using a sine-squared laser pulse of duration 20 fs and maximum amplitude 15 MV/cm, polarized along the cluster-dye direction. For the dynamics simulations, the lowest-lying $N_{\mathrm{states}} = 38$ ($N_{\mathrm{states}} = 15$) excited states up to an energy of 4.27 eV (3.97 eV) computed using CAM-B3LYP are used for dye D102 (JK2). The states labeled "TiO_2 CB" describe states of the conduction band for which the particle is localized on the cluster. The frequency of the laser pulse is chosen resonant with the transition from the ground to the bright state, which amounts to $\hbar\omega = 3.32$ eV and $\hbar\omega = 2.99$ eV for D102 and JK2, respectively. The resulting field is depicted as a thin black line. Top panels: dynamics without dissipation. Bottom panels: dynamics with a vibration-induced broadening $\eta = 0.2$ eV.

3.0×10^{11} W/cm^2. For this peak intensity, little to no electron loss through ionisation can be expected. In each case, the field frequency is chosen resonant with the transition from the ground to the first bright state or, in the case JK2@TiO_2 described with the Lh12ct-SsifPW92 functional, the first group of optically accessible states.

The population dynamics of the ground and first bright state during laser irradiation is reported in Fig. 6 for the case of CAM-B3LYP. The driving field is shown as a thin black line to guide the eye and illustrates the origin of small oscillations observed in the populations as a response. The frequency of the electric field is related to the energy difference between the ground and target state, $\Delta E_{mn} = \hbar\omega_{mn}$.

28

Without vibration-induced relaxation (top panel), only the optically-active target becomes significantly populated in both cases. The transition dipole of JK2@TiO$_2$ is much larger than for D102@TiO$_2$. This is indicative of a stronger degree of charge separation along the cluster-dye direction in the excited state. Consequently, the excitation probability becomes much larger because of the increased coupling to thee external electric field. This leads to a larger population of the excited state, which reaches a crossover point and undergoes an almost complete first Rabi cycle. It is known that excitation using short, intense laser pulses along the dipole direction leads to important non-linear dynamical effects. These can be treated variationally by including a large number of pseudo-CIS states in the basis used for the dynamics. Because the number of states remain modest in the present simulations, the results should be interpreted with care.

Comparison with the case where energy relaxation is included (broadening $\eta = 0.2\,\text{eV}$ and $T = 300$K), does not reveal any change in the dynamics for JK2@TiO$_2$. This is because of the poor band alignment of the dye excited state and the TiO$_2$ conduction band with CAM-B3LYP, associated with a weak hybridization due to the small density of TiO$_2$ states at the correct energy. While the overall dynamics for the D102 dye are also almost unaffected by the inclusion of vibrationally-induced energy relaxation, some states of the TiO$_2$ conduction band becomes populated (black line in the bottom left panel of Fig. 6). This is accompanied by a depopulation of the excited state (green line), which is visible at the end of the pulse. Although this indirect mechanism is typical of type II DSSC, it is found to be very inefficient when the electronic structure is characterized using the CAM-B3LYP functional.

The picture proposed by the dynamics at the Lh12ct-SsifPW92 level of theory is quite contrasting. The resulting population evolution under application of similar laser pulses as above is shown in Fig. 7 (see figure caption for the pulse parameters). For the D102 dye, the dynamics without energy relaxation (top left panel) already show an important population of the TiO$_2$ conduction band during the laser pulse excitation. This represents a more pronounced direct electron transfer character in this case, due to the stronger hybridization and the larger cross section for the direct excitation from the dye-HOMO to the substrate. Allowing for vibration-induced relaxation increases the importance of the indirect electron transfer from the D102 dye to the TiO$_2$ conduction band, as can be seen in the bottom left panel of Fig. 7. Vibration-induced energy redistribution leads to a rapid transfer of the electron from the strongly hybridized dye-LUMO to the cluster. This comes at the expense of a smaller overall depopulation of the ground state (purple line) and a less efficient population of the excited state (green line), both compared with the CAM-B3LYP dynamics and the case without energy dissipation.

The JK2 dye behaves even more differently at the Lh12ct-SsifPW92 than at the CAM-B3LYP level of theory. The first obvious difference stems from the increased density of TiO$_2$ states around the LUMO of the dye, which amounts to a spreading of the bright state among at least three dominant contributions. All three are significantly populated during the laser excitation, as can be seen from the top right panel of Fig. 7. During the excitation, the ground state is almost
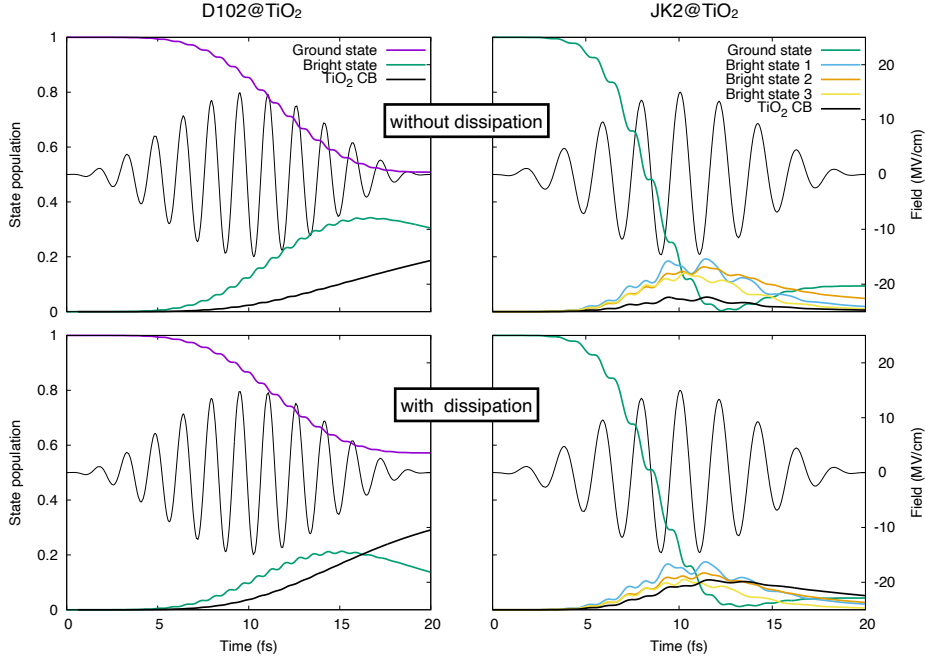
Figure 7: Same as for Fig. 6 but using the Lh12ct-SsifPW92 functional. For D102, the energy of the laser pulse is chosen resonant with the transition from the ground to the bright state, which is $\hbar\omega = 2.66\,\text{eV}$. For JK2, the average frequency $(1.98\,\text{eV})$ of the three bright states strongly hybridized with the TiO_2 cluster of the first absorption band is used. For the dynamics simulations, the lowest-lying $N_{\text{states}} = 45$ $(N_{\text{states}} = 20)$ excited states up to an energy of $2.73\,\text{eV}$ $(2.22\,\text{eV})$ are used for dye D102 (JK2). The top and bottom panels report the dynamics without and with a vibration-induced broadening $\eta = 0.2\,\text{eV}$ at $T = 300\text{K}$.

completely depopulated due to the stronger transition dipole to the bright states as compared with the D102 dye. Contrary to the CAM-B3LYP situation, the system does not undergo a full Rabi cycle and some hybridized states of the TiO_2 conduction band (thick black line) are directly photoexcited. The frequency of the transition is also markedly smaller than in D102, as can be directly seen from the reported field (thin black line). As in the case of D102, vibration-induced relaxation leads to an increased population of the TiO_2 conduction band (see bottom right panel). On the contrary, including energy dissipation leads to a more important depopulation of the ground state for the JK2 dye excitation, which appears to land mostly in the TiO_2 conduction band. This will be seen to have an effect on the electron injection efficiency.

The anti-commutator in Eq. (21) leads to a loss of norm in the many-body reduced density matrix, which is due to the presence of the CAP in the equations-
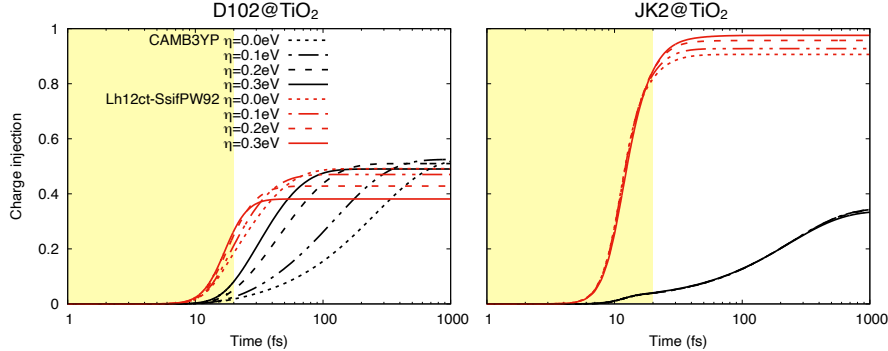
Figure 8: Charge injection dynamics for the D102 and JK2 dyes adsorbed on TiO_2 upon laser excitation. The injection efficiency with various vibrational broadening is reported in black and red for the Lh12ct-SsifPW92 and CAM-B3LYP functionals, respectively. The yellow shaded areas represent the interval during which the pulses are applied (see Figs. 6 and 7 for the pulse parameters).

of-motion. This absorption through the CAP is related to the loss of an excited particle, and it can be assimilated to the injection of an electron into bulk TiO_2. Fig. 8 reports the charge injection efficiency for D102@TiO_2 (left panel) and JK2@TiO_2 (right panel) for different dissipation strengths. The results are reported in black for the CAM-B3LYP functional and in red for the local hybrid Lh12ct-SsifPW92. The shaded area represents the interval during which the external field is on. For the D102 dye, most of the charge injection takes place after the pulse has been switched off, although this is more pronounced at the CAM-B3LYP level of theory. Using this functional, gradually increasing the dissipation strength from $\eta = 0$ (dotted line) to $0.3\,eV$ (solid line) accelerates the charge injection from about 1ps to about 50fs duration. The charge injection yield is not markedly affected and remains around 50% for all relaxation times investigated. This correlates well with the population dynamics observed in Fig. 6, which reveals a change from a direct excitation of the dye LUMO when neglecting dissipation to an indirect charge injection via the TiO_2 conduction band via vibration-induced energy redistribution.

To understand the interplay between band alignment, hybridization, relaxation, and charge injection, Fig. 9 shows the projected NTO particle density for the lowest-lying states for both dyes. For D102, the first bright state can be readily identified as a large peak in both spectra. It reaches a larger value of about 1 and slightly above 0.8 for CAM-B3LYP and Lh12ct-SsifPW92, respectively. This indicates a strong degree of localization on the dye and weak hybridization with the TiO_2 conduction band. As a consequence, very little coupling to the titanium dioxide bulk – and with a low charge injection – is expected. At the CAM-B3LYP level of theory, the first bright state is found to be located very low within the conduction band, in a region of low density of states. This implies that energy will not have many lower-lying states to dissipate the energy, as the
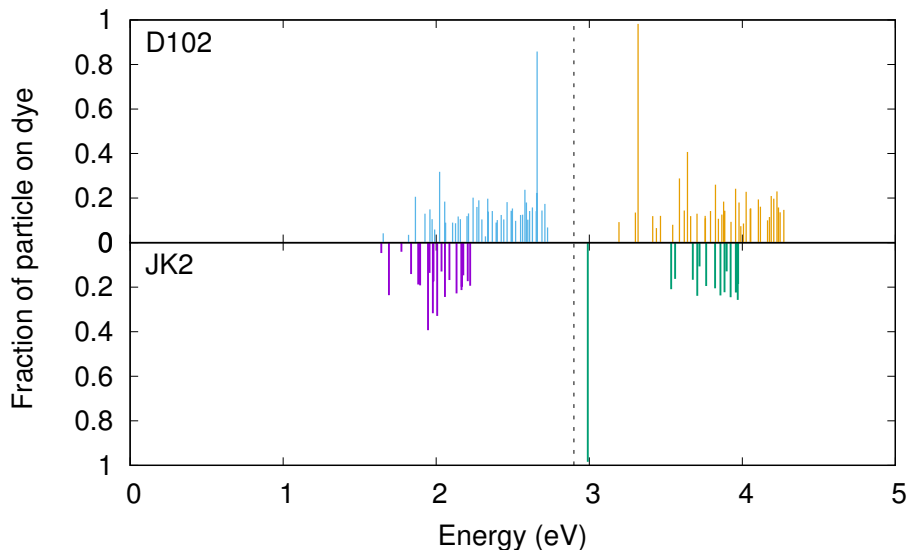
Figure 9: Projection of the NTO particle density on the dye evaluated as the complement to Eq. (25), $1 - P_n^{(\text{cls})}$. The lowest-lying excited states obtained from the Lh12ct-SsifPW92 (blue for D102, purple for JK2) and CAM-B3LYP functionals (yellow for D102, green for JK2) are reported to the left and right of the vertical dashed line, respectively.

density of states is low. Despite being still relatively localized on the dye, the bright state of D102 computed at the Lh12ct-SsifPW92 level of theory is found in a region of the conduction band with higher density of states. This leads to stronger hybridization and increased potential for vibration-induced energy redistribution.

From a dynamical perspective, slow charge injection has to be expected for the D102 dye when studied at CAM-B3LYP level of theory, since the LUMO is more strongly localized on the dye and only weakly interacts with the absorbing potential. As the conduction band becomes populated via energy relaxation, these strongly delocalized states interact more with the absorbing potential and charge injection becomes faster. A similar acceleration of the charge injection dynamics, as a function of the increased dissipation strength, is also observed at Lh12ct-SsifPW92 level of theory, even if at a lesser extent. The larger density of states close to the dye LUMO leads to a stronger hybridization of all states within the conduction band. This, in turn, leads to a delocalization of the particle density over the whole cluster and to a faster overall charge injection rate, such that most of the charge departs by the end of the pulse and within the 20fs following the excitation. The reduction in the charge transfer efficiency observed

with increasing dissipation rate originates solely from the smaller depopulation of the ground state.

The case of JK2@TiO$_2$ is quite different (right panel of Fig. 8). As can be expected from the population dynamics at the CAM-B3LYP level of theory (see Fig. 6), increasing energy relaxation has no effect on the charge injection rate (black lines). This is due to the poor TiO$_2$ band alignment with the dye LUMO, which appears now below the CB states and is completely localized on the dye (see green lines in Fig. 9). The charge injection dynamics reveal two timescales: an ultrafast one during the excitation with the external electric field, and a longer one on the order of 1ps stemming from the slow population leakage from the excited state with LUMO character into the TiO$_2$ bulk. At the Lh12ct-SsifPW92 level of theory, the charge injection proceeds on the timescale of the laser excitation and it is mostly completed by the end of the pulse. The efficiency is high (circa 90%) even without accounting for vibration-induced relaxation. Contrary to the D102 case, increasing energy dissipation also increases the charge injection efficiency while not accelerating the charge injection rate. As the vibrational broadening reaches its largest value, charge injection is almost complete (solid red line). This can be traced back to the more quantitative depopulation of the ground state during the excitation, as seen in the bottom right panel of Fig. 7. Further, the indirect population of the TiO$_2$ conduction band via excitation of the strongly hybridized bright states becomes more efficient and, with it, the coupling of the excited states with the bulk. The better band alignment obtained from the Lh12ct-SsifPW92 functional and the stronger hybridization observed in Fig. 9 (purple lines) thus leads to a markedly different picture for the electron injection efficiency and the associated rates.

5.6 Conclusion and Outlook

In this work we investigated the potential of local hybrid functionals to characterize the electronic structure of two highly efficient organic dyes (D102 and JK2) for applications in DSSCs, both free-standing and anchored to a semiconductor (TiO$_2$). To get deeper understanding of band alignments effect on the photo-induced charge dynamics we used hybrid TDDFT/CI method with two functionals, CAM-B3LYP and Lh12ct-SsifPW92. When it comes to the absorption maxima of the smaller dye alone (D102) and with the semiconductor (D102@TiO$_2$), the presented local hybrid functionals are showing great accuracy, especially in the gas phase. In the solvent, their accuracy can be compared with hybrid functionals with adjusted value of exact exchange like PBE35 (35% of exact exchange). Inherently, the well-established range-separated functional CAM-B3LYP is overestimating the experimental values, which points at the negative influence of excessive exact exchange admixture in the functional. The optical excitation in the larger dye (JK2) is significantly underestimated in all cases, except with CAM-B3LYP, which is also the most accurate value in comparison to the other used functionals. Level alignment analysis showed that PBE0 and two local hybrids provide sufficient accuracy with respect to the CB of the TiO$_2$ and ground state oxidation potential. This is the case with both sys-

tems. Interestingly, CAM-B3LYP yields a wrong and unphysical level alignment for the bigger dye (JK2), where the HOMO of the dye lies below the LUMO of the TiO$_2$. This is an indication of the wrong description of the asymptotic behavior in systems with pronounced long-range charge transfer character. When we isolate and optimize D102 in water, there is an excellent agreement with the experimental value in the lowest absorption maxima in the case of an adjusted local hybrid functional Lh07s-SVWN (0.3), while Lh12ct-SsifPW92 and Lh12ct-SsirPW92 are very close to the actual value. Results for the band gap of TiO$_2$ are highly overestimated with all of the functionals except for a slightly adjusted local hybrid with a LMF based on the reduced density gradient. Concerning the development of refined local hybrid functionals, further improvement for dyes stronger charge separation in their first excited state could be obtained by incorporating additional long-range exact exchange into local hybrids. At the same time more information on the performance of local hybrid functionals for semiconductors is required to make necessary adjustments to the LMF.

The electron dynamics simulations reveal a considerable dependence on the XC functional used for the underlying electronic structure calculation. In particular for the JK2@TiO$_2$ system, the qualitatively different level alignment obtained from CAM-B3LYP, as compared to the local hybrid Lh12ct-SsifPW92, is correlated with larger injection times and a lower overall charge injection. With Lh12ct-SsifPW92 functional the JK2 dye showed an increased density of TiO$_2$ states around LUMO, while the ground state is completely depopulated due to the strong transition dipole moment. This is not the case with D102 where the population of the ground state is only reduced to about 50 % (with both functionals). The calculated charge injection efficiency showed that for D102 most of the injection takes place after switching off the pulse of the external field, which is more pronounced with CAM-B3LYP. Projection of D102 NTO particle densities with CAM-B3LYP and D102 case implied that the energy will not have many channels to dissipate, while Lh12ct-SsifPW92 functional showed stronger hybridization and an increased potential for vibration-induced energy redistribution. In case of JK2 with CAM-B3LYP, increasing relaxation has no effect on the charge injection rate due to the poor TiO$_2$ level alignment with the dye LUMO, fully localized on dye, appearing below the semiconductor CB levels. With the Lh12ct-SsifPW92 functional, charge injection will proceed through the end of the pulse with high efficiency.

5.7   Declaration of Competing Interest

The authors declare that they have no known competing financial interests or personal relationships that could have appeared to influence the work reported in this paper.

5.8   Acknowledgements

5.9   Appendix A. Supplementary material

Supplementary data associated with this article can be found, in the online version, at https://doi.org/10.1016/j.chemphys.2022.111521.

6 Electronic structure in organic dye-sensitized solar cells: Insight from density functional theory and electron dynamics

CRediT authorship contribution statement

Dejan Gemeri: Conceptualization, Calculations, Data curation, Writing - original draft.

6.1 Abstract

Recently, local hybrid density functionals have been assessed in conjunction with electron dynamics to simulate the charge injection at two dye-semiconductor interfaces (Chem. Phys. 559, 111521, 2022). Building on these results for two typical dyes, this work extends the application of this method to several double-donor dyes with a central triphenylamine-unit. Energies of excited states are approximated by linear-response time-dependent density functional theory and the laser-induced charge-injection is subsequently simulated with the time-dependent configuration-interaction methodology. Our findings confirm a significant dependence of the level alignment at the interface and the degree of hybridization of dye and semiconductor states on the underlying exchange-correlation functional. Consequently, the charge injections calculated using different functionals vary qualitatively and quantitatively. In comparison with standard global or range-separated hybrid functionals, the local hybrid functionals provide an overall more balanced description of excited states in the dyes and the dye-TiO_2 system if a sizable cluster model for the semiconductor is employed.

6.2 Introduction

Harvesting solar energy offers a clean alternative source of energy to fossil fuels, which are responsible for greenhouse emissions at the center of the current energy crisis [142]. Third generation photovoltaic cells such as dye-sensitized solar cells (DSSCs) demonstrated great potential and are strong candidates for commercial applications [7, 8]. In particular, metal-free organic dyes are attracting

lots of attention since they are environment-friendly and easy available. However, the highest incident Photon-to-Current Efficiency (PCE) for this family of dyes is 12.5%[143] and the search for more efficient DSSCs remains an active field of research, which is often assisted by theoretical studies.

A crucial step for the optimization of metal-free organic DSSCs is the creation and separation of charge carriers at the hybrid organic-semiconductor interface.[66]. For indirect injection cells, sunlight falls onto the device and excites first the electrons from the highest occupied molecular orbital (HOMO) to the lowest unoccupied molecular orbital (LUMO) of the dye. The orbital pair is mostly localized close to the acceptor anchoring group, directly bound to the conduction band of the semiconductor. Depending on the alignment of the electronic levels of the semiconductor conduction band and of the dye LUMO, this may lead to a strong hybridization at the interface and an important variation of the charge injection efficiency. From a theoretical perspective, optimization of DSSCs thus requires an accurate description of the electronic structure of both the free dye and of the organic-semiconductor interface.
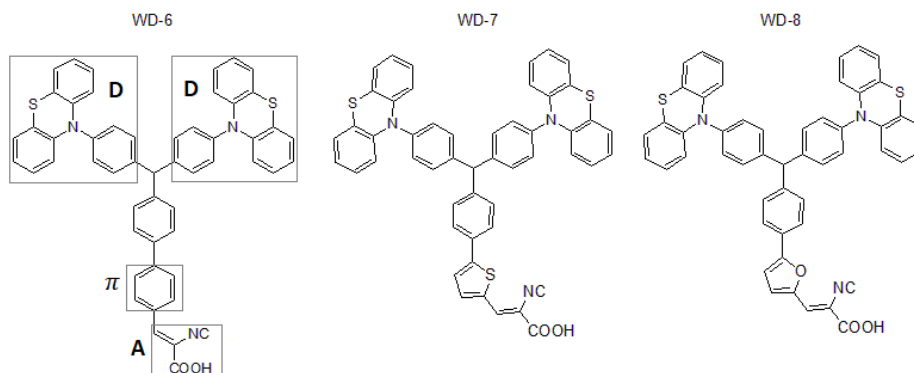
Figure 10: Molecular structures of the three organic dyes labeled WD-6, WD-7, and WD-8. All presented dyes have the same donor and acceptor groups, but different conjugated linker: benzene, thiophene, and furan (from left to right). Individual parts of the first molecule (D-donors, π-linker and A-acceptor) are marked with rectangles.

A promising design for efficient organic dyes adopts a donor-acceptor structure connected through a delocalized π linker (D-π-A). By incorporating an additional donor, leading to a D-D-π-A structure, PCEs can be improved through broadening and intensifying the dye absorption spectrum and preventing dye aggregation[144, 145]. Our investigation builds on two experimental and theoretical studies for such double donor systems attached to titania (TiO$_2$) as a semiconductor. Photovoltaic performaces for three double donor dyes with varying conjugated linker groups (benzene, thiophene, and furan, see Fig.10) were reported.[146]. Identifying furan as the best linker, another series of dyes was designed using DFT (see Fig.11) by systematically varying the donor groups.

Based on ground state calculations with periodic boundary conditions for the dyes attached to a TiO_2 surface, the phenothiazine donor was identified as the most promising candidate[147]. To simulate the UV-Vis spectra of the combined system a single TiO_2 unit was employed.
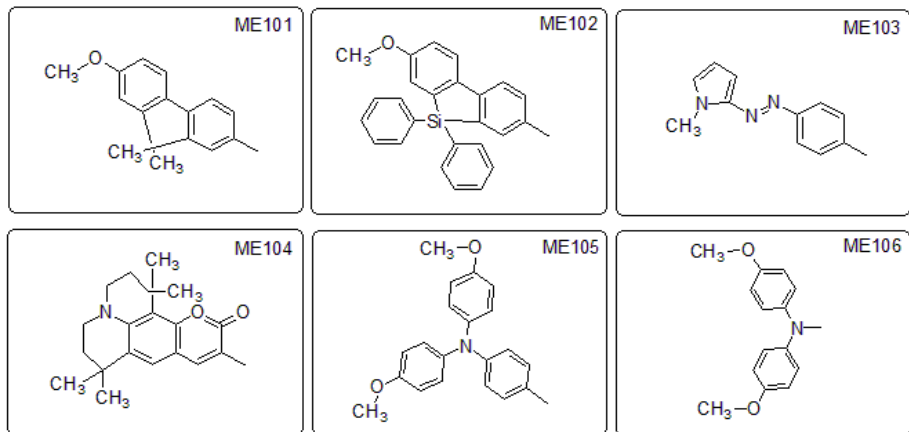
Figure 11: Molecular structures of various dyes derived from the WD-8 structure (see Fig.10). The anchoring furan group remains unchanged while the donor part is changed for every different structure. The dyes are labeled ME101-ME105 in the following.

In the present work, we investigate theoretically all aforementioned dyes attached to a sizeable $(TiO_2)_{38}$ cluster using a combination of density functional theory (DFT) [1, 2], linear response time-dependent DFT (LR-TDDFT) in the Casida framework [148, 34], and many-electron dynamics[117, 115, 116].

In a previous study, [149], we have assessed the performance of local hybrid density functionals for DSSC models and dependence of electron dynamics on the exchange-correlation functional. The rather recent family of exchange-correlation functionals, appear to be favourable for the description of hybrid organic-inorganic DSSC interfaces for two prototypical dyes. In the present study our approach is extended to the aforementioned double-donor dyes.

This paper is organized as follows. The methods used in this work and the associated computational details are summarized in Section 5.3. Section 5.4 reports on the performance of the local hybrid functionals for the static properties in the different DSSC models. Simulations of the laser-induced electron injection dynamics are presented and discussed in section 5.5, which is followed by general conclusions.

6.3 Methods and Computational Details

All electronic structure calculations were performed with the TURBOMOLE modular program suite for *ab initio* quantum-chemical and condensed-matter

simulations [128]. Ground-state and electronic absorption spectra calculations were performed with DFT and LR-TDDFT in the Casida formulation[34, 150]. All structures were built and visualized with Avogadro [151] and VESTA [152], and optimized using a 6-31G* basis set [153] and the B3LYP exchange-correlation functional [101, 154] with grid size m3 [155]. Solvation effects are included via the conductor-like screening model, COSMO, with standard settings for acetonitrile as a solvent. All LR-TDDFT calculations for the combined dye@TiO$_2$ systems are performed by freezing all occupied orbitals below the HOMO, thus allowing only excitations from the HOMO. In order to accurately represent the conduction band (CB) structure of titania, the same (TiO$_2$)$_{38}$ anatase cluster established in previous works was used [72, 99, 100]. Excited states are computed using the global hybrid functional B3LYP, the range-separated functional CAM-B3LYP [130], and the local hybrid functional Lh12ct-SsifPW92 [113, 156, 41].

In contrast to the constant exact-exchange admixture that is applied in global hybrid functionals, in local hybrid functionals the amount of exact exchange varies throughout the molecule. It is governed by a local mixing function $a(\mathbf{r})$ that depends on the density, the gradient or the kinetic energy density.

$$E_{\mathrm{XC}}^{\mathrm{LH}} = \int a(\mathbf{r})\epsilon_{\mathrm{X}}^{\mathrm{ex}}(\mathbf{r})d\mathbf{r} + \int (1 - a(\mathbf{r}))\rho(\mathbf{r})\epsilon_{\mathrm{X}}^{\mathrm{Slater}}(\mathbf{r})d\mathbf{r} + E_{\mathrm{C}}^{\mathrm{sifPW2}}. \qquad (26)$$

Lh12ct-SsifPW92, the local hybrid employed in this work, mixes Slater exchange with the exact-exchange energy-density, using a LMF based on the kinetic energy density, along with a one-electron self-interaction free version of the PW92 fit for LDA correlation. More details about the theoretical background of local hybrid functionals in comparison to global hybrids and range-separated functionals are given in the supplementary material and in Ref. [149].

To retrieve dynamical information about the photon-to-current conversion mechanism and efficiency, we simulate laser-induced electron injection with the hybrid TDDFT/configuration interaction method (TDDFT/CI) [117, 115, 116]. Here, the energies and coefficients of the excited states are obtained from a LR-TDDFT calculations that is performed once for every functional and dye@TiO$_2$ system. Note that, the full Casida matrix-equations were solved (without the Tamm-Dancoff approximation). Following previous work[157], the excited states are thus also referred to as energy levels in section 5.4. when the level alignments at the dye-semiconductor interface are discussed. Subsequently, the TURBO-MOLE data was post-processed for the electron dynamics calculations with ORBKIT [133, 134, 135]. An external electric field was applied vertically along the dye@TiO$_2$ direction as

$$\mathcal{F}(t) = F_0 \sin^2(\pi t/T) \sin\left(\omega_0(t - T/2)\right) \qquad (27)$$

The frequency, ω_0, is chosen for each system and functional in resonance with the transition from the ground state to the low-lying excited state with the largest oscillator strength. For every case the same laser pulse duration $T = 20\,\mathrm{fs}$ and amplitude of $F_0 = 15\,\mathrm{MW/cm}$ are used. The effect of the electric field on the

system is treated as a semi-classical interaction with the molecular dipole. Artificial reflections over the edges of the cluster are prevented using an absorbing potential. The latter simultaneously describes the coupling of the many-electron wave function with the semiconductor. Finally, non-adiabatic coupling between the electrons and nuclear vibrations is simulated by introducing Lindblad-type operators and using first-order time-dependent perturbation. Theoretical background of the electron dynamics and calculation of charge injections is detailed in the supporting information and in Ref. [149]. All dynamical calculations are performed using in-house codes [118, 158, 120, 126, 127].

6.4 Results

6.4.1 Static

The calculated transition energies of the lowest excited state in all free-standing dyes are reported in Table 5. For the first three dyes (WD-6, WD-7 and WD-8), they are compared to the experimental results obtained in previous work [146]. The excitation energies are presented for three different types of functionals (B3LYP, CAM-B3LYP and Lh12ct-SsifPW92). With a mean absolute error (MAE) of 0.08 eV, that is dominated by the dye with a thiophene linker (WD-7), the range-separated CAM-B3LYP functional performs best. Both, the global and the local hybrid functionals underestimate the transition energies, with the former lying much further away from the experimental values. It thus confirms that, with about 65% of Hartree-Fock exchange at long-range and only 19% at short range, CAM-B3LYP is able to capture the intramolecular charge transfer character of the free dye excitations accurately. The constant amount of exact exchange in B3LYP (20%) leads to a severe underestimation of the transition energies, which is likely to be seen in similar dyes such ME101-106. In all cases, the local hybrid functional yields results between the two other functionals. This is indicative that the local mixing function somewhat alleviates the problems of B3LYP and improves the description of intramolecular charge transfer states, albeit not perfectly.

Table 6 shows the first excitation energy for the same series of dyes adsorbed on the surface of TiO_2. The experimental transition energies for the three first dyes (WD-6, WD-7, WD-8) are found to be barely affected by the adsorption. This is also what is observed using the local hybrid functional, which adapts well to the electronic structure of the hybrid organic-semiconductor interface. On the contrary, CAM-B3LYP is severely overshooting the experimental findings in this case. As for the free dyes, B3LYP is severely underestimating all values, indicating the necessity of using a more flexible functional. With local hybrids, the maximum amount of exact exchange is located around the atom cores and in the asymptotic region. The LMF exhibits a shell structure, leading to lower exact-exchange admixtures on average for heavier elements. This seems to be sufficient to adapt to the different electronic environments, from the organic fragment to the semiconductor, while the imperfect treatment of intramolecular charge transfer is likely to remain present. Yet, local hybrids offer the best

dye	B3LYP	CAM-B3LYP	Lh12ct-SsifPW92	exp.
WD-6	2.30	3.30	2.70	3.22
WD-7	2.20	2.90	2.54	3.05
WD-8	2.29	2.93	2.61	2.94
MAE	0.81	0.08	0.45	
ME101	2.13	2.82	2.42	
ME102	2.18	2.76	2.45	
ME103	2.14	2.82	2.42	
ME104	2.01	2.79	2.34	
ME105	1.89	2.80	2.28	
ME106	1.76	2.68	2.09	

Table 5: Absorption maxima (in eV) from TDDFT calculations for the free dyes including solvent effects via COSMO. Results are showing the lowest dye → dye excited state. Experimental results are taken from Ref. [146].

balance and lowest MAE for the benchmarked systems, which we attribute in part to the reduced self-interaction error. For the other systems, although no experimental results are available, our CAM-B3LYP results confirm previous findings for the absorption maxima [147], e.g. that ME06 has the absorption maximum at the lowest energy and that the maxima for ME03 and ME04 are red-shifted compared to the other dyes. With the local hybrid the energy range of the absorption maxima is smaller. Yet, all functionals indicate that small changes in the donors group can significantly alter the energetic position of low-lying charge-transfer states, which will in turn affect the level alignement between dye-dye excitation and the semiconductor conduction band.

dye@TiO_2	B3LYP	CAM-B3LYP	Lh12ct-SsifPW92	exp.
WD-6	2.12	3.96	2.77	3.22
WD-7	2.08	3.44	2.52	2.97
WD-8	2.10	3.91	2.74	2.93
MAE	0.94	0.73	0.36	
ME101	2.14	3.10	2.42	
ME102	2.24	3.15	2.57	
ME103	2.63	3.88	3.00	
ME104	1.99	4.09	2.41	
ME105	1.80	3.28	2.33	
ME106	1.73	2.86	2.06	

Table 6: Absorption maxima (in eV) from LR-TDDFT in Casida form calculations for the dye@TiO_2 combined systems including solvent effects via COSMO. Results are showing the lowest dye → dye excited state.

The top panel of Fig. 12 shows the Gaussian-broadened absorption spectrum

from CAM-B3LYP calculations of three dyes with different linkers. As discussed above, CAM-B3LYP yields an excellent agreement with the experimental values, especially for WD-8, while the maxima for WD-6 is slightly blue- and the one for WD-7 is slightly red-shifted. All three dyes exhibit a similar second absorption band between 3.8–5.2 eV, which is composed of a multitude of excited states with relatively lower intensities. They can be seen in the top panel of Fig. 12.

The central panel of Fig. 12 highlights the strong blue-shift of the absorption maxima upon adsorption of the dye on the TiO_2 cluster with values ranging from 313 nm, 362 nm, and 317 nm. It is interesting that the experimental absorption spectra remain more or less the same upon absorption on TiO_2 films. Wan et al. [146] attribute that conduct to the starburst 2D structure of the dyes, which may prevented their aggregation on the TiO_2 film. As shown in previous work, this could stem from the wrong level-alignment at the CAM-B3LYP level of theory, where the first excitation is predominantly a HOMO-LUMO transition localized on the dye and within the semiconductor gap. This leads to almost no overlap of the dye-LUMO with TiO_2 and low hybridization with the semiconductor conduction band. Hence, excited electrons are only injected slowly in the semiconductor after photoexcitation, which will be demonstrated below.

The spectra also show a dramatic decrease in intensity for the WD-6@TiO_2 and WD-8@TiO_2 systems upon adsorption, revealing very low oscillator strengths with the range-separated CAM-B3LYP functional. Excluding the highest-intensity peak of the WD-7@TiO_2, the remaining excitations present similarly low oscillator strengths as in the two other systems. A potential cause for low oscillator strengths could come from the linkers, which is a crucial ingredient in the photovoltaic performance.Here, we provide evidence that it could originate from the spatial distribution of the charge densities on the donor groups. Per construction, it is composed only of the HOMO in our model. The charge density of the HOMO in the WD-6@TiO_2 and WD-8@TiO_2 systems is localized on a single donor. For the WD-7@TiO_2 system, the particle density is delocalized over the whole dye. This is illustrated in Fig. 13. All other examined systems (ME101-ME106) present a HOMO density on both donors as for WD-7@TiO_2 and, as a result, they have higher oscillator strengths even when considering only excitations from the HOMO.

The effect of excitations from lower-lying orbitals on the spectrum can be appreciated in the bottom panel of Fig. 12. By increasing the number of occupied orbitals in the LR-TDDFT calculations for the WD-6@TiO_2, the lowest-lying absorption band is red-shifted and the intensity varies importantly. When incorporating HOMO, HOMO-1, and HOMO-2 that are located on the other donor group or both, respectively (shown in Fig. 14), the intensity increases drastically and the transition energy decreases to 3.47 eV. This improves the agreement with experiment, although the error remains large (see Table 6). This demonstrates that the choice of orbitals for the excitations, the degree of delocalization of these orbitals, and the associated level alignment with respect to the semiconductor levels are of utmost importance to describe quantitatively electronic excitations at organic-semiconductor interfaces.

Lin et al. [147] reported the theoretical spectra for ME106 and ME106@TiO_2,

42
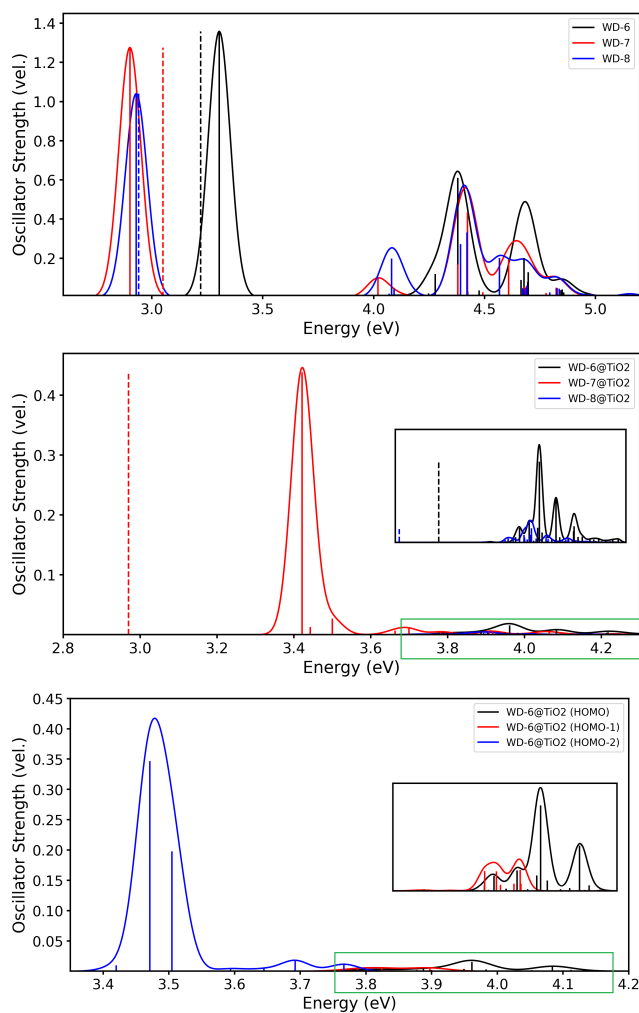
Figure 12: Absorption spectra for selected dyes of the WD series, calculated with the CAM-B3LYP functional and broadened with a Gaussian distribution. The top and central panels show the spectra for the isolated dyes and dyes@TiO$_2$, respectively, when allowing only for excitations from the HOMO. The bottom panel shows the spectrum for the WD-6@TiO$_2$ system obtained by allowing excitations from the one to three occupied orbitals (HOMO, HOMO-1, and HOMO-2). The insets show a zoom of the framed region of the associated spectrum. Dashed lines represent experimental reference values.

with the conclusion that the absorption spectrum of the adsorbed dye is consistent with the isolated dye. The spectra computed using the same range-separated functional are reported in Fig. 15. For the free ME106 in acetonitrile,
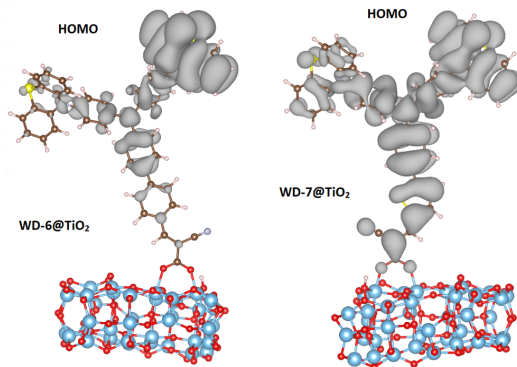
Figure 13: Isocontour of the HOMO density for WD-6@TiO$_2$ (left) and WD-7@TiO$_2$ (right). The isocontour value is chosen as $0.01\ a_0^{-3}$.

there are three significant absorption peaks at 462 nm, 302 nm, and 269 nm. Attaching the dye on the TiO$_2$ cluster notably reduces the oscillator strengths of all individual states, which was not observed previously. Further, only two major peaks at 432 nm and at 415 nm appear in the spectrum. The origin of this contrasting behaviour lies in the different approach to treat the interaction with the TiO$_2$ surface. Here, a three-layer (TiO$_2$)$_{38}$ cluster is used to represent the anatase surface, while a minimal model with a single TiO$_2$ unit was used in the previous study [147]. The latter is unable to reproduce the correct density of states in the semiconductor, thereby underestimating the degree of hybridization at the interface.

The level alignment at the dye-semiconductor interface can be assessed for the three functionals used in this work by projecting the many-electron states on the different fragments of the system [82]. It is shown in Fig. 16 for WD-7@TiO$_2$ and ME103@TiO$_2$. The level alignment behaves similarly for all other investigated systems and can be found in the Supporting Information. The particular behaviour shown here confirms previous findings for single-donor systems [149], where it was observed that a poor agreement of the first excitation energy for the free and anchored dyes can still lead to the correct level alignment. In the present case, global and local hybrids show similar accuracy, while the range-separated CAM-B3LYP yields a wrong level alignment: the HOMO of TiO$_2$ and of the dyes are much too low, and the LUMO of TiO$_2$ is close or even above the LUMO of the dyes. This could be explained by spurious exact interaction in the semiconductor introduced through the exact exchange at long range in this functional. A better description for the cluster could be obtained with screened hybrids that use exact exchange only at short range, thus highlighting a mismatch of the range-separation procedure for the description of dye-semiconductor interfaces. Interestingly, all three functionals place the LUMO of the dye at about the same energy. One reason why the local hybrids
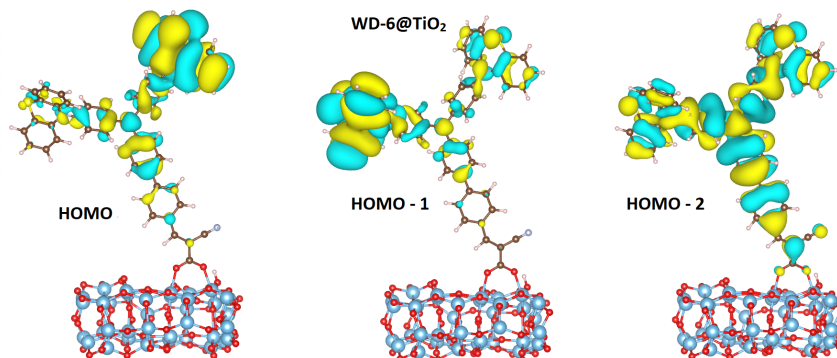
Figure 14: Isocontour of the HOMO, the HOMO-1 and HOMO-2 density for WD-6@TiO$_2$ with CAM-B3LYP. Positive isocontour is colored yellow, while negative is colored blue. The isocontour value is chosen as $0.01 \, a_0^{-3}$.
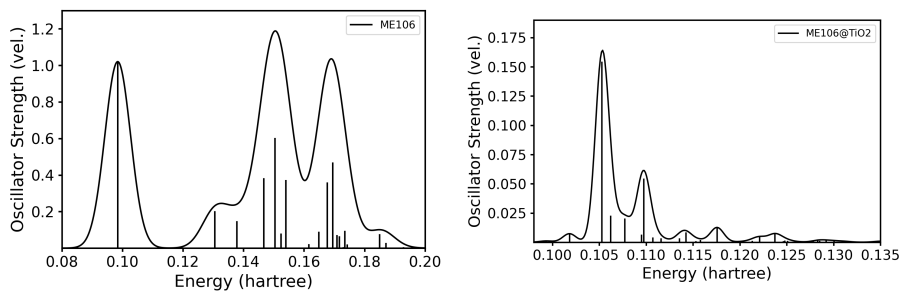
Figure 15: Absorption spectra for (top) the isolated ME106 dye and (bottom) the ME106@TiO$_2$, calculated with the CAM-B3LYP functional and broadened with a Gaussian distribution.

provide a more balanced description of the isolated dye and the combined dye-TiO$_2$ system is rooted in the local mixing function. It exhibits a pronounced shell structure leading to more oscillations for heavier atoms and an overall lower exact exchange admixture in the TiO$_2$ cluster than in the molecule. But, so far, local hybrid functionals have been developed and optimized for molecules and improved result for the combined system might be obtained by adjusting the LMF for solids or large clusters.

It is known that local hybrids are inferior to range-separated functionals for charge-transfer excitations and in order to describe the charge-transfer in the isolated molecule more accurately additional long-range exact is mandatory [111]. One route, that has been proposed recently is adding range-separation to a local hybrid functional [159]. Another option is a generalization of range-separated exchange functionals by replacing the constant range-separation parameter by a position-dependent function. This concept has been explored for basic chemical

properties showing its superiority over range-separated functionals with a fixed range-separation parameter, but an assessment for larger systems or excited states is still pending [160, 161].
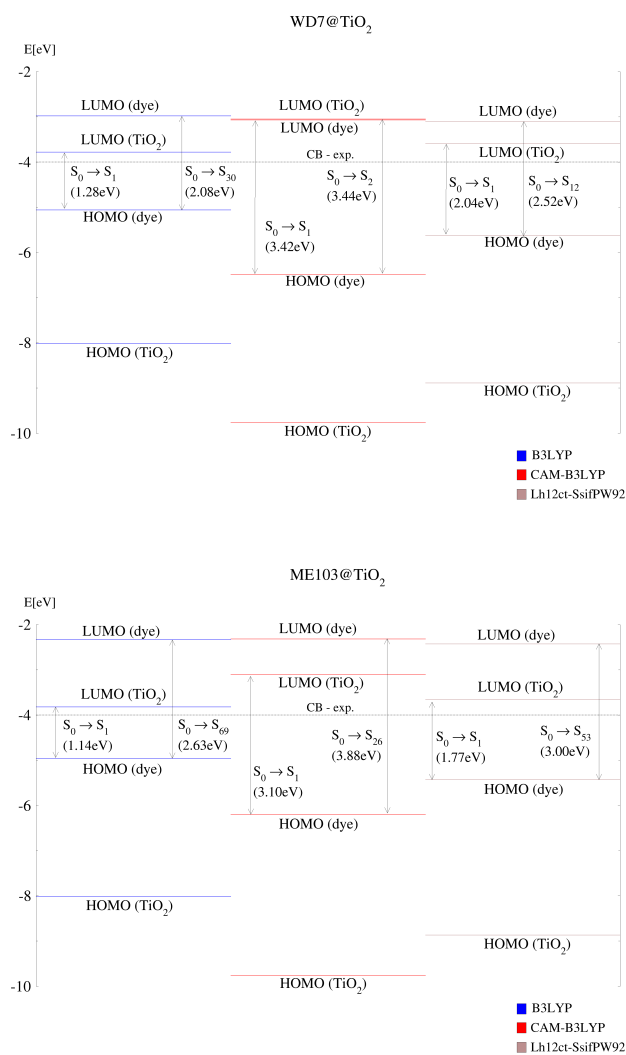
Figure 16: Alignment of the energy levels in (a) WD-7@TiO_2 and (b) ME103@TiO_2 in acetonitrile obtained from LR-TDDFT-COSMO calculations with three different functionals: B3LYP, CAM-B3LYP, and Lh12ct-SsifPW92. The black line is representing the experimental TiO_2 conduction band (CB) edge.

46
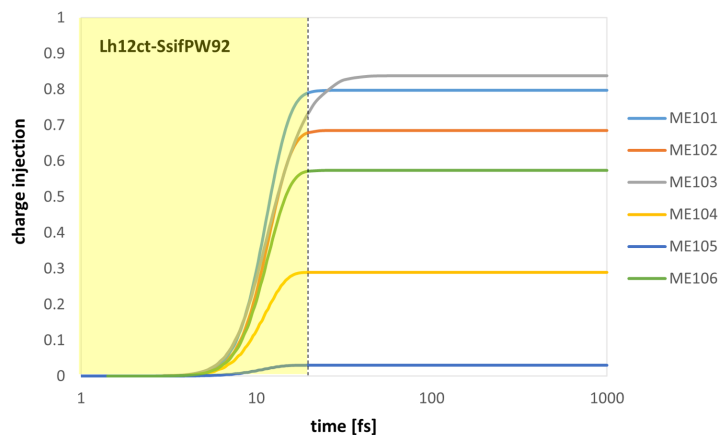
Figure 17: Charge injection efficiency for all investigated systems obtained from many-electron dynamics simulations using the local hybrid functional Lh12ct-SsifPW92.

6.4.2 Dynamics

The level alignment obtained with LR-TDDFT can potentially have a strong influence on the dynamical properties, not the least on the photon-to-current efficiency and the charge carrier injection rate. To shed light on these effects, many-electron dynamics simulations of charge injection induced by short laser pulses were performed. The employed parameters described in the Computational Details section are chosen to represent a realistic experimental setup, with a field amplitude of $F_0 = 15\,MV/cm$, which is polarized along the dye-cluster axis, and duration of 20 fs. Fig. 17 shows the charge injection efficiency for each system of the ME series, based on the LR-TDDFT reference with the local-hybrid functional. The yellow shaded area represents the time during which the pulses are applied. For completeness, similar graphs for the other functionals can be found in the Supporting Information. In all systems but one, charge injection is over by the end of the pulse. Yet, the injection mechanism in type II DSSCs is indirect, that is, electron loss to the conduction band of the semiconductor occurs after HOMO-LUMO excitation on the dye. This implies strong hybridization of the LUMO with TiO_2 orbitals and an important delocalization of the particle density over the whole cluster, which leads to an injection rate faster than the excitation dynamics.

The efficiency is satisfactorily high in most cases – in excess of 60% – except for the ME105 and ME104 dyes. The weak electron-donating effect of the methoxy group in ME105 seems to be screened by the phenyl linker, as the charge injection efficiency is much diminished as compared to the similar ME106 dye. This reduction in efficiency could also be caused by a steric effect because the latter dye is more compact than both ME0104 and ME105. The ME103@TiO_2 system containing the azo group and the electron-withdrawing

nitro group produces the highest charge injection. The second most efficient dye, ME101, is also elongated and spatially compact, which confirms that steric effect ought to play an important role in determining the charge injection efficiency in such double donor systems. Interestingly, ME103@TiO$_2$ is the only one in which some amount of charge injection is also taking place after the pulse is switched off. This implies that energy redistribution from the dye-LUMO to the conduction band through non-adiabatic coupling is slower in this system. In general, the charge injection efficiency computed using the local hybrid functional is much higher in every examined system in comparison to the global hybrid results. The range-separated functional predicts similar charge injection efficiencies (see Supporting Information), although it yields a wrong level alignment in the ME102@TiO$_2$ system.

The dynamical effect of the electronic structure stemming from different behaviour for the various functionals can be related to the population dynamics during laser excitation, which is shown in Fig. 18 for selected systems. Studying WD-7@TiO$_2$ using CAM-B3LYP (left panel), a large transition dipole moment is observed for WD-7 because of the stronger charge separation in the target excited state. This results in a faster population of the excited state than for the ME103@TiO$_2$ system (right panel), which shows a lesser degree of charge transfer character when studied using the local hybrid functional. The general effect is that a population remains trapped longer in the excited state in WD-7@TiO$_2$, with subsequent relaxation to the states of the semiconductor conduction band via non-adiabatic coupling. At longer times, all excited states lose their population via charge injection into the TiO$_2$ bulk, as quantified by the coupling through the complex absorbing potential.

Using CAM-B3LYP, the conduction band of WD-7@TiO$_2$ is shifted upwards and the first bright state does not strongly hybridize with the TiO$_2$ cluster. On the contrary, using Lh12ct-SsifPW92 for ME103@TiO$_2$ yields a better level alignement and leads to a stronger hybridization with the semiconductor. The faster charge injection in ME103@TiO$_2$ due to this stronger hybridization prevents accumulation of population in the bright state. This can be confirmed by looking at the projection of the NTO particle density on the dye for the low-lying excited states in both systems (see Fig. 19). Whereas the first excited state has its largest peaks for WD-7@TiO$_2$, the largest contribution of the LUMO on the dye for ME103@TiO$_2$ is buried deep in the conduction band of TiO$_2$. Despite a strong level of localization on the dye, the bright state rapidly decays to the large density of states delocalized over the TiO$_2$ cluster, which favor injection into the conduction band.

6.5 Conclusion and Outlook

We show that local hybrid functionals provide a balanced description of the excited states in isolated double-donor dyes and the dyes adsorbed on a sizeable TiO$_2$ cluster. Confirming previous findings, the range-separated functional CAM-B3LYP overestimates the band gap in the TiO$_2$ cluster, leading to wrong level alignments at the dye-TiO$_2$ interface and spurious blue shifts of the ab-
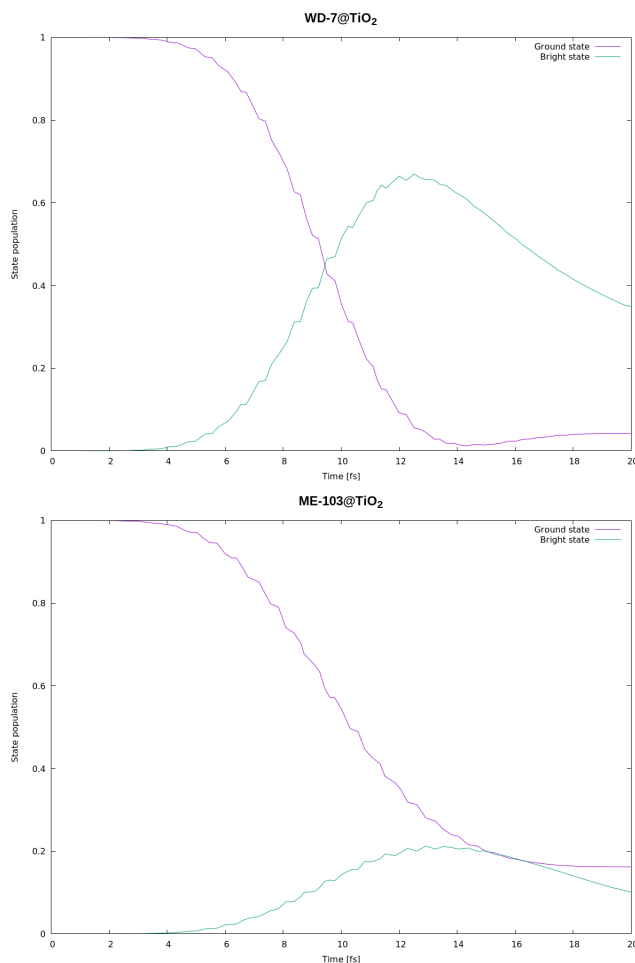
Figure 18: Population dynamics of selected states during the excitation of two dyes (a) WD-7 with CAM-B3LYP and (b) ME103 with Lh12ct-SsifPW92 on titanium dioxide using a sine-squared laser pulse of 20 fs and maximum amplitude of $F_0 = 15 MV/cm$. The lowest-lying $N_{states} = 30$ excited states up to an energy of 4.24 eV are used for (a) and $N_{states} = 70$ excited states up to an energy of 3.29 eV for (b). The frequency of the laser pulse is chosen resonant with the transition from the ground to the bright state, which amounts $\hbar\omega = 3.42\,\mathrm{eV}$ and $\hbar\omega = 3.00\,\mathrm{eV}$ for (a) and (b), respectively.

sorption maxima for dyes upon adsorption on TiO_2. For double donor dyes, excitations from other occupied orbitals close to the HOMO may need to be considered if the HOMO is mainly located on only one of the donor groups to increase the overall oscillator strengths and obtain meaningful absorption spectra. Starting from a LR-TDDFT calculation with local hybrid functionals, the

49
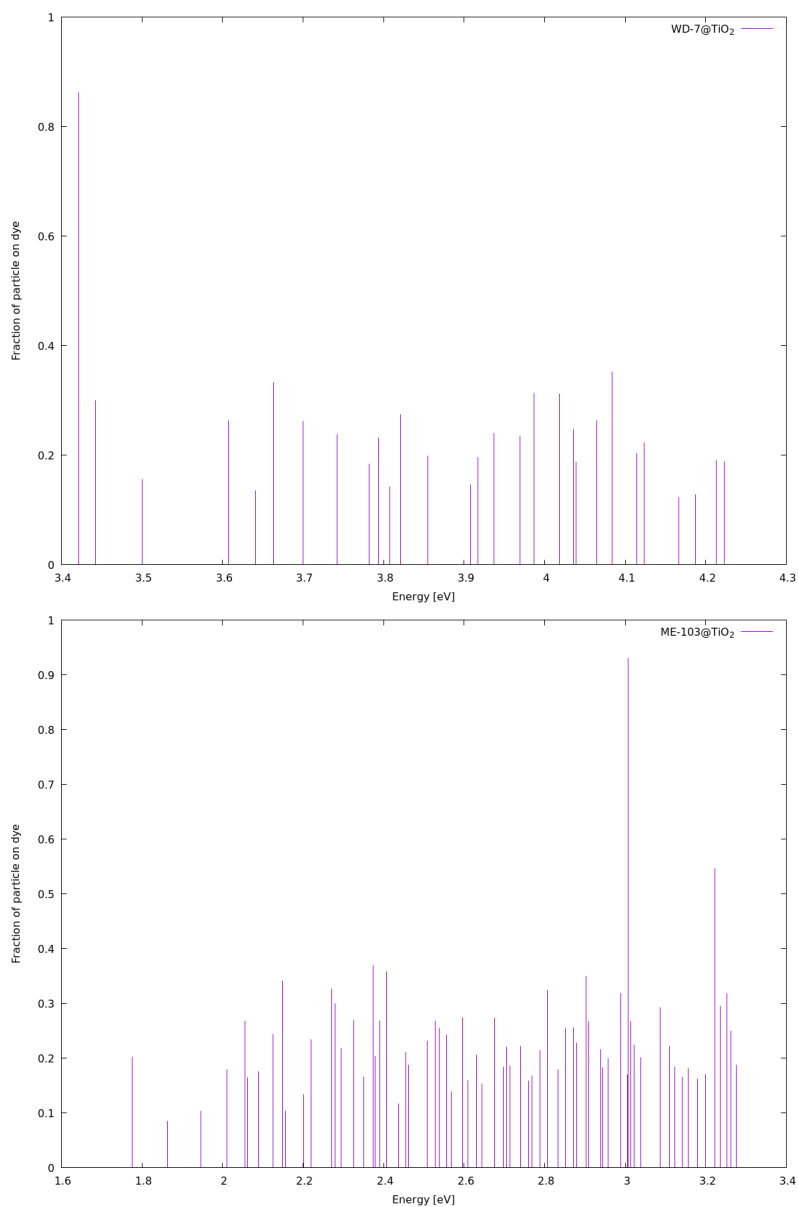
Figure 19: Projection of the NTO particle density on the dye. The lowest-lying excited states are reported for the (a) WD-7 with CAM-B3LYP and (b) ME103 with Lh12ct-SsifPW92.

laser-induced charge injection from the dye to the cluster is readily available. Based on comparison with experimental date for three dye-semiconductor sys-

tems, this approach may serve as a protocol for the prediction of charge-injection rates and efficiencies in cluster-based models for DSSCs. Among six dyes that have been proposed in an earlier DFT study, four dyes are found to be good candidates for improved DSSCs with charge injections between 60 and 80 %, while one dye with modified triphenylamino-donors appears to feature inefficient charge injections. Flexible hybrid functionals such as the local hybrids employed in this work are subject to on-going development. For instance, the recently introduced exchange functionals with local range-separation or range-separated local hybrids are likely to provide better quantitative agreement of excitation energies in DSSCs with experimental UV-Vis spectra and will be studied in the future.

6.6   Acknowledgements

6.7   Appendix B. Supplementary material

Supplementary data associated with this article can be found, in the online version, at https://doi.org/10.1016/bs.aiq.2023.03.009

7 Hydroxyapatites

Apatites represent a group of minerals with a similar structure and they can be found in various environments. Biological apatites are the main constituents of the hard tissue in the human body, from bones to teeth enamel. But also, they are a main part of some rocks and meteorites in the nature[162]. Investigation started around 1930, scientists performed the first X-ray pattern which showed apatites inside bone and tooth[163, 164]. In 1964 and 1980, we already knew everything about the crystal structure of the apatites, provided by the precise Reitveld analysis of the X-ray data[165, 166, 167].

It was discovered that the key component of bone tissues is a special family of apatite minerals, called hydroxyapatites (OHAp), which have calcium-phosphate phase form[168, 169, 170], with the chemical formula

$$Ca_{10}(PO_4)_6(OH)_2. \tag{28}$$

When we talk about bone tissue, OHAp has a hexagonal structure and non-stoichiometric form because a lot of substitutions can occur during the mineralisation process, providing a defective structure without strict ratios between the components. Opposite case is the monoclinic structure, which is thermodynamically more stable with the stoichiometric Ca:P ratio of 1.67, found as a mineral in earth crust[171, 172, 173, 174, 165, 175, 176, 177, 178].

Hydroxyapatites attracted attention because they can be used as a bioactive ceramic material in medicine as a promising material for bone reconstruction and implants in dental medicine. It is of great importance to investigate all of the possible defects and substitutions/vacancies that can occur in the hydroxyapatite structure in order to develop a suitable biomaterial for medical purposes. For now, OHAp is indeed the most used biomaterial. Knowing the surface properties of the material and its growth is the essential property, since it will be in contact with human cells[169, 170, 172]. In order to achieve that, we need to fully understand electronic structure of OHAp and DFT is proven to be a great tool for this kind of clarification.

Figure 20 is showing the differences between the two main structures of OHAp, hexagonal and monoclinic. The hexagonal structure has a $P6_3/m$ crystal space group with lattice parameters: $a = b = 9.417$ Å and $c = 6.875$Å, while monoclinic carry $P2_1/b$ group with $a = 9.48$Å, $b = 18.96$Å and $c = 6.83$Å parameters of a unit cell[179]. The unit cell for the hexagonal form consists of 44 atoms and monoclinic from 88 atoms, since the unit cell is doubled in one axis. There is a difference between the OH^- groups in the structures. Hexagonal OHAp has only one type of OH^- group, while in monoclinic there are two, hydroxyl (same as in hexagonal) and protonated hydroxyl group (HPO_4^{2-}), which can behave as a proton donor or acceptor. In different words, monoclinic structure can have both, parallel and antiparallel configuration of OH^- groups, while in hexagonal structure there is only an antiparallel arrangement. It is worth to mention how any defect in the structure will result in different unit cell composition.
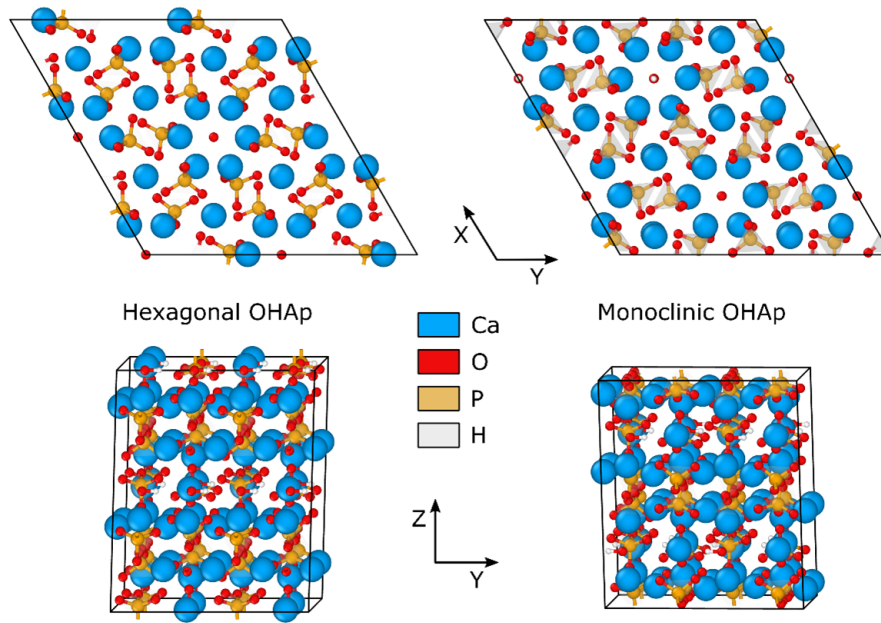
Figure 20: Crystallographic structure of hexagonal and monoclinic unit cell of hydroxyapatite.

When it comes to the substitutions and defects, a lot of things can happen. For example, instead of Ca atoms one can have Sr, Ba, Cd etc., P can be substituted with As, V, CO_3, Mn etc., and OH^- group can be replaced by $CO_3^{2-}, F^-, Cl^-, Br^-$ and many more[180]. Published work in the next chapters will be dealing with the three main types of substitutions, type-A, type-B and type-AB. It was discovered that the biological apatite contains carbonate ions in the range from 1.95 to 3.66% for human dental enamel[181, 182, 183, 184].

In the type-A substitution, carbonated ions take the place of the hydroxyl group inside the Eq. 28, while in type-B case they substitute some of the phosphate ions, including sodium (Na) atoms to maintain the charge balance. Type-AB is the mix of both substitutions at once, and this is the most common occurrence for the biological apatite inside a human body. Defects, vacancies and substitutions are very important for improving biomimetic characteristics of the hydroxyapatites and it also helps for preserving a hexagonal structure at room temperature[171].

Next chapters will provide the introduction to the IR and Raman spectroscopy and two already published papers about orientation effects in the Raman spectra of hydroxy-and carbonated apatite and surface phonons in the vibrational spectra, with much more detailed description about hydroxyapatites, methods and gathered results[185, 186].

8   Infrared and Raman Spectroscopy

In order to obtain significant information about the molecular structure and chemical properties of materials (samples), scientist use Infrared (IR) and Raman spectroscopy techniques[187, 188, 189]. Both are based on the interaction of electromagnetic radiation with the material, where we neglect the magnetic component of the field and focus only on the electric field, since the light-molecule interaction requires only electric dipole moments. Radiation is issued in discrete units or packets of energy, called photons, which have specific energies that can be absorbed by a material[190]. IR and Raman spectroscopy use different mechanisms and experimental setups for measuring the desired spectra, but they are complementary, filling each others "blanks", and only with both techniques we can get a full and complete spectra of vibrational modes inside of a molecule. In principle, a photon is absorbed and this changes the vibrational state of the system in both techniques, but the way in which the energy transfer occurs is different.

When a molecule absorbs light, it undergoes a fundamental transition, a leap from its ground state to the first excited state. This transition alters the total energy of the molecule, encompassing contributions from rotational, vibrational, and electronic energy components. From the IR and Raman point of view, the main interest is in vibrations and rotations, involving only the lower range of the electromagnetic spectrum. Figure 21 illustrates a potential energy diagram for the quantum mechanical harmonic oscillator. This model serves as a valuable tool for describing oscillatory behavior, particularly in the context of molecular vibrations. The harmonic oscillator assumes perfect periodic motion, which is a simplified representation suitable for many situations. However, it's important to note that real molecular vibrations often deviate from this idealized behavior due to factors such as anharmonicity. These deviations become particularly significant at higher energy levels. Additional terms in the Taylor expansion of the potential energy function provides a mathematical framework to describe these anharmonic effects, offering a more accurate representation of molecular vibrations under various conditions. The potential energy exhibits U-symmetric-shape around the equilibrium position, leading to discrete energy levels which are determined by their corresponding wavefunctions (Ψ). The square of the wavefunction provides the probability density of finding the oscillator at a specific position relative to the equilibrium. This analysis begins with the ground state, denoted by $n = 0$, with associated energy E_0 and wavefunction Ψ_0. In the quantum mechanical description of the harmonic oscillator, energy levels can be calculated using the following formulation

$$E_n = \left(n + \frac{1}{2}\right)hf \tag{29}$$

where n represents a discrete quantum number (0, 1, 2...), h is the famous Planck's constant and f is a classical vibrational frequency. In practice, deviations from the idealized quadratic potential curve are common in real-world
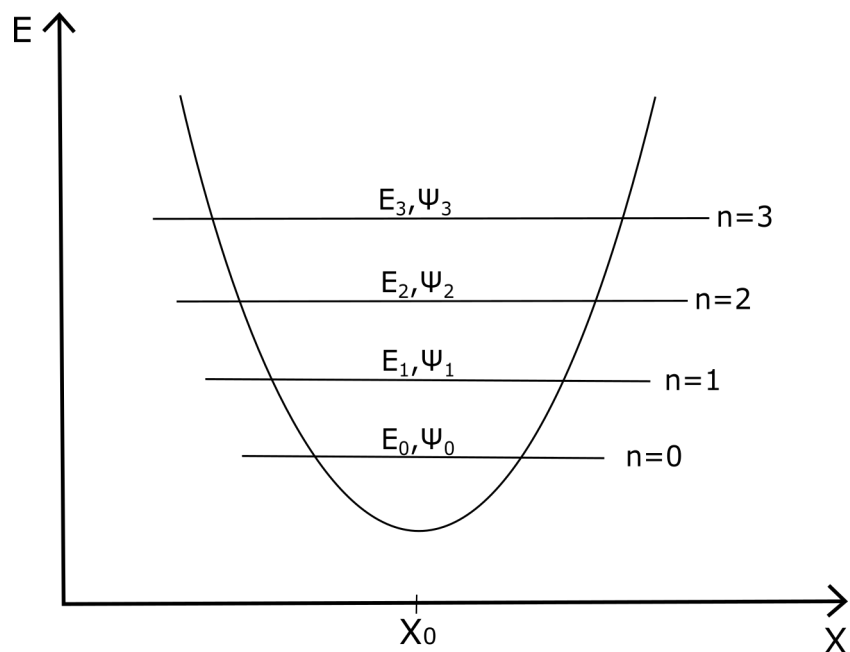
Figure 21: Potential energy diagram of a quantum mechanical harmonic oscillator with respect to the displacement. U-symmetric-shaped potential energy curve is represented with the corresponding energies (E) and quantum states (n). X_0 is the point of the equilibrium.

molecular systems. Anharmonicity refers to the departure of vibrational motion from the simple harmonic oscillator model, introducing higher-order terms in the potential energy function. To correct for these deviations and achieve more realistic results, it becomes crucial to account all vibrational states beyond the simple harmonic oscillator's ground state. In the harmonic oscillator model, the potential energy curve is parabolic, and the vibrational levels are evenly spaced. However, in an anharmonic system, the potential energy curve deviates from this idealized form, and the vibrational energy levels become unevenly spaced. By considering higher vibrational states and incorporating anharmonicity into the theoretical framework, the resulting spectra more accurately represent the complex vibrational behavior of molecules. This correction is particularly important when aiming to align theoretical predictions with experimental observations[191, 192, 193].

IR spectrometer can cover different ranges of frequencies like near-IR ($1400 - 4000 cm^{-1}$), mid-IR ($4000 - 400 cm^{-1}$) and far-IR ($400 - 10 cm^{-1}$). In the basic experiment, monochromatic light is directed onto the sample. At this point, the sample exhibits distinct vibrational levels characterized by molecular transitions. When illuminated, the sample selectively absorbs light at frequencies corresponding to the differences in energy between these vibrational levels. It

is essential to note that these transitions in molecules are not represented as continuous bands but rather as discrete energy levels. The absorption of light induces a frequency shift, which can be attributed to the distinctions between the sample's specific vibrational energy levels. The absorbed energy corresponds to the energy difference between the initial and final vibrational states of the molecules within the sample. This process results in a shift in frequency, providing valuable information about the molecular structure and composition of the sample. Our resulting IR spectrum will show peaks of specific vibrational bands and characteristic functional groups present in the analyzed sample. One of the most important role of the IR absorption process is the molecular dipole moment, μ. If our experiment is working and the frequency of the radiation corresponds to the frequency on which molecule is vibrating (resonance), the molecule will absorb energy and jump from the ground state to some specific excited state. For this to happen, the molecule must have a permanent dipole moment which is IR-active. This can also be seen on the spectra while the intensity of the peaks is directly correlated with the size of the dipole moment change. Total dipole moment can be expressed as the sum of these two components:

$$\mu = \mu_{elec} + \mu_{nuc}. \tag{30}$$

The electronic contribution operator (μ_{elec}) arises from the distribution of electronic charge in a molecule and is calculated as the sum of the product of each electronic charge (q_i) and its respective position vector ($\mathbf{r}_i$):

$$\mu_{elec} = \sum_{i=1}^{N} q_i \mathbf{r}_i. \tag{31}$$

On the other hand, the nuclear contribution (μ_{nuc}) accounts for the movement of atomic nuclei. It is expressed as the sum of the product of each nuclear charge (Q_i) and the vector representing the displacement of the nucleus from a reference position ($\mathbf{R}_i$):

$$\mu_{nuc} = \sum_{i=1}^{N} Q_i \mathbf{R}_i. \tag{32}$$

Simply put, IR is causing a dipole moment change with respect to the vibrational amplitude, A[190].

$$\left(\frac{\delta \mu}{\delta A} \right) \neq 0. \tag{33}$$

Molecules without a permanent dipole (eg CO_2) don't absorb light in the IR range. For these molecules there is no change in the dipole moment with respect to a normal mode. This IR inactivity can be covered if we use some other techniques such as Raman spectroscopy in order to get a complete picture of the molecular vibrations. That's why our intention is going from the dipole moment to the molecular polarizability, α, as a key component in the Raman spectroscopy. The polarizability is representing a value which is describing how much an external electric field changes the dipole moment. Raman spectroscopy
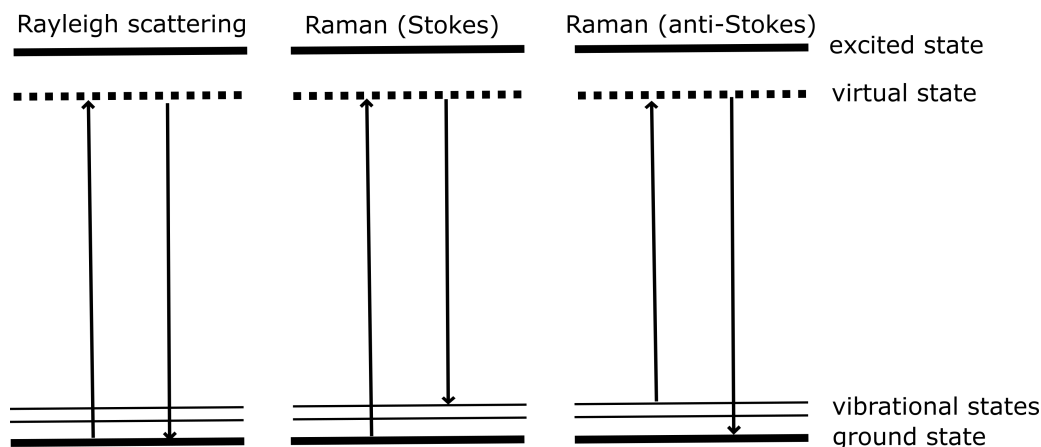
Figure 22: Schematic representation of Rayleigh, Raman (Stokes and anti-Stokes) scattering.

has a working principle based on light-scattering processes and interaction of incident light energy with the vibrational modes of a molecule. In principle, a photon will carry a greater energy than the vibrational energy and during the collision, the photon loses a fraction of its energy to the vibration, while the rest scatter with lower frequency. Raman spectra can catch a broad frequency region from $785cm^{-1}$ to $1064cm^{-1}$, which corresponds to UV, visible and near-IR region[194]. A transition is visible only if we have a change in the polarizability as a consequence of the electron interaction with an external electric field, E.

$$\mu = \alpha \mathbf{E}. \tag{34}$$

While this interaction influences the electron density, it also leads to changes in the molecular structure, inducing vibrational motion. The overall effect encompasses alterations in both electronic and nuclear distributions within the molecule, contributing to the observed transition and associated vibrations. In Rayleigh scattering, the majority of scattered photons are elastically scattered, meaning they retain the same energy (frequency) as the incident laser light. However, in Raman scattering, the interaction involves inelastic behavior. Photons are absorbed from the vibrational ground state of the molecule, temporarily elevating it to a virtual energy state. The molecule then returns to the same vibrational ground state, emitting a photon with the same frequency as the incident photon. This process results in what is known as Rayleigh scattering (no change in energy) (see Fig. 22).[195, 196, 197].

Central to the success of Raman spectroscopy is the concept of phonons, quanta of vibrational energy that illuminate the collective motion of atoms within a crystal lattice. Phonons are quantized vibrational modes, representing the discrete, quantized units of energy associated with the lattice vibrations of atoms. These modes include various patterns of atomic motion, such as stretch-

ing, compressing, and twisting to the collective dance of atoms within a crystal lattice. Phonons, therefore, act as messengers of molecular vibrations, conveying information about the structural and dynamic properties of a material. By analyzing the Raman shifts, researchers can decipher the unique vibrational fingerprint of a substance, unveiling details about its molecular composition, crystal structure, and chemical environment.

As we delve deeper into the intricacies of vibrational phenomena, our attention naturally turns to molecular vibrations, the fundamental oscillations of chemical bonds within molecules. While phonons describe describe the vibrational motion within a crystalline structure, molecular vibrations pertain to the internal movements of atoms within individual molecules. This shift in focus allows us to explore the finer details of a material's chemical composition and elucidate its molecular dynamics. To bridge these two realms, we turn our intention to the Raman tensor, a 3x3 matrix. This mathematical construct becomes a powerful tool, offering insights into the oscillations in polarizability concerning the modes of molecular vibrations. In the context of Raman spectroscopy, molecular vibrations refer to specific patterns of atomic motion within a molecule. These vibrational modes are quantized and can be excited by incident light, leading to characteristic changes in polarizability. Each mode corresponds to a specific way in which the atoms within a molecule move in relation to one another. Understanding these vibrational modes is crucial for interpreting Raman spectra, as they directly influence the Raman scattering process.

$$\begin{bmatrix} \alpha_{xx} & \alpha_{xy} & \alpha_{xz} \\ \alpha_{yx} & \alpha_{yy} & \alpha_{yz} \\ \alpha_{zx} & \alpha_{zy} & \alpha_{zz} \end{bmatrix} \begin{bmatrix} x_1 \\ y_1 \\ z_1 \end{bmatrix} = \begin{bmatrix} x_2 \\ y_2 \\ z_2 \end{bmatrix}. \tag{35}$$

Here, indicies on the left side of the equation represent the interaction of the Raman tensor components with the exciting radiation electric vectors (x_1, y_1, z_1), while on the right hand side we have vectors related to the Raman scattered radiation (x_2, y_2, z_2)[198]. Furthermore, Raman intensity ratios are calculated when we transform the Raman tensors through the directions in the coordinate system.

Density functional theory has a great potential in the field of spectroscopy, since there is a great progress involving new computational software methods together with significant compromise between computational costs and accuracy. DFT will provide molecular structures and in the harmonic approximation IR and Raman spectra, while it can analyze the polarizability changes which can be directly compared with experimental IR or Raman spectra. The next two chapters are presenting a DFT calculations of IR and Raman spectra on hydroxyapatites, showing its bulk and surface properties on the same foot.

9 Density funtional theory demonstrates orientation effects in the Raman spectra of hydroxy- and carbonated apatite

Work in this chapter has been published in

CRediT authorship contribution statement

Dejan Gemeri: Data curation, Writing - original draft preparation.

9.1 Abstract

Raman spectroscopy is widely used to examine the carbonate content within bone apatite, but Raman spectra are also sensitive to orientation effects between the polarisation of the incoming laser light and the sample orientation. This may lead to discrepancies when using Raman spectroscopy to evaluate the carbonate content as the extent of crystal organisation can change depending on the type of bone, age, and presence of mineralisation disorders in the organism. It is experimentally very challenging to evaluate the effect of orientation using individual bone crystals. Therefore, we have used density functional theory to examine the effect of orientation in apatitic materials. We examined hydroxyapatite and three different types of carbonated apatite: A-type where the carbonate ion substitutes the two OH groups in the unit cell, B-type where co-substitution occurs between carbonate in a phosphate position and Na^+ for Ca^{2+} to maintain charge balance, and AB-type where carbonate sits in both A-site and B-site. Our simulations show that the OH group in hydroxyapatite has a strong orientation dependence, consistent with previous literature. In addition, the phosphate and carbonate bands of the apatitic structures are predicted to be orientation dependent, where the maximum scattering efficiency occurs in configurations in which the laser polarisation is parallel to the crystallographic axes of the material. The intensity changes of the phosphate and carbonate bands are not consistent upon changing orientations and thus may lead to an underestimation of carbonate contents if insufficient sampling points are used during bone analysis.

9.2 Introduction

Biological apatite found in bone, dentine, and enamel[199] is an inorganic, crystalline calcium phosphate material with an atomic structure similar to that of abiotic hydroxyapatite (OHAp) found in geological materials. However, unlike its abiological counterpart, significant chemical substitutions are found associated with this material, particularly the occlusion of carbonate ions (CO_3^{2-}) either in place of a hydroxyl (A-type) or phosphate (B-type) group[12]. These substitutions dramatically change the physical and chemical properties of the crystals,[200, 201] enabling them to have specific functionalities in biological tissues. Due to this, significant amounts of research have been undertaken in the materials and medical science domains as changes in the chemical reactivity of the material can be related to pathological mineralisation, such as in cardiovascular disease, deficient mineralisation,[202] including osteoporosis,[203] and are important for the biocompatibility of bone and teeth implants[204]. Thus, it is of great importance to characterise and gain insight into defective OHAp structures. A key analytical tool for probing chemical changes in bioapatite, that is the go-to method for the materials and medical scientific communities, is vibrational spectroscopy: infrared (IR) and Raman spectroscopies. For example, pristine vibrational bands respond to the chemical environment of the carbonate group incorporated into the structure via the formation of new vibrational bands[205, 184, 206]. These methodologies are considered so robust that it has become a standard procedure to obtain the carbonate percentage in biological apatite from the ratio of the carbonate band(s) intensity versus the intensity of the dominant phosphate band. However, there have been reports that the relative intensities of the Raman bands are dependent on the orientation of the crystals with respect to the incoming light source,[207, 208] which can be highly variable in materials such as bone and dentine and change with age of the organism[209] or tissue and in the presence of mineralisation disorders[210].

Raman spectroscopy is increasingly the focus of such research as it has been suggested to be more sensitive to carbonate substitutions[211] and it is relatively easy to examine the effects of orientation using this technique. As a technique, it is particularly interesting for medical research because there is a potential to apply it in vivo,[212, 213, 214] unlike many orientation and compositional analytical techniques, for example, 2D X-ray tomography or electron microscopy. Hydroxyapatite and enamel have been measured using a Raman spectrometer under different laser polarisations at selected orientations, and results show that some band intensities have a strong dependence on the sample orientation[215, 216]. Similarly, bone samples orientated differently with respect to laser polarisation produce Raman spectra where the intensity of the biological apatite related bands varies[217]. Yet, the reported behaviour of the bands between these studies is inconsistent. Particularly, the effect on the symmetric stretching band of PO4 (ν_1) is critical because this is the band that is used to normalise intensities between spectra to calculate the carbonate concentration. In large, abiotic hydroxyapatite crystals the intensity of the ν_1 PO4 band is found to show minimal change with orientation,[216] yet within bone,

this effect is significant[210]. In contrast to bone and dentine biological apatite, enamel crystals are typically 100 times larger, have a lower carbonate content, and have higher crystallinity[218, 219, 220]. Whether carbonated apatite shows a similar orientational relationship to abiotic hydroxyapatite is unclear from the current studies. To the best of our knowledge, orientation experiments with synthetic carbonated hydroxyapatites have not been reported in the literature, probably due to the logistical difficulties associated with the small size of the crystallites produced. Similarly, mineral components in bone and dentine are too small to evaluate the effect of orientation on individual crystals. Therefore, in this study, we have used density functional theory to determine the effect of laser polarisation and sample orientation on the Raman spectra of carbonated apatites.

9.3   Methods

Density functional theory (DFT) calculations presented in this work were performed using a linear combination of atomic orbitals (LCAO) basis set as implemented in the all-electron code CRYSTAL (2017 release),[221, 222] where the atoms were described using basis sets reported in literature (calcium,[223] phosphorus,[224] oxygen,[225] hydrogen,[226] carbon,[227] and sodium[228]). The global hybrid B3LYP exchange-correlation functional[21, 154] was used throughout all calculations without further modifications. The geometry of each system under scrutiny was optimised in both atomic coordinates and cell parameters, while the Hessian was updated using the Broyden-Fletcher-Goldfarb-Shanno (BFGS) algorithm.

In CRYSTAL, the convergence of the real-space summation of the Coulomb and exchange contributions to the Hamiltonian matrix is controlled by five overlap criteria. The values used in this study were $10^{-6}, 10^{-6}, 10^{-6}, 10^{-6}$, and 10^{-12}. The threshold on the self-consistent (SCF) energy was set to 10^{-7} Ha. For the compounds of interest, the convergence with respect to k-points was checked. Monkhorst-Pack meshes of 2 x 2 x 4 for bulk hexagonal hydroxyapatite and 2 x 4 x 1 for bulk monoclinic hydroxyapatite were used to sample the first Brillouin zone[229].

Relative Raman intensities were computed analytically based on coupled-perturbed Hartree-Fock/ Kohn-Sham (CPHF/KS) treatments implemented in the code[230, 231]. Integrated Raman intensities are normalised so that the most intense peak is set to 1000. The peak width is not explicitly available within this treatment; thus, it was kept constant. The spectra are constructed by using the transverse optical modes and adopting a pseudo-Voigt function with the default VOIGT and DAMPFAC variables of 1.0 (pure Lorentzian functions) and 8.0 (full width at half maximum used for the spec- tra), respectively. The temperature and laser frequency, taken into account through a prefactor in the expression for the Raman integrated intensity, were set to 295 K and 532 nm to facilitate comparison with available experimental measurements. In CRYSTAL, the Raman spectra are obtained for an oriented single crystal and for a powder polycrystalline sample. Different polarisation components are identified

from the components of the polarisability tensor. The standard polarisation notation is used throughout the work; for example, the xy polarisation denotes the response of the material in the x-direction as a result of an applied incident light source polarised in the y-direction. Upon analysing the resulting spectra, the unit cell orientation axis were translated where required to a common reference system (chosen to be the initial pristine hexagonal bulk OHAp one, which corresponds closest to the crystallographic one) for consistent and relevant comparison between the systems under scrutiny. Furthermore, the chosen setup has been shown to reproduce the structure as well as vibrational properties of apatite compounds in good agreement with experimental data[232, 233, 234, 235]. Anharmonicity has been taken into account only for the O–H stretching mode[236, 237].

Long range dispersion corrections were included using the semi empirical D3 approach of Grimme et al. with Becke–Johnson damping[238, 239, 240]. Graphical drawings were produced using VESTA[152]. The crystal structures and their corresponding lattice directions used through- out this work are shown in Figure 23. Hexagonal OHAp was modelled in a unit cell with $P6_3$ (nr. 173) symmetry, instead of the experimentally noted $P6_3/m$ (nr. 176) space group to avoid the unphysical duplication of each OH group[225]; monoclinic OHAp was modelled in a cell with $P2_1/b$ symmetry (nr. 14), while all the carbonate-bearing models are simulated in a triclinic trivial P1 symmetry (nr. 1). Estimations of the intensities related to orientations other than the six calculated (xx, xy, xz, yy, yz, and zz) were found using a locally modified Matlab script (originating from the VASPKIT MAE script[241]) whereby the intensities were linearly interpolated before being plotted in a 3D diagram where notation of the plot axes corresponded to the crystallographic axes.

9.4 Results and Discussion

9.4.1 Geometrical features

The calculated lattice parameters of pristine as well as carbonated hydroxyapatite are listed in Table S1. The calculated values compare well to experimentally available data as well as earlier theoretical works, which is not sur- prising as the adopted methodology and simulated geometries have been audited and elaborated upon extensively in available literature[12, 225, 235, 242, 243, 244]. It is, however, noted that the inclusion of weak van der Waals (dispersive) forces (via the Grimme's D3 semiempirical approach) yields lattice constants that systematically underestimate the lattice parameters of OHAp when compared to experiments. Further system-dependent tuning of the dispersion parameters would be required to achieve results closer to measured ones, as demonstrated by Civalleri and co-workers,[245] which was not pursued here in order to present a systematic study with consistent parameters across all OHAp systems. The comparison of anharmonic corrections to the OH stretching modes is reported in Table S2. As CRYSTAL only applies anharmonic effects to stretching modes, it is difficult to make full comparison with experimental data for reasons outlined
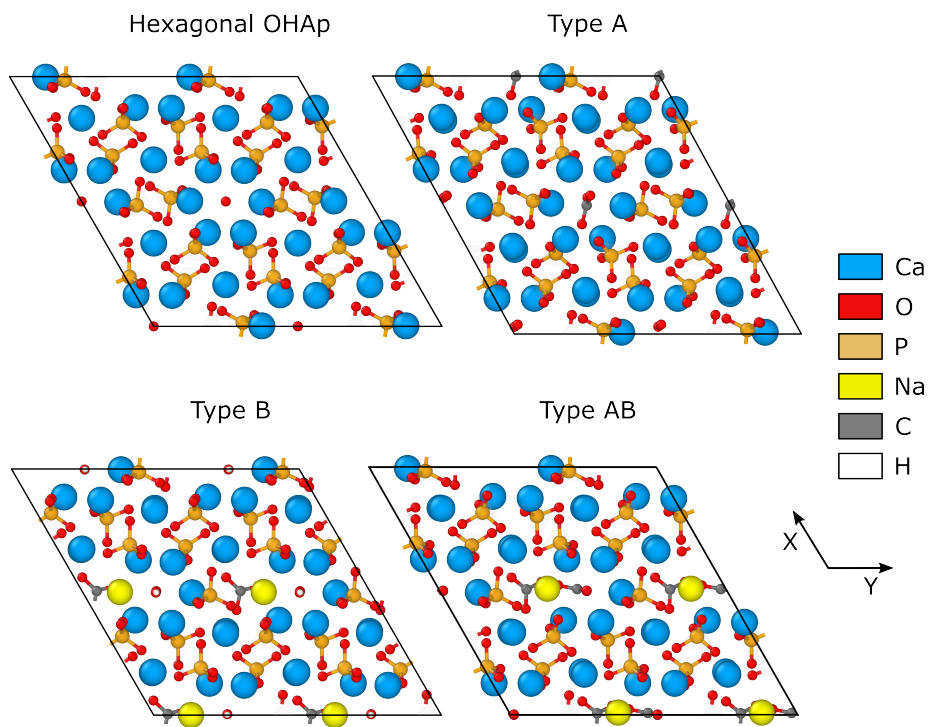
Figure 23: Crystal structure of the four distinct unit cells coupled with DFT used to determine the effect of laser polarisation and sample orientation on the Raman spectra of carbonated apatites

elsewhere[246].

9.4.2 Hydroxyapatite

Calculations of the effect of incoming light polarisation with respect to the crystal structure orientation calculated using DFT demonstrate that all bands in the Raman spectrum display an orientation dependency of their intensity (Figure 24a). Typically, the orientation of the incoming light perpendicular to the major crystal axes results in the lowest band intensities observed. The exception to this was the symmetric bending ν_2 PO_4 band at 474 cm^{-1}, which becomes more intense when the incoming light is orientated along the z-axis, but the crystal has an x or y orientation. Many bands important for the study of bone are even predicted to have close to zero intensity under the condition where the crystal and incoming light are orientated perpendicular to one another. For example, in the most extreme cases, such as the activity of the antisymmetric stretch of the phosphate band (ν_3 PO_4) at 1095 cm^{-1} and symmetric stretch of the OH band at 3790 cm^{-1}, the only orientation under which they are activated is when the crystal and incoming light are parallel along the z crystallographic axis (Figure 24b). This behaviour has been observed experimentally for the OH band, as described by Iqbal et al.[247] and Tsuda and Arends[216]. A loss of the OH band intensity upon rotation of the crystal from a parallel to 45° orientation of the laser was also found experimentally by Tsuda and Arends[216] and is confirmed by our calculations as shown in Figure 24b for this band. In Tsuda and Arends' work, the most sensitive bands to sample orientation were determined to be the antisymmetric bending ν_4 PO_4 bands around 590 cm^{-1}. In our model, the relative intensity of the 597 cm^{-1} band is largest in the zz orientation, whereas the intensities of neighbouring bands at 620 and 586 cm^{-1} become more dominant in other orientations. This is consistent with the observations in the literature; therefore, the DFT simulations reproduce the expected dependence of most Raman band intensities with respect to the laser orientation for hydroxyapatite crystals. However, previous experimental work has demonstrated that unlike other bands in the spectrum, the 960 cm^{-1} ν_1 PO_4 band does not exhibit the dramatic change in intensity found in the calculations[216, 247]. As hexagonal fluorapatite shows an orientation dependence of this band, the lack of an orientation dependence for hydroxyapatite was explained in previous studies as evidence for a monoclinic rather than hexagonal structure[247]. In contrast, our simulations with a monoclinic structure for hydroxyapatite show the same scale of orientational behaviour as that of the hexagonal structure (Figures S1 and S2), demonstrating that differences in the lattice are not sufficient to result in the observed retention of the ν_1 PO_4 band in the Raman spectra at different orientations in single crystal experiments. Interestingly, Raman spectra of bone materials obtained at different orientations with respect to the laser polarisation do show a dependence of the ν_1 PO_4 band intensity when scattering-related errors are minimised by using a high numerical aperture lens[210]. This behaviour is most consistent with the hexagonal crystal structure as the highest intensity is found when the laser polarisation is parallel to the long axis of the bone and
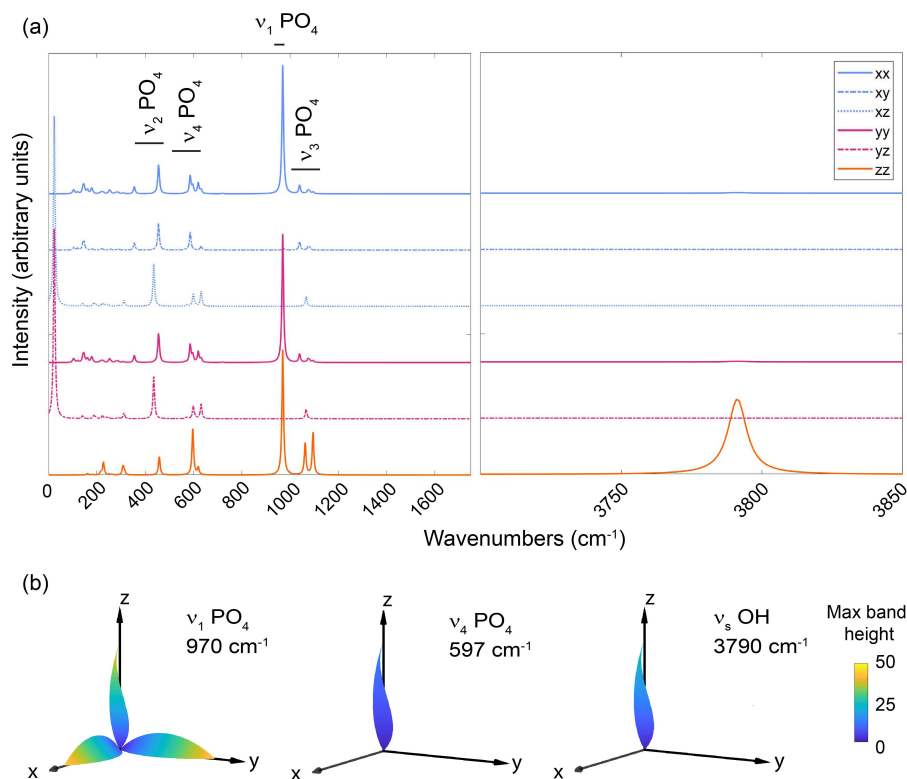
Figure 24: Analysis of the dependence of Raman band intensity on sample orientation of hydroxyapatite. (a) Raman spectra of hexagonal hydroxyapatite, where, for example, xy refers to response of the material in the x-direction as a result of an applied incident light source polarised in the y-direction. There are no bands between 1800 and 3700 cm^{-1}; therefore, this spectral range has been omitted to aid visualisation. Similarly, the spectra have been offset for clarity. (b) Three-dimensional plots showing the intensity of specific bands with respect to specific crystal-laser orientations. The intensities calculated have been linearly interpolated to predict band intensities when the laser is aligned in other orientations to those computed. Here, the axes refer to those of the crystal lattice. The colour scale reflects the highest intensity found in the spectrum, and the axes lengths are normalised to the maximum intensity of the band of interest to aid visualisation.

65

therefore the c-axis of the mineral. Therefore, we expect that the behaviour of this band found in the hexagonal model system is consistent with bone materials and is not related to a change in symmetry due to the presence of carbonate groups. We have thus continued to study the hexagonal form for the carbonated apatites rather than the monoclinic system based on this analysis.

9.4.3   A-type carbonated apatite

To maintain charge neutrality, all OH groups in the unit cell are replaced by carbonate in our A-type carbonated apatite model. Substitution of OH by carbonate was found to produce a change in the sensitivity of the phosphate bands with respect to the polarisation of the laser. In this material, there are several ν_1 PO_4 bands with similar intensities when summed over all orientations, where the most intense are found at 959 cm^{-1} and 965 cm^{-1} (Figure 25). Overlap of these bands produced a band envelope with an apparent higher wavenumber shoulder, also observed in published work on synthetic A-type carbonate apatites[184]. Animations of these bands using CrysPlot demonstrate that the band at 965 cm^{-1} corresponds to phosphate groups located close to the carbonate, in contrast to the 959 cm^{-1} band of phosphate groups in the centre of the unit cell. Overall, these bands have a similar behaviour to that observed for the ν_1 PO_4 band in hydroxyapatite, whereby an intensity close to zero was found for configurations when the laser polarisation was perpendicular to the crystallographic axes and the highest intensity in parallel configurations. But, their behaviour with respect to orientation is slightly different. For the 959 cm^{-1} band, there was a larger change in the intensities in parallel directions where the ratios of $I_{yy} : I_{xx}$ was 0.97 and 0.88 for $I_{zz} : I_{xx}$, in comparison with 1 and 0.97, respectively, in pure hydroxyapatite. In contrast, the 965 cm^{-1} band has a stronger orientation dependence producing ratios for $I_{yy} : I_{xx}$ of 0.94 and $I_{zz} : I_{xx}$ of 0.87, resulting in a higher prominence of this shoulder in spectrum from the xx configuration. The ν_4 phosphate band at 597 cm^{-1} showed only a weak direction–intensity relationship in this material.

In A-type carbonated apatite, the occupation of carbonate in the hexagonal channels within the apatite structure means that the carbonate group has a high degree of rotational freedom. Although it remains aligned with the channel length, which lies along the z-axis of the crystal, DFT calculations have demonstrated that there is a low energy barrier to rotation in the xy plane[248]. Thus, in experimental data, the carbonate signal should arise from an average of multiple orientations of carbonate within the channel. To evaluate how the orientation of the carbonate within the apatitic crystal structure changes the spectra under a differently polarised laser, we analysed three stable configurations where the three-fold rotational axis (C_3) of the carbonate group is differently orientated: (1) 5°, (2) 18°, and (3) 79° from the crystallographic x-axis (Figure 25c). In the Raman spectra, the most active carbonate band was that associated with the symmetric carbonate stretch ν_1. This band varied its position by 3 cm^{-1} depending on the orientation of carbonate group from 1129 cm^{-1} in configuration 3, to 1132 cm^{-1} when there was the largest mis-
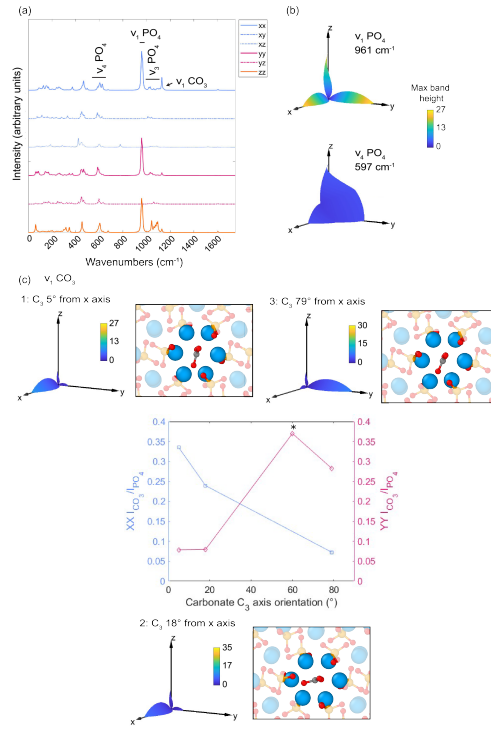
Figure 25: Analysis of the Raman band intensity dependence on sample orientation of A-type carbonate substituted apatite. (a) Raman spectra, where, for example, xy refers to response of the material in the x-direction as a result of an applied incident light source polarised in the y-direction. There are no bands above 1800 cm^{-1} as in this material, the CO_3^{2-} replaced OH^- in the structure. The spectra have been offset for clarity. (b) Three dimensional plots showing the intensity of phosphate bands with respect to specific crystal-laser orientations. (c) The effect of carbonate ion orientation in the xy plane on band activity. Intensity ratios of the carbonate versus the phosphate symmetrical stretch are plotted for the xx and yy configurations for models where the carbonate ion threefold rotational axis is orientated at 5°, 18°, and 79° to the x crystallographic axis. Due to the hexagonal unit cell, the C_3 axis is orientated along the y crystallographic axis at 60° in the plot. An estimate of the intensity ratio for the yy configuration at this point (highlighted with a *) was obtained by fitting the xx data with a polynomial function. Three-dimensional plots show the band intensities associated with the laser-crystal orientations for each model. Note, the plots in (a) and (b) correspond to configuration 1 in (c). For (b) and (c) 3D plots, the calculated intensities were linearly interpolated to predict band intensities when the laser is aligned in other orientations to those computed. The axis labels refer to the axes found in the crystal lattice, and the colour scale reflects the highest intensity found in the spectrum, with the axes' lengths normalised to the maximum intensity of the band of interest to aid visualisation.

67

alignment from the crystallographic axes (configuration 2). This corresponds with a slight deformation of the hexagonal Ca ring in the different configurations (Figure 25b) and is up to 20 cm^{-1} higher than described previously for synthesised samples[184]. In addition to a change in position, the carbonate ν_1 band intensity had a strong dependence on the laser orientation when it was closer to the crystallographic axes, but is expected to decrease as the C_3 axis becomes unaligned (Figure 25c). Although both the carbonate and phosphate bands vary their intensity with orientation differently, the ratios of carbonate to phosphate ν_1 bands calculated for the three carbonate orientation models produced a very similar range for the xx and yy configurations, 0.07 to 0.33 and 0.08 to 0.28, respectively. By examining the different orientations, it is predicted that the maximum intensity ratios will be 0.37 when the carbonate C_3 and laser polarisation are aligned with either the x or y crystallographic axes. In contrast, there was very little variation in the car- bonate to phosphate ratio (0.10 to 0.11) when the system was in the zz configuration, consistent with the lack of carbonate rotation with respect to this axis.

9.4.4 B-type carbonated apatite

Placement of the carbonate band in the location of a phosphate group (B-type substitution) with the concomitant substitution of a Ca^{2+} for a Na^+ to maintain charge balance results in a similar behaviour of the Raman bands to that of pristine hydroxyapatite. The lowest energy substitute configuration explored by Ulian et al.[235] was adopted for this study (labelled as the Na6 configuration model in the corresponding literature). Again, the dominant phosphate band, the symmetrical stretch ν_1 showed the highest intensity in parallel configuration along the xx-axis with $I_{yy} : I_{xx}$ and $I_{zz} : I_{xx}$ of 0.85 and 0.90, respectively. In comparison, the ν_4 PO_4 band at 597 cm^{-1} retained its dominance in the zz configuration but, as observed with the A-type carbonated apatite, also has a larger intensity contribution in the other two parallel configurations, as well as the perpendicular configurations (Figure 26). Examination of the vibrations contributing to this band using CrysPlot demonstrated that unlike the unsubstituted hydroxyapatite, in the B-type carbonated apatite, the band in the spectrum is not a pristine phosphate vibration but rather is overlapped by an additional OH stretch. Therefore, some of the orientational dependency may also arise from that of the OH group. As for the A-type carbonated apatite, the carbon- ate group shows a strong dependency on orientation. Here, the ν_1 of carbonate in the phosphate site is found at 1091 cm^{-1}, again consistent with previous analysis of synthesised B-type carbonated apatite[249]. But this band shows a high intensity along the zz direction with a very low intensity in the two other parallel configurations. This information if somewhat latent and mixed in the full spectra as a result of overlapping carbonate and phosphate bands, yet it can be clearly identified from the orientational plots for specific vibrational modes (Figure 26b). Thus, for a B-type apatite, the true carbonate content would only be able to be measured in the parallel configuration along the zz, with other parallel configurations resulting in an underestimation.
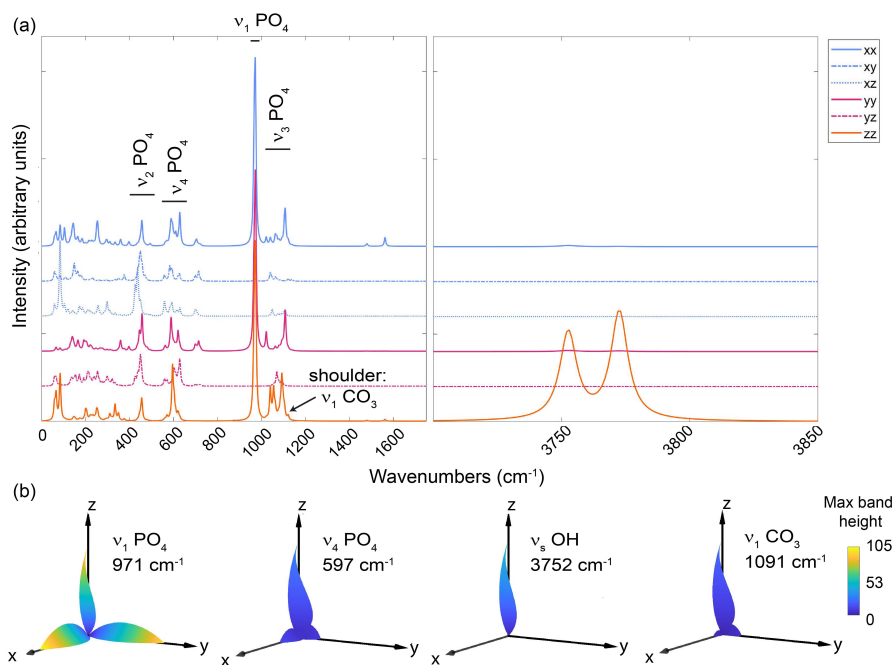
Figure 26: Raman spectra and intensities of specific bands with respect to the orientation between the laser and crystal structure for the B-substituted hydroxyapatite, where carbonate substitutes for a phosphate group within the apatite structure. (a) Raman spectra of different orientations between the incoming laser light and crystal structure. Here, for example, yz refers to the response of B-substituted hydroxyapatite orientated in the y-direction as a result of an applied incident light source polarised in the z-direction. There are no Raman bands determinable from the simulations between 1800 cm^{-1} and 3700 cm^{-1}; therefore, this spectral region has been omitted. The individual spectra have been offset to aid visualisation. (b) Plots showing the three-dimensional relationship between crystal orientation and laser polarisation. Intensities obtained from the simulations were linearly interpolated to predict band intensities when the laser is polarised in other orientations to those computed. Here, the axes refer to the axes in the crystal lattice. The axes' lengths are normalised to the maximum intensity of the band of interest whereas the colour scale reflects the highest intensity found in the spectrum.

9.4.5 Type AB

As expected, due to the mixed nature of the AB substituted apatite structure, this material shows a combination of the behaviours found thus far for the A and B-type apatite materials with respect to sample orientation and laser polarisation. As observed for the A-type carbonate substituted apatite, the phosphate ν_1 symmetrical stretch is split into two bands, where the lower wavenumber band (967 cm^{-1} in this model) has the highest intensity in all configurations and corresponds to phosphate groups located in the centre of the unit cell (Figure 27). In contrast, the lower intensity band observed for this material at 974 cm^{-1} corresponds to phosphate located closest to A-type carbonate group substituted the equivalent position to OH in hydroxyapatite. All bands show a sensitivity to orientation, with the phosphate ν_1 symmetrical stretching modes retaining their maximum scattering efficiency when the laser is polarised parallel to a crystallographic axis, with a maximum intensity found in the xx configuration. Similar to the B-type apatite, the phosphate ν_4 band at 597 cm^{-1} has its maximum scattering efficiency in the zz configuration, but, retains its orientation dependence unlike the A-type substituted apatite.

In contrast to the A-type apatite, our simulations with different initial orientations of the carbonate group in place of an OH group (A-type carbonate substitution) in the AB-type model reverted to the lowest energy state described previously by Ulian et al.[235] In other words, the rotational energy barrier for carbonate in the hexagonal channel that runs along the z-axis seems to be much higher in the AB-type carbonated apatite. This is likely due to the replacement of a Ca^{2+} ion at the edge of the channel with an Na^+ ion (Figure 23), required to maintain charge balance when a phosphate group is replaced by carbonate (B-type carbonate substitution). The carbonate C_3 axis in the AB-type structure is positioned 78° from the x-axis in the AB-type model, which is almost identical to configuration 3 in the A-type carbonated apatite model. However, the orientation sensitivity of the carbonate ν_1 band and its intensity were much lower as the xx and yy carbonate to phosphate ν_1 band ratios were 0.009 and 0.005 for the AB-type system, respectively, whereas they were 0.07 and 0.28 for the A-type model, respectively. A maximum scattering efficiency for the carbonate ν_1 band was found in the zz configuration for the AB-type carbonate substituted apatite, with $I_{xx:zz}$ and $I_{yy:zz}$ of 0.51 and 0.24, whereas the maximum difference in the perpendicular directions (in the xz configuration) is also 0.24 with respect to the zz scattering efficiency, with other directions producing an intensity even lower. The ν_1 symmetrical stretch of carbonate in the B-site of the AB substituted structure was found at the same location as the equivalent band in the B-type carbonate substituted apatite. However, the presence of the A-type carbonate appears to result in a change in the behaviour of the bands related to the carbonate substituted for phosphate. For example, the ν_1 symmetrical stretch of carbonate in the B-site found at 1091 cm^{-1} showed the same scattering efficiency in both the xx configuration and yy configuration as well as an intensity ratio for $I_{zz:xx}$ of 0.57, whereas in a perpendicular configuration, the highest intensity ratio was 0.10. Despite showing a similar behaviour
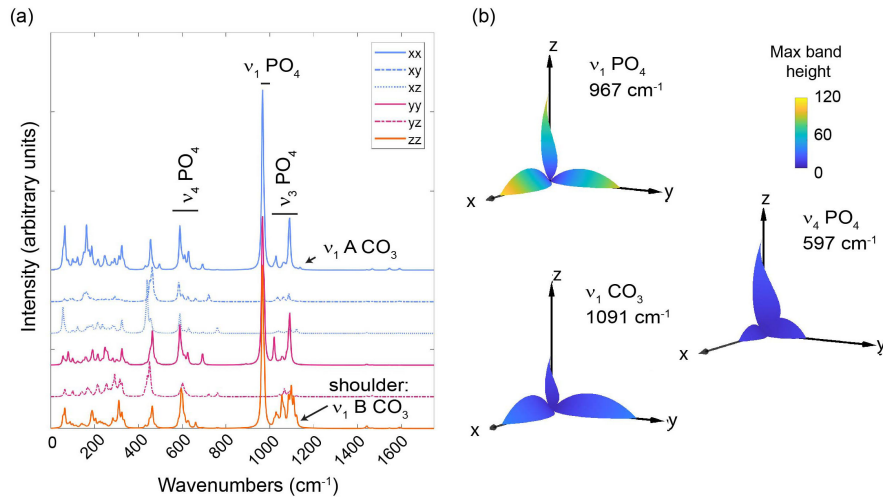
Figure 27: Raman spectra and intensities of specific bands with respect to the orientation between the laser and crystal structure for the B-substituted hydroxyapatite, where carbonate substitutes for a phosphate group within the apatite structure. (a) Raman spectra of different orientations between the incoming laser light and crystal structure. Here, for example, yz refers to the response of B-substituted hydroxyapatite orientated in the y-direction as a result of an applied incident light source polarised in the z-direction. There are no Raman bands determinable from the simulations between 1800 cm^{-1} and 3700 cm^{-1}; therefore, this spectral region has been omitted. The individual spectra have been offset to aid visualisation. (b) Plots showing the three-dimensional relationship between crystal orientation and laser polarisation. Intensities obtained from the simulations were linearly interpolated to predict band intensities when the laser is polarised in other orientations to those computed. Here, the axes refer to the axes in the crystal lattice. The axes' lengths are normalised to the maximum intensity of the band of interest whereas the colour scale reflects the highest intensity found in the spectrum.

71

with respect to the activity of bands in different configurations, the changes in scattering efficiency are not the same for the phosphate and carbonate related bands. In the parallel configurations, where the intensity is highest, the difference in scattering efficiency would result in a $CO_3 : PO_4$ ratio of 0.29, 0.35 and 0.18 for xx, yy, and zz, respectively.

9.5   Implications for Bone Analysis

Orientation of crystallites within bone is an important component of bone's mechanical function,[250] including during its regeneration[205]. It is known that the bioapatite crystals within bone can be orientated with respect to the collagen fibrils and thus the lamellae that are present at a higher level of the hierarchical arrangement in bone[251]. The absolute orientation of the bioapatite with respect to the bone characteristics will therefore be dependent on the type of bone, as compact bone in long bones has a different organisation at higher levels of the hierarchical material than spongy cancellous bone[252, 253]. Even in woven bone, where there is no measurable fibril orientation, bone mineral crystallites are observed to become orientated with time[254]. However, within a single compact bone, there can be different amounts of organisation, for example, two mineralised fibre arrangements are present, twisted, or orthogonal plywood structure, where differences in the relative intensities of Raman bands have been used to evaluate their presence[255]. Similarly, in rats, the level of organisation was not found to be consistent across a single bone specimen[256]. In addition, the organisation of the bone structure and therefore the alignment of the bone mineral component can vary with age,[209] up to puberty in humans,[257] and in cases where a bone mineralisation disease is present[258].

The observation that orientation would be expected to play a significant role in characterising bone materials is reflected in Raman spectroscopic analysis of these materials where the ν_1 PO_4 band intensity was found to depend on the orientation of the mineral with respect to the polarisation of the laser[210]. However, while it is an acceptable method to use Raman spectroscopy to evaluate the carbonate:phosphate ratios within bone,[259] the effect of orientation on this data is typically neglected in these analyses. The calculations conducted here clearly show that apatite phosphate band intensities are orientationally dependent. This not only applies to hydroxyapatite but also is consistent with our models of carbonated apatite, supporting the use of phosphate bands for Raman spectroscopy-based orientational studies as described in the literature. However, the carbonate bands are also highly orientation dependent and are not expected to scale directly with the intensity changes of the phosphate band based on the simulations. Even Raman instruments without the ability to polarise the laser along different directions can produce orientation effects in mineral spectra[260]. Therefore, this effect is expected to be present in mineral characteristic studies as well.

In compact bone, it has been reported that 75% of thecrystallites lie outside of the collagen matrix and that these crystals are highly aligned with their c-axis lying parallel to the long axis of the bone[261]. Evaluation of the effect of

orientation within the crystal on the measured ratios indicates a variability in the ratios of up to 23% for the B- and 17% AB-type carbonated apatite. Based on the calibrated lines of synthetic B-carbonated apatite,[262] this would be a variation in the carbonate content of 10 weight %. Given that the largest discrepancies for both the B and AB-type carbonated apatites are between the zz and xx or yy orientations, this implies that limiting the difference in orientation through analysing perpendicular to the long axis of the bone or collagen alignment should produce the most robust carbonate data, although they will reflect an underestimation in the carbonate content. When examining the difference between the xx and yy orientations, the difference in the carbonate:phosphate ratios are much lower, 6% for both B- and AB-type car- bonated apatite, resulting in a difference of 1 weight % carbonate when using the synthetic calibration lines. A previous study exploring longitudinally cross-sectioned compact bone found higher carbonate contents of several weight % related to less crystallite alignment in bone associated with a mineralisation disorder. In contrast, in the same study, a decrease in carbonate with increasing alignment was found related to age in normal mice[263]. This indicates that decreasing alignment of the crystallites does not scale directly with increasing carbonate content, which would be expected if an increased zz component was significant during the analysis of less organised bone. Thus, increased carbonate content related to bone mineralisation diseases was not the consequence of changes in the bone organisation. The variability of organisation within the bone structure requires that specific areas, such as close to osteons, should be avoided and many points taken to make a statistically robust measurement that can account for more variations. In addition, our findings suggest that there may be a population of the bone crystals in the randomly organised crystals that are not being effectively mapped by the Raman spectrometer during analysis if they are orientated perpendicular to the laser polarisation.

Interestingly, B-type carbonated apatites have been reported to have a lower OH band intensity with increasing carbonate substitution,[264] consistent with the observation of a lack of OH within the crystal structure in bone crystallites[220]. Our simulations demonstrate that for a structure that has 17% carbonate content, that is, one out of six phosphate sites it taken up by a carbonate ion, which is higher than the typical content reported for synthesised samples, the OH band should remain Raman active.

In the B-type carbonated apatite, the OH band becomes split due to the lowering of symmetry in the simulations from $P6_3$ in hydroxyapatite to P1. Yet, the OH/ν_1 PO_4 intensity ratio was very similar (0.61) for the most intense OH band of the B-type carbonate hydroxy- apatite compared with that found in the hydroxyapatite (0.60). Therefore, if OH was present in bone bioapatite and the sample was randomly orientate or along zz, the simulations indicate OH stretching bands should be visible in the Raman spectrum. Its absence in previous work[220] that studied an extracted powder that is assumed to be randomly orientated, thus, supports the hypothesis that bone bioapatite does not contain significant amounts of OH consistent with later NMR analyses[265].

A range of positions for the B-type carbonate ν_1 band have been reported

from 1072 to 1080 cm^{-1} depending on the phase composition, including the presence of other substitute ions such as silica, and crystallinity[266]. Most synthetic materials of the A- or B-carbonated apatite report ν_1 carbonate bands that are 30 cm^{-1} apart consistent with previous simulations of different AB-carbonate structures with the exception of one model where the ν_1 band positions of A-type carbonate were found to be lower than the equivalent B-type band[235]. A later paper has demonstrated that the exact spacing of these bands changed depending on pressure[267]. Therefore, there is a chance that there may be some overlap between A- and B-type ν_1 carbonate bands depending on the sample chemistry. Critically, even if the bands are distinguishable, our model demonstrates that the activity of the A-type band is expected to be lower in the AB-type carbonated apatite system. Thus, it is possible that in bone and synthesised carbonated apatite, some carbonate also substitutes for the OH but is not detectable using Raman spectroscopy. This would be consistent with IR spectroscopy analysis of bone, which detects carbonate in the A-type site[268].

9.6 Conclusion

Density functional theory calculations of hydroxyapatite and carbonated apatite structures have demonstrated a consistency with experimentally derived systems reported in the literature, including their response to orientation where this information is available. It became clear from the simulations that the apatite system has a strong orientation dependency of the Raman band intensities and that these behaviours differ depending on the band examined. This means that ratios of critical bands, such as the ν_1 of phosphate and carbonate, are not consistent between different orientations. In particular, the zz orientations have the highest sensitivity to both phosphate and carbonate and produce the largest ratio value. In comparison, there is almost no intensity observed for the phosphate and carbonate bands in orientations where the laser is aligned perpendicular to the crystallographic axes of the apatites studied. This means that for orientation studies, evaluations of bone cut perpendicular to the collagen structure will produce the most sensitive information. However, samples cut parallel to the collagen structure will be most effective for examining changes in carbonate content between specimens as the ratios of the carbonate and phosphate band intensities are most robust in this orientation because they are not as affected by orientation of the crystallites.

9.7 Acknowledgements

9.8   Appendix C. Supplementary material

Supplementary data associated with this article can be found, in the online version, at https://doi.org/10.1002/jrs.6465.

10 Identifying surface phonons in the vibrational spectra of carbonated apatite using density functional theory

Work in this chapter has been published in

CRediT authorship contribution statement

Dejan Gemeri: Data curation, Writing - original draft preparation.

10.1 Abstract

Vibrational spectroscopy is widely used to examine the mineralogy of bone apatite. Yet, these spectra may be significantly influenced by the nanometre size of the crystallites through either phonon confinement or surface phonon contributions. This could lead to misinterpretations of the implications of non-apatitic environments that have been described previously as additional bands in the vibrational spectra. Here we use density functional theory to simulate bulk and slabs of hydroxyapatite as well as A-type, B-type, and AB-type carbonated apatite to test for eventual contributions of surface phonons. The analysis showed that surface phonons can have a significant intensity in the vibrational spectra. They are expected at both higher and lower wavenumbers than their bulk counterparts, unlike phonon confinement which has been linked with only lower wavenumber shifts. The band shift of surface phonons was up to 40 cm^{-1}, which is determinable by both Raman and Infrared spectroscopy. All internal modes of evaluated molecular groups (OH, CO_3, PO_4) were affected by the surface presence. Therefore, it is expected that surface phonons are likely to be present in the vibrational spectra of bone minerals and contribute to spectral effects such as line broadening, presenting a crucial factor in their interpretation and application.

10.2 Introduction

Apatite is the inorganic component of biological hard tissues such as bone, dentin, and enamel[199, 12] and as such is a critical target in thin film research to enhance the biocompatibility of implants into these tissues [269, 270, 271]. Bioapatite found in hard tissues is a crystalline calcium phosphate material with an atomic structure similar to abiotic hydroxyapatite (OHAp, $Ca_{10}(PO_4)_6(OH)_2$).

However, unlike its abiological counterpart, significant chemical substitutions have been detected within the structure of bioapatite including the inclusion of carbonate ions (CO_3^{2-}) at different structural sites [268] and cations such as Mg^{2+} and Na^+ [272]. These substitutions dramatically alter the physical and chemical properties of the crystals and reflect the role of these materials within different hard tissues. Further changes in the crystal chemistry are also observed in situations where there is deficient mineralization[273, 274], including osteoporosis[203], which may have negative feedbacks for the functionality of the crystals within the biomaterial.

A key method used to probe chemical changes in bioapatite is vibrational spectroscopy: infrared (IR) and Raman spectroscopies. For example, carbonate is known to substitute into two different sites within the apatite structure, in place of an OH group (A-type substitution) or a phosphate group (B-type substitution), where charge balance is maintained during B-type substitution through the concomitant substitution of a divalent cation by a monovalent cation, i.e., Na+ for Ca^{2+}. As the pristine vibrational bands respond to the chemical environment of the carbonate group, new bands appear in the spectrum for A- and B-type substitution and carbonate adsorption[243, 184]. Analysis of IR spectra from bone also indicates that a third chemical environment for car- bonate is present, described as non-apatitic carbonate[268], which has led some authors to suggest that bone minerals are in fact sheathed with a less crystalline, highly labile layer [275]. A recent study has predicted that for a 4 nm thick particle this layer could be as wide as 0.8 nm [276]. Although the presence of a non-apatitic carbonate environment has been considered to occupy a layer at the crystal exterior simply the presence of a surface gives rise to strain within the crystal structure reducing crystallinity in the surface region. As bone crystals have been reported to have a platelet morphology of around 20 nm width and 6 nm thickness[277], there will be a high surface to bulk ratio, making the effect of the surface region's difference in crystallinity measurable. Indeed, the additional strain in this region is thought to be responsible for line broadening effects in X-ray diffraction measurements[278].

Two effects may occur in the vibrational spectra due to the presence of nano-sized crystalline material. The first is phonon confinement, whereby new vibrational modes become detectable when a material is typically smaller than 10 nm[279]. The second is the presence of surface related phonons. Here reconstructions of the atomic arrangement to accommodate the surface bond terminations will break site symmetry also resulting in the potential formation of new vibrational bands or shifts in the modes due to changes in nearest neighbour distances, thus bond lengths. Band broadening observations from bone vibrational spectra have been attributed to phonon confinement[277, 280], but, the platelet like shape of bone crystallites[278] would limit this effect [281] and it cannot explain the presence of the additional carbonate environment observed in IR and nuclear magnetic resonance data. In contrast, the presence of surface phonons are typically not considered. Direct correlation of surface phonons with specific structural sites is not possible from experimental data. Therefore, we use density functional theory calculations to test the hypothesis whether surface

phonons are visible in the vibrational spectra of nanosized apatite. To do this we have examined hydroxyapatite slabs of different thicknesses as well as A-, B- and AB-type carbonate substitution to evaluate whether different carbonate groups are sensitive to structural reconstruction at surfaces.

10.3 Computational details

Theoretical results presented in this work are based on density functional theory (DFT) calculations performed using a linear combination of atomic orbitals (LCAO) basis set as implemented in the all- electron code CRYSTAL (2017 release) [221, 222] and the B3LYP hybrid exchange functional [21, 154]. This functional has been shown to provide a reliable description of geometry, electronic structure, energetics, and phonons in a wide range of materials [282, 283, 284, 285, 286, 287]. With respect to the basis set, atoms were described using basis sets reported in literature (calcium [223], phosphorus [224], oxygen [225], hydrogen [226], carbon [227], and sodium [228]).

In CRYSTAL, the convergence of the real-space summation of the Coulomb and exchange contributions to the Hamiltonian matrix is controlled by five overlap criteria. The values used in this study were 10^{-6}, 10^{-6}, 10^{-6}, 10^{-6}, and 10^{-12}, ensuring convergence of the vibrational frequencies up to 1 cm^{-1}. The threshold of the self-consistent (SCF) energy was set to 10^{-7} Ha for single-point and relaxation calculations, while it was set to 10^{-10} for frequency calculations. For the compounds of interest, the convergence with respect to k-points was checked. Monkhorst-Pack meshes of $2 \times 2 \times 4$ for bulk hexagonal hydroxyapatite and $2 \times 1 \times 4$ for bulk monoclinic hydroxyapatite were used to sample the first Brillouin zone[221].

Relative Infra-red and Raman intensities were computed analytically where possible, based on coupled-perturbed Hartree-Fock/Kohn-Sham (CPHF/KS) treatments implemented in the code[288, 229, 231, 230]. Integrated Raman intensities are normalized so that the value for a selected reference mode is set to 1000. The spectra are constructed by using the transverse optical modes and adopting a pseudo-Voigt function with the default VOIGT and DAMPFAC variables of 1.0 (pure Lorentzian functions) and 8.0 (full width at half maximum used for the spectra), respectively. The temperature and laser frequency, only taken into account through a prefactor in the expression for the Raman integrated intensity, were set to 295 K and 532 nm, for relevant comparison with experimental measurements. In CRYSTAL, the Raman spectra are obtained for a powder polycrystalline sample. The chosen setup has been shown to reproduce the structure as well as vibrational properties of apatite compounds in good agreement with experimental data[234, 235, 232, 233]. However, for two systems in the given study, namely i) the bulk AB-type carbonated apatite simulated in the $2\times2\times1$ supercell and ii) the (100) AB-type surface cleaved from the $2\times2\times1$ bulk supercell, the system size prohibited us from using the CPHF/KS approach when computing vibrational frequencies, so we instead resorted to the use of the Berry phase approach to obtain relevant information about the infrared spectra[236, 289]. The differences between the two approaches for com-

puting the vibrational frequencies were assessed and found not to exceed 1 cm^{-1}. Anharmonicity has been taken into account only for the OH stretching mode[236, 237]. Graphical drawings were produced using Ovito[290].

Hexagonal OHAp was modelled in a unit cell with P63 (nr. 173) symmetry, instead of the experimentally noted $P6_3/m$ (nr. 176) space group to avoid the unphysical duplication of each OH group[225]; monoclinic OHAp was modelled in a cell with P21/b symmetry (nr. 14), while all the surfaces and defect-bearing models are simulated in a triclinic trivial P1 symmetry (nr. 1). Crystallographic parameters of the surfaces can be found in Table S1.

The surfaces were modelled as two-dimensional slabs periodic in the x- and y-direction, but not in the z-direction. This means that there is no parameter for the vacuum thickness needed. To characterize the surface, the surface energy (γ) as a measure of the thermodynamic stability has been calculated through the following expression:

$$\gamma = \frac{E(n) - nE_{bulk}}{2A} \tag{36}$$

where E(n) is the energy of the slab containing n-layers, Ebulk the energy of the bulk, and A the area of one side of the slab. Low Miller index surfaces were created from each relaxed bulk structure and further filtered based on the following criteria: stoichiometry, coordination environment, and polarity. Surfaces obtained by cleaving the phosphorus tetrahedral and/or carbon trigonal geometrical environment were neglected as this represent chemically unfavourable configurations and therefore very unlikely to be found in real systems. Furthermore, out of the initially screened geometries, those which have the lowest total dipole moment perpendicular to the surface (Tasker I and Tasker II type surfaces in his seminal work[291]) were chosen. Slabs structures with large dipole moments undergo complex reconstruction to cancel the inherent dipole present at the unreconstructed surfaces. Stabilization methods include metallization (charge transfer across the slab), vacancy formation, adatoms, etc., however, such reconstructed dipolar surfaces are usually less stable and due to the additional complexity have therefore been neglected in this study. After applying the aforementioned criteria, a handful of surfaces were identified as suitable, which are summarized in Table 7. Our previous work demonstrated that the hexagonal form of hydroxyapatite replicates the orientation dependent spectral behaviour of hydroxyapatite best[185], thus we focused on this system in this work. However, the lowest energy surface for the monoclinic system has been included in Table 7 for completion.

The radial particle distribution function (PDF) measures the probability of finding a particle at distance r given that there is a particle present at position r = 0, yielding a histogram of pair-wise particle distances. The PDFs have been obtained with OVITO using the DFT relaxed structures. The separation distance for the histogram bins was set to 0.02Å.

System	Surface termination	$\Gamma(J/m^2)$	Surface dipole (D)	Surface thickness (nm)
Hexagonal HAP	(010):Ca-O	1.19	0.91	2.38
Hexagonal HAP	(001):Ca-O	1.01	0.04	2.00
Monoclinic HAP	(010):Ca-O	0.97	0.00	2.10
Type A	(100):Ca-O	0.75	0.88	2.08
Type B	(100):O-H	0.98	2.43	2.45
Type AB (from 1x1x1 bulk)	(001):Ca-O	0.85	3.44	2.00
Type AB (from 2x2x1 bulk)	(100):Ca-O	1.14	0.96	3.21

Table 7: Identified suitable surfaces of hydroxyapatite together with their termination indicator, calculated relaxed surface energies (Γ), final surface dipole moment, and slab thickness, respectively. For type AB hydroxyapatite, two different slabs were considered, one cleaved from a pure hydroxyapatite bulk doped in the 1×1×1 simulation cell and one from a pure hydroxyapatite bulk doped in the 2×2×1 simulation cell.

10.4   Results and discussion

10.4.1   Hexagonal hydroxyapatite

Pristine bulk   Our presented results on pure bulk hydroxyapatite are found consistent with earlier experimental and theoretical works [225, 292], but to aid comparison with the data derived from the modelled slab structures we have described it together with its related vibrational spectroscopy signatures briefly here. Hexagonal hydroxyapatite is characterized by tetrahedrally coordinated phosphate groups that interconnect Ca^{2+} ions sitting in two distinct sites, one coordinated to 9 different O atoms of the phosphate groups and a second coordinated to 7 different O atoms of which one is part of the OH group. From the calculations, these sites have a distance between the Ca-O of 2.5 and 2.4Å, respectively (Fig. 28). The 7-fold coordinated Ca^{2+} ions are organized in a hexagonal ring structure that is described in the third dimension by a screw axis along the c direction. In the centre of the ring, the OH groups point downwards along the c-axis. Focusing on the vibrational spectral region above 400 cm^{-1}, where internal modes related to specific molecular units are found, the simulations of bulk hydroxyapatite produced multiple bands between 550 and 650 cm^{-1}, 950–1150 cm^{-1} and above 3600 cm^{-1} (Fig. 29).
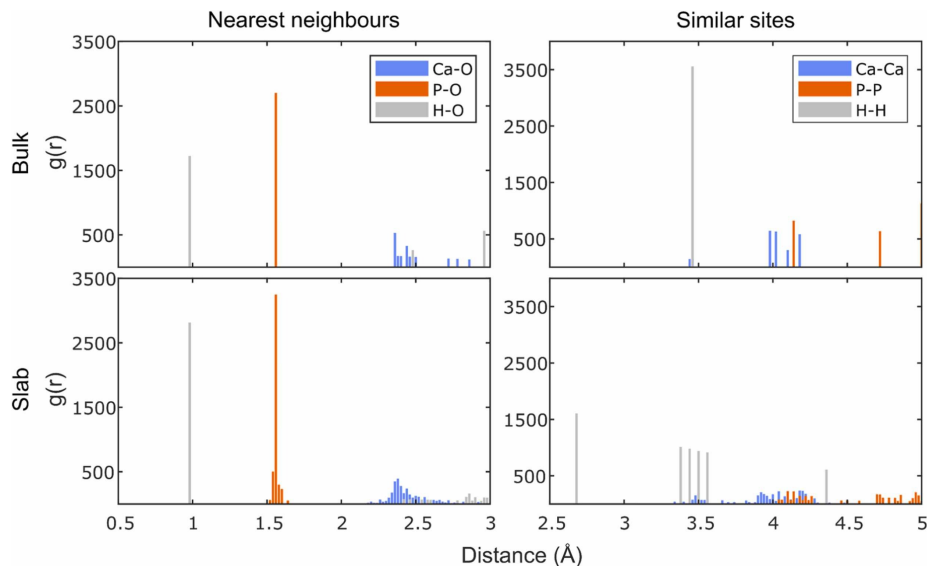
Figure 28: Pair distribution functions for the nearest neighbours and longer-range distances between similar sites for hexagonal hydroxyapatite bulk and slab with a thickness of 2.38 nm.

Most bands in the spectral region between 550 and 650 cm^{-1} arose from a mixture of OH group bends (δ) and a phosphate bend (ν_4) in the IR and Raman spectrum. The exception to this are the bands at 565 and 620 cm^{-1} in the Raman spectrum, which was found to be a pure phosphate ν_4 stretch. The 565 cm^{-1} band corresponds well with experimental observations[293]. However, the 620 cm^{-1} is very weak but has been detected in IR spectroscopy of experimentally synthesised hydroxyapatites[294]. In the IR spectrum a phosphate symmetric stretching mode (ν_1) was found, albeit with low intensity, at 971 cm^{-1} as well as a dominant and degenerate phosphate asymmetric stretching modes (ν_3) at 1044 cm^{-1} and slightly weaker third ν_3 phosphate mode at 1053 cm^{-1}. A final degenerate ν_3 mode was found at 1109 cm^{-1}. Of the ν_1 modes, only the band at 971 cm^{-1} was found in the Raman spectrum, where it was now the most intense band for the internal modes. In contrast, multiple ν_3 modes were observed from 1040 cm^{-1} to 1100 cm^{-1} spectral range, of which some had a small component of an OH bending mode. In the Raman spectrum, the symmetric stretch (ν_1) of the OH group was also visible at 3598 cm^{-1} after correction for anhar- monicity effects (Table 8). These results on anharmonicity are consistent with earlier experimental and theoretical work, describing such effects in greater detail[246].

Pristine surfaces   Cleaving the bulk structure along the (010) plane (which is equivalent to the (100) plane as a result of the crystal symmetry of the bulk)
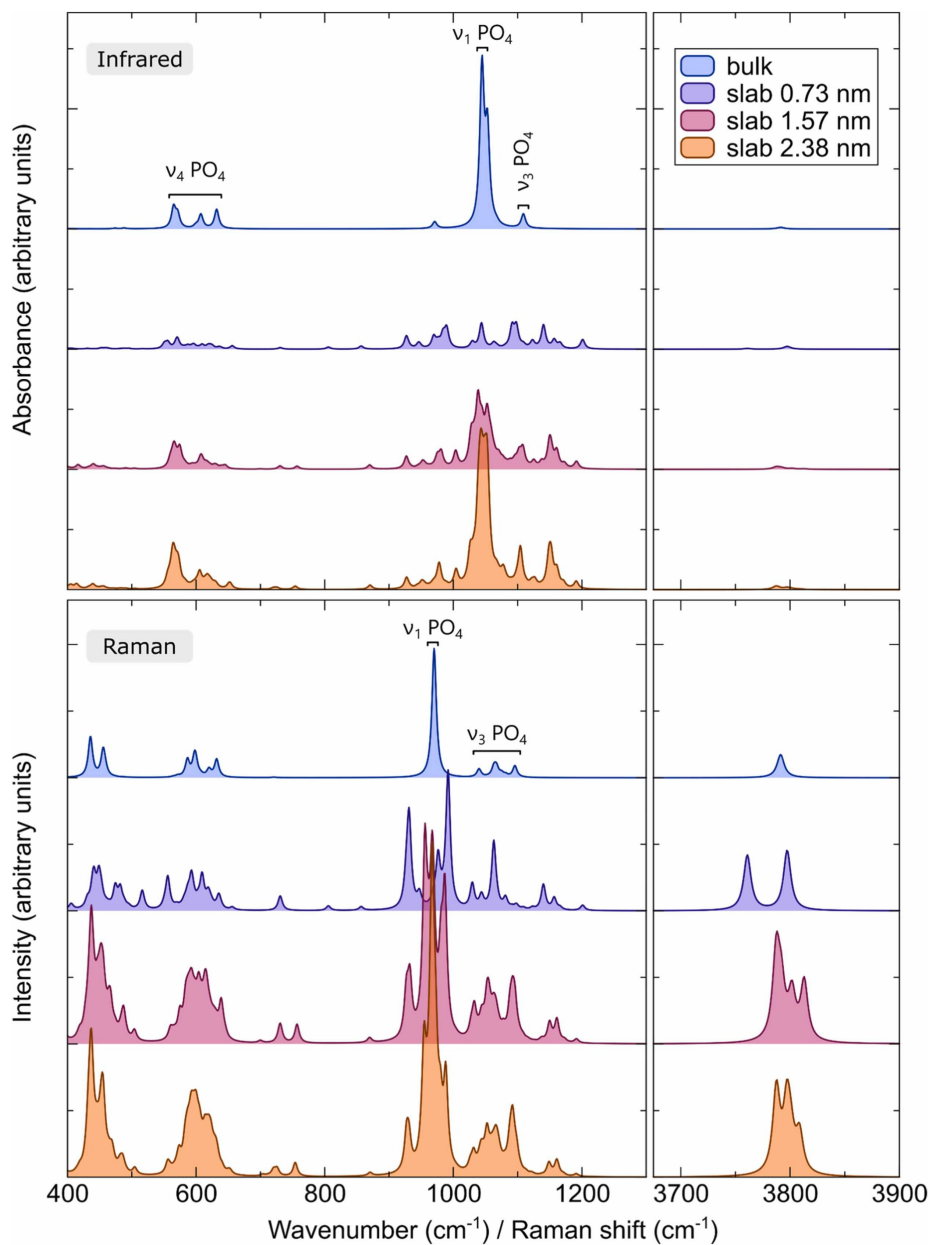
Figure 29: Comparison between the Infrared and Raman spectra of hexagonal hydroxyapatite as a bulk material and slab with increasing thickness in the spectral region between 400 cm^{-1} and 1300 cm^{-1} and the OH stretching region between 3725 and 3850 cm^{-1}. The spectra have been offset and the wavenumbers between 1300 and 3725 cm^{-1} have been omitted to aid visualization. vibrational

System	No. of OH sites	Harmonic frequency cm^{-1}	Anharmonic stretching frequency cm^{-1}	Δcm^{-1}
Hexagonal (010) 1 layer	2	3777.7	3607.2	170.5
		3749.7	3585.3	164.4
Hexagonal (010) 2 layers	4	3771.1	3612.7	158.4
		3761.6	3589.2	172.4
		3783.7	3625.1	158.6
		3763.6	3600.9	162.7
Hexagonal (010) 3 layers	6	3771.4	3613.0	158.4
		3762.4	3591.2	171.2
		3767.1	3607.1	160.0
		3766.4	3605.6	160.8
		3782.1	3622.9	159.2
		3759.4	3596.7	162.7
Type B (100)	6	3777.7	3613.8	163.9
		3758.7	3598.2	160.5
		3768.5	3608.4	160.1
		3748.0	3585.9	162.1
		3884.7	3725.4	159.3
		3817.0	3658.1	158.9

Table 8: Vibrational frequencies of the O-H stretching mode corrected for anharmonicity in the relevant studies OHAp systems. All values reported for the B3LYP functional.

resulted in an asymmetric slab with differently terminated surfaces on either side (Fig. 30). Here the Ca ring structure that contains the OH group in the bulk was longitudinally cut and the most stable configuration of the system was found with the (010) surface terminated by the exposed OH groups and the (010) terminated by Ca ions (complete values listed in Table 7). When the slab is a single layer thick (0.73 nm), the OH groups angled upwards from the surface and changes in the site characteristics related to this group resulted in splitting of the OH ν_1 band to 3607 and 3585 cm^{-1} (values corrected for O-H stretch anharmonicity). Unlike the bulk, these bands also become IR active and were clearly visible in the predicted IR spectrum (Fig. 29). Creation of the single layer slab also resulted in a tripling of the number of bands within the region between 400 and 1800 cm^{-1}. The bands at 556 and 656 cm^{-1} are dominated by the OH δ vibrational mode and could be observed in both the predicted Raman and IR spectra. Visualizations of the computed vibrations associated with the different modes demonstrate that although some modes are degenerate in the bulk, these modes are found at different spectral positions when a surface is introduced as the phosphate groups at the OH terminated surface required lower energies (IR and Raman band found around 550 cm^{-1}) than those closer to the centre of the slab (IR and Raman band found around 571 cm^{-1}). This difference also explains some of the additional bands in the phosphate ν_1 and ν_3 region between 900 and 1200 cm^{-1}, which were related to vibrational modes of phosphate ions positioned away from the hydroxyl groups, e.g., the IR and Raman active band at 927 cm^{-1}. For the same type of vibration, such as ν_3 PO_4 stretch, phosphate closest to the OH groups occurred at the highest wavenumbers.

Increasing the layer thickness produced Raman and IR spectra that showed more similarities to the bulk hydroxyapatite spectra. At two layers thickness (1.57 nm) the system had enough atoms that two distinct OH regions were present, the first exposed at the surface due to the cut through the (010) plane and the second enclosed within a bulk- like Ca ring, see Fig. 30, when the simulation cell is orientated along the x axis which is parallel to the c axis of the crystal structure. This led to the presence of four active modes within both the IR and Raman spectra, where the three modes found at the lowest wavenumbers (see Table 8 for complete anharmonic values) belonged to the OH groups within the bulk-like Ca ring and the mode at higher wavenumbers (3625 cm^{-1}) corresponded to the symmetric stretch of the OH groups at the (010) surface. In the case of the three-layer system (thickness of 2.38 nm), reconstruction of the material resulted in the presence of three distinct OH sites: at the OH terminated surface, within a distorted Ca-ring and within a bulk-like Ca ring and produced six vibrational modes that were both IR and Raman active. Three of these modes were dominant as they have the highest intensity of which the central band at 3613 cm^{-1} corresponded to the symmetric stretch of OH groups at the surface. Thus, when the thickness was greater than 2 nm, the surface groups no longer correspond to the modes with the highest wavenumbers, although they remained more energetically demanding than the bulk mode (band at 3598 cm^{-1}).
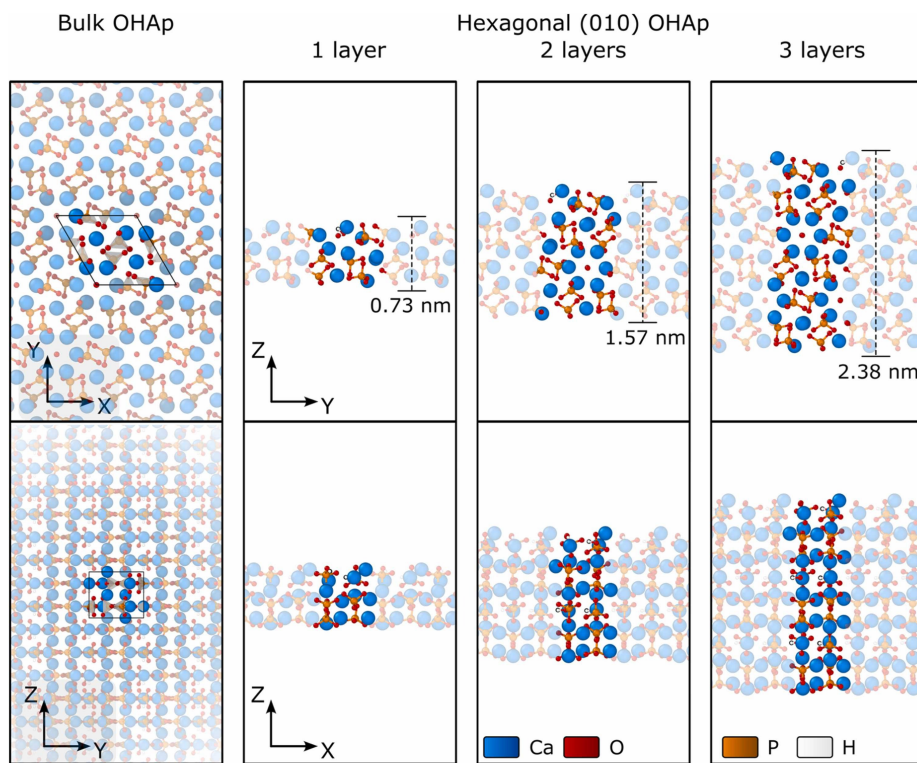
Figure 30: Optimized crystal structures of bulk hexagonal hydroxyapatite together with the (010) surface with increasing surface thickness in views along the x and y axes. The vividly coloured atoms represent the unit simulation cell, while the transparently rendered ones represent 2D periodic images. The thickness of the respective slabs is indicated as well.

Between the slabs of 0.73 and 2.38 nm thickness the number of active vibrational modes in the spectral region 400–1800 cm^{-1} also tripled, although many were predicted to have very low intensity. Shifts in bands can be related to changes in the energy required for specific modes that are directly controlled by the chemistry of the next atoms within a crystal structure. This is the result of many factors including a change in the intramolecular force, where a weakening results in a redshift and a strengthening would result in a blue shift[295]. For example, in carbonate minerals that have the same crystal structure a variation of 0.02 Å in the C-O bond length due to the difference in adjoining cations results in a blueshift shift of up to 15 cm^{-1} in the Raman vibrational modes[296, 297, 298]. In contrast, changes in the structure of a site, e.g., due to differences in the coordination with cations or shifts in the atomic positions both of which can occur related to surface reconstruction, would result in the production of new bands within the vibrational spectra. These new bands could have a red or blue shift depending on the characteristics of the new site. It can be seen from the pair distribution function (Fig. 28) that such changes in bond length do occur within the structure upon the formation of a 2.38 nm thick slab. Similarly, it can be seen from Fig. 30 that there is a shift in the orientation of groups such as the phosphate when they are exposed at the surface. Therefore, shifted surface phonon bands most likely represent a change in the intramolecular force within a vibrating group in response to changes in the distance to the next atoms and bond length within the group. Here, red shifted would reflect a lengthening of the intramolecular interactions whereas blue shifted is the result of a shortening implying a stronger bond, both of which can be observed in the P-O distances in Fig. 28. In the ν_4 phosphate spectral region increasing the layer thickness resulted in an increase in the IR intensity of the most bulk-like environment band (at 632 cm^{-1}) with equivalent bands related to the OH-terminated surface found at lower wavenumbers (630 cm^{-1}) and the Ca-terminated surface at higher wavenumbers (640 cm^{-1}) in the thickest slab. Similarly, the bulk phosphate ν_1 was found at 971 cm^{-1}, whereas the OH- and Ca-terminated surface bands were found at 956 and 988 cm^{-1}, respectively. However, this is the opposite behaviour to the δ OH bands whereby the OH groups just below the Ca-terminated surface were found at lower wavenumbers to the bulk-like OH groups, 555 and 571 cm^{-1}, respectively, and the OH-terminated surface groups had the highest energy (found at 573 cm^{-1}). In previous work with another insulator, namely diamond, phonon confinement resulted in the shift of vibrational bands to lower wavenumbers compared to that of the bulk material[299]. In contrast, our DFT calculations demonstrate that surface phonon bands are expected to appear at both higher and lower wavenumbers than the bulk groups, where the exact behaviour is dependent on the surface termination. Surface phonon related bands decreased in intensity relative to bands with bulk contributions as the slab thickness increased (Fig. 29). As the largest simulated surface system has a size closest to that expected in bone minerals, had a fully converged surface energy (see Table 7 for complete results) and shows both bulk as well as surface phonons, we used slabs of thickness greater than 2 nm to evaluate the different types of
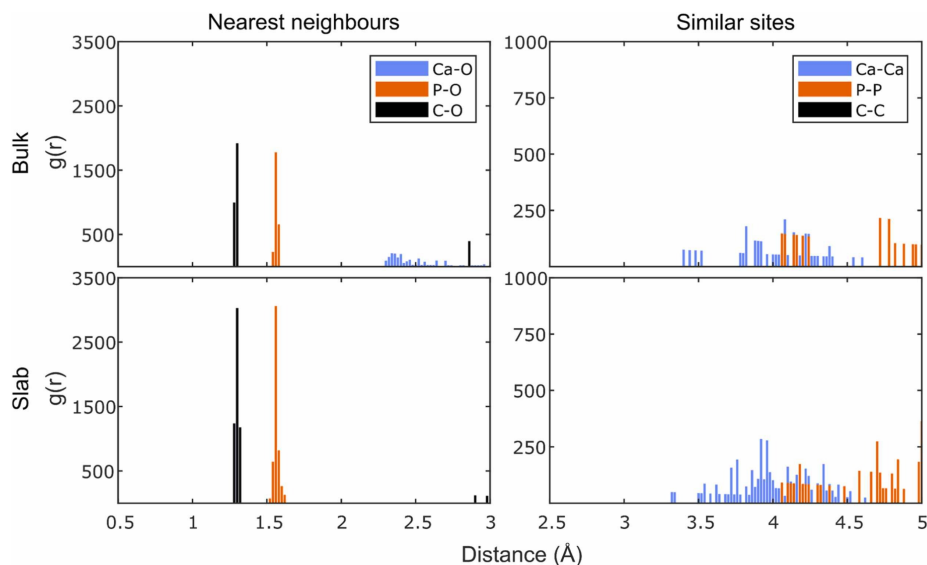
Figure 31: Pair distribution functions for the A-type apatite bulk and slab are shown for the nearest neighbour interactions as well as similar site distribution. There were no C-C pairs found below 5 Å distance in this material.

carbonated hydroxyapatite.

10.4.2 Type A carbonated apatite

In type A carbonated apatite the OH groups were replaced by CO_3^{2-} groups. Despite this substitution, most PO_4 groups show the same bond lengths as in the hexagonal hydroxyapatite structure with a few groups deviating by up to 0.02 Å (c.f. Fig. 28 and Fig. 31). Whereas the Ca-O groups show some distortion with the majority of sites showing a bond length of 2.4 Å. Spectroscopically, substitution of carbonate in the OH site results in a loss of the OH spectral bands and the introduction of carbonate related bands in the vibrational spectra (Fig. 31a). For example, the IR active carbonate ν_2 band was observed at 873 cm^{-1} and the ν_3 antisymmetric stretch was found at 1519 and 1604 cm^{-1}. The ν_1 carbonate symmetric stretch was only visible in the Raman spectra at 1130 cm^{-1}. Phosphate related bands showed the same behaviour as described for hydroxyapatite above, but the ν_1 symmetric stretch shifted to 960 cm^{-1}. Although the exact band positions are about 10 cm^{-1} off between the DFT model and experimental observations, a downshift of 10 cm^{-1} for the phosphate symmetric stretch in the Raman spectrum has also been reported for synthesized A-type carbonated apatite[184].

The most stable surface for this system was found to be the (100). In this case, both sides of the slab were terminated by Ca and phosphate groups with the carbonate groups occupying the Ca-ring structure about 3 Å below the

surface (Fig. 32). As for the hexagonal hydroxyapatite, formation of a more than 2 nm thick slab caused the formation of PO_4 group with different bond lengths. Although the C-O bond lengths were only minimally affected by the presence of a surface, their shape became distorted as the internal angles in the bulk-like centre of the slab were 117, 118 and 125∘ between O-C-O, whereas the two carbonates close to the surface had angles of 119, 120 and 121∘ or 117, 119 and 124∘. A change in the Ca groups was also observed as a different distribution of the Ca-O lengths as well as changes in the spacing between different PO4 groups and Ca sites (c.f. Fig. 31c and Fig. 31d). In addition, as before the slab showed a tripling of the bands present in the vibrational spectra. This included clearly visible carbonate bands in the IR and Raman spectra due to three distinct carbonate bearing Ca-ring channels in the three-layer slab, one close to each surface and the third running through the centre of the slab (Fig. 33). For example, in the carbonate ν_2 spectral region, the most bulk-like carbonate channel was found at 877 cm^{-1} (Table 10.4.2), thus was shifted to higher wavenumbers than observed in the bulk. Whereas the carbonates associated with the surface were found at 881 and 884 cm^{-1}. Similarly, the two ν_3 antisymmetric carbonate stretch were split into six bands upon the formation of the slab. However, no shift of the band related to an asymmetric stretch in the [010] direction, or the bulk-like bands (found at 1604 cm^{-1}) was found, in contrast to the large shift to 1546 cm^{-1} for the asymmetric stretch along [001]. In addition, unlike the ν_2 bands where the surface related vibrations were found at higher wavenumbers compared to the bulk-like, for the ν_3 bands the surface phonons were observed to appear at lower wavenumbers. For the Raman active ν_1 symmetric stretch of carbonate the bulk-like central channel was shifted to 1128 cm^{-1} whilst the surfaces appear at lower wavenumbers e.g., 1093 cm^{-1}. There was, however, significant overlap with the surface and bulk phonons related to the asymmetric stretch of phosphate that are also present in this spectral region.

Table 9: Carbonate group positions for different materials studied. (I) refers to bands that are predicted to have zero spectral intensity for a specific simulation. [a]bulk-like group in centre of slab, [b]surface group.

CO_3 mode	Activity	A-type		B-type		AB-type (1x1x1)		AB-type (2x2x1)	
		Bulk	Slab	Bulk	Slab	Bulk	Slab	Bulk	Slab
ν_4	IR (weak) Raman (strong)	661 (I) 675 697 (I) 721 (I) 761 (I)	662[a] (I) 677[b] (I) 688[b] (I) 696[a] (I) 701[b] (I) 716[a] (I) 721[b] (I) 739[b] (I) 758[b] (I) 762[a] (I) 788[b] (I)	705 714	702[b] 705[a] 708[b] 716[b] 718[a] 725[b] 729[b]	662 693 721 760	661[a] 677[b] 693[a] (I) 701[b] 716[a] 721[b] 738[b] 758[b] 761[a] 787[b]	664 691 719 782	659[b] 664[a] 688[a] 692[a] 706[b] 721[a] 738[b] 787[a]
ν_2	IR	873	870[b] (I) 874[b] (I) 877[a] 878[b] (I) 893[b] (I) 895[a] (I)	875	868[b] 875[a] 876[b]	875 890	870[b] 874[b] 877[a] 878[b] 893[a] 895[b]	877 899	878[ab] 887[a] 892[b]
ν_1	IR Raman	1130	1090[b] 1093[b] 1101[b] 1106[b] 1130[a] 1134[a]	1108	1106[a] 1108[b] 1112[a] 1130[b]	1085 1091	1080[a] 1090[a] 1095[b] 1105[b] 1129[b]	1098 1127	1062[b] 1080[b] 1099[a] 1129[a]
ν_3	IR (strong) Raman (weak)	1519 1605	1442[b] 1447[a] 1467[a] 1474[b] 1479[b] 1501[b] 1541[a] 1558[b] 1577[b] 1586[b] 1609[a] 1621[b]	1480 1562	1468[b] 1473[b] 1482[a] 1574[a] 1592[b] 1638[b]	1442 1468 1546 1593	1442[b] 1447[a] 1467[a] 1474[b] 1479[b] 1500[b] 1541[b] 1558[b] 1579[b] 1586[b] 1609[a] 1622[b]	1471 1503 1565 1610	1389[b] 1415[b] 1474[a] 1492[b] 1513[a] 1569[a] 1612[a] 1652[b]

10.4.3 Type B carbonated apatite

The bulk material of type B carbonated apatite (modelled in a simulation cell as outlined in earlier works [235, 185]) showed a similar behaviour to the hydroxyapatite with little change in the nearest neighbour distances (c.f. Fig. 28 and Fig. 34). Similarly, the OH symmetric stretch was visible in the Raman spectrum but had a very low intensity in the IR spectra. However, unlike the bulk hydroxyapatite, the Raman spectrum already showed a splitting of the OH symmetric stretch into two separate bands (Fig. 35) due to the change in the symmetry of the material upon carbonate substitution from $P6_3$ to P1. When the carbonate is substituted for phosphate with co-substitution of a neighbouring Na^+ in a Ca2 site, rather than OH as in the A-type carbonate, some C-O bonds increase in length to 1.32 Å (Fig. 34). These changes resulted in a shift of the carbonate antisymmetric stretch (ν_3) doublet visible in the IR from 1519 and 1604 cm^{-1} in A-type carbonated apatite to 1480 and 1562 cm^{-1} in the B-type. This is consistent with previous DFT and experimental studies[12]. In contrast, the carbonate bend was only shifted by 3 cm^{-1} in comparison to the same band found in A-type carbonate. Again this shift agrees well with reported computational work and experimental work[12, 268]. The phosphate bands showed the same behaviour as the hydroxyapatite, with the exception that the carbonate symmetric stretch was visible at 1108 cm^{-1} and obscured the phosphate antisymmetric stretch in this spectral region.

Cutting the structure along the (100) plane resulted in a similar carbonate distance from the surface to that found with the A-type carbonated apatite, but now the (100) surface was Ca-terminated whereas the (100) also had exposed OH groups. There is another carbonate site within the bulk at around 10 Å from either surface. O-C-O angles within the carbonate changed from 119, 120 and 121∘ in the bulk-like site within the slab to 119 and 123° or 116, 120 and 124° in the carbonate groups at the surfaces. The presence of the surface and the structural rearrangements that occur due to this resulted similar Ca-O bond distances as well as a shortening of the distance between different Ca and OH groups (Fig. 34). As observed for the hydroxyapatite slab, the number of spectral bands tripled between the bulk and slab. Again, the vibrational modes with the highest wavenumbers were associated with the Ca-terminated surface, including those of carbonate. However, carbonate modes associated with the bulk site were found at the lowest wavenumbers. Interestingly, the OH mode at lower wavenumbers predicted for the bulk is absent in the spectrum of the cut structure, whereas all surface related bands are located at higher wavenumbers to the bulk band at 3778 cm^{-1}.

10.4.4 Type AB carbonated apatite

Two sizes of simulation cell were tested for the AB-type carbonated apatite. In the smaller cell incorporation of carbonate at both the A- and B-type sites means that no OH was present in the simulation cell. The carbonate groups were also separated by only 3.9 Å (Fig. 36), meaning that they are both localised around
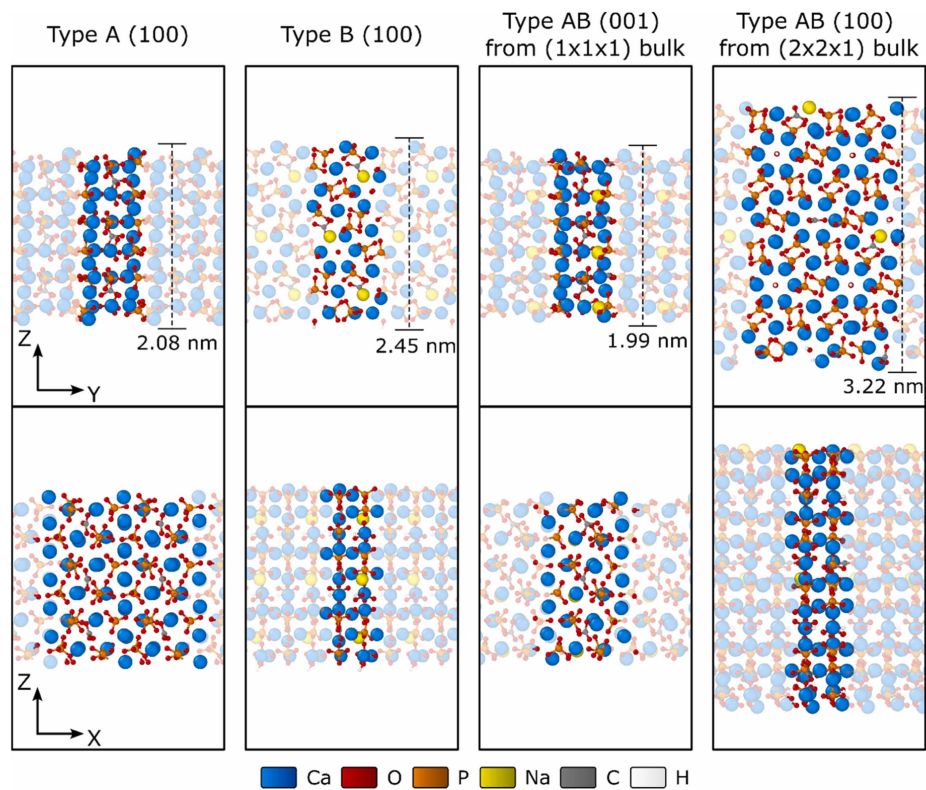
Figure 32: Optimized crystal structures of the A-type, B-type, and AB-type carbonated apatite surfaces in views along the periodic axes. The vividly coloured atoms represent the unit simulation cell, while the transparently rendered ones represent 2D periodic images. The thickness of the respective slabs is indicated as well.
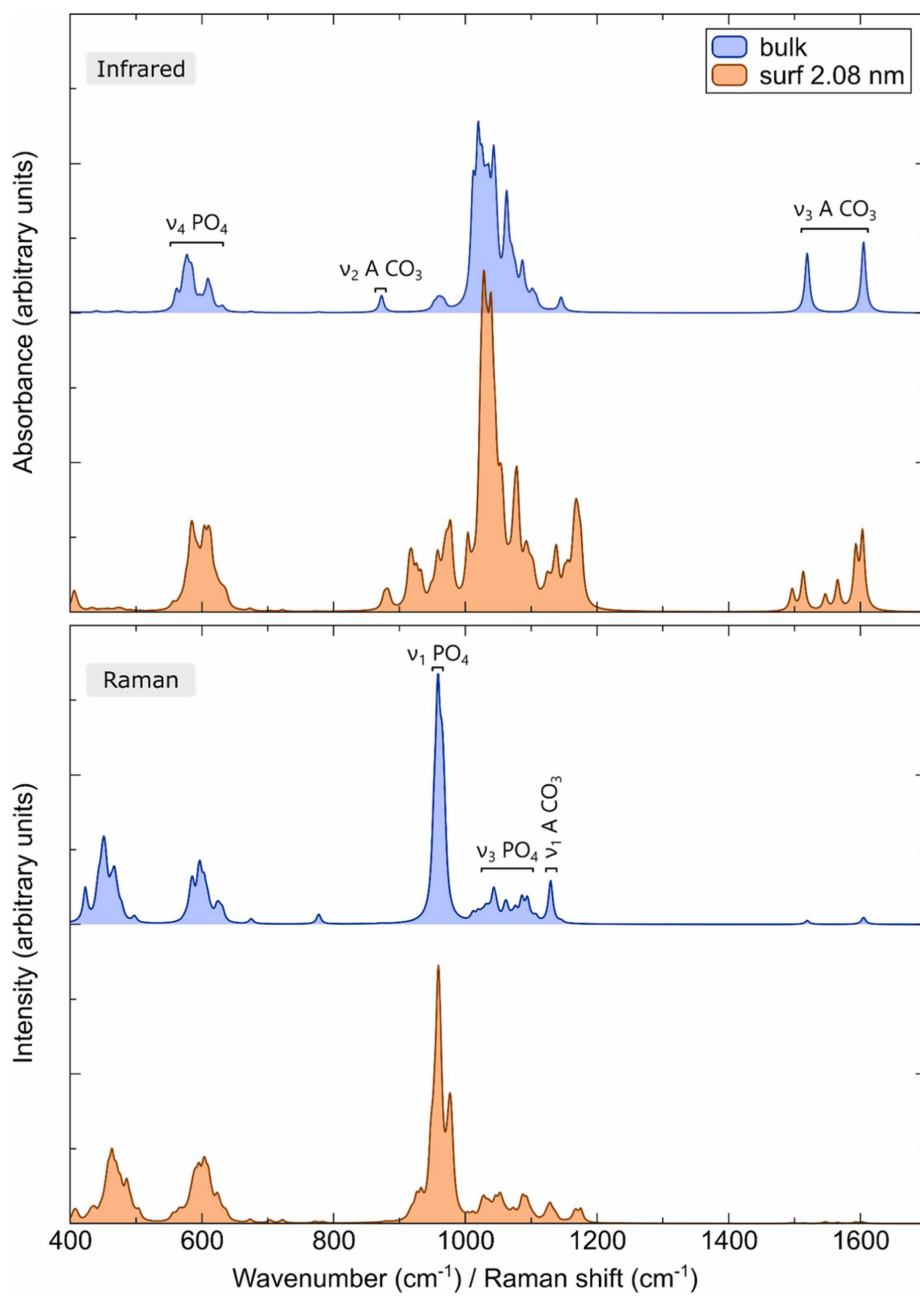
Figure 33: Infrared and Raman spectra of apatite with carbonate substituting for the OH group, thus A-type carbonate. The spectra for the bulk and a slab with a thickness of 2.08 nm are shown and have been offset for clarity. Note, as the carbonate group has replaced the OH groups there are no bands predicted above 1700 cm^{-1}.
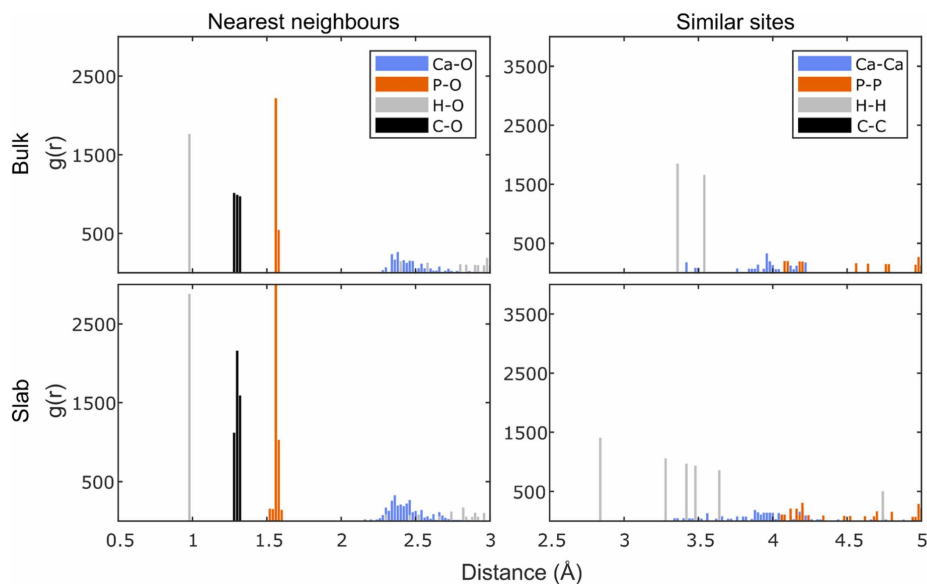
Figure 34: Pair distribution functions of the B-type hydroxyapatite between nearest neighbours and similar sites in the bulk and the slab simulated structures.

the same Na+ ion within the simu- lation cell (Fig. 32). In contrast, expansion of the simulation cell to double the size in the [100] and [010] direction enabled us to probe the effect of a more diluted carbonate concentration and when the carbonate groups are separated by more than 5 Å. The larger simulation cell also included OH groups as not all were substituted by carbonate. Increasing the cell size did not produce a difference in the spacing between nearest neighbours and these spacings replicate those found in the other carbonated apatite structures. However, extension of the cell parameters allowed us only to simulate the IR spectrum as the Raman spectral features are more computationally expensive to evaluate. Therefore, the information below focuses on the IR spectra only.

For both simulation cell sizes, the bulk AB-type carbonated apatite produced spectral features that are a mixture of both the A- and B-type carbonate models described above. In both simulation cell sizes the phosphate dominant v1 stretches were found close to 960 and 970 cm^{-1}, consistent with what was observed in the A- and B-type carbonated apatite simulations, respectively. Similarly, in the larger simulation cell that included OH groups two dominant vibrational bands were found in the OH stretching spectral region, comparable with what was observed in the B-type model. However, interestingly the most intense band in this region was found at much lower wavenumbers (3609 cm^{-1}), similar to what is observed experimentally in hydroxyapatite, even without taking into account the effects of anharmonicity. The carbonate ν_2 region of the IR spectra both A- and B-type carbonated apatite showed similar band positions,
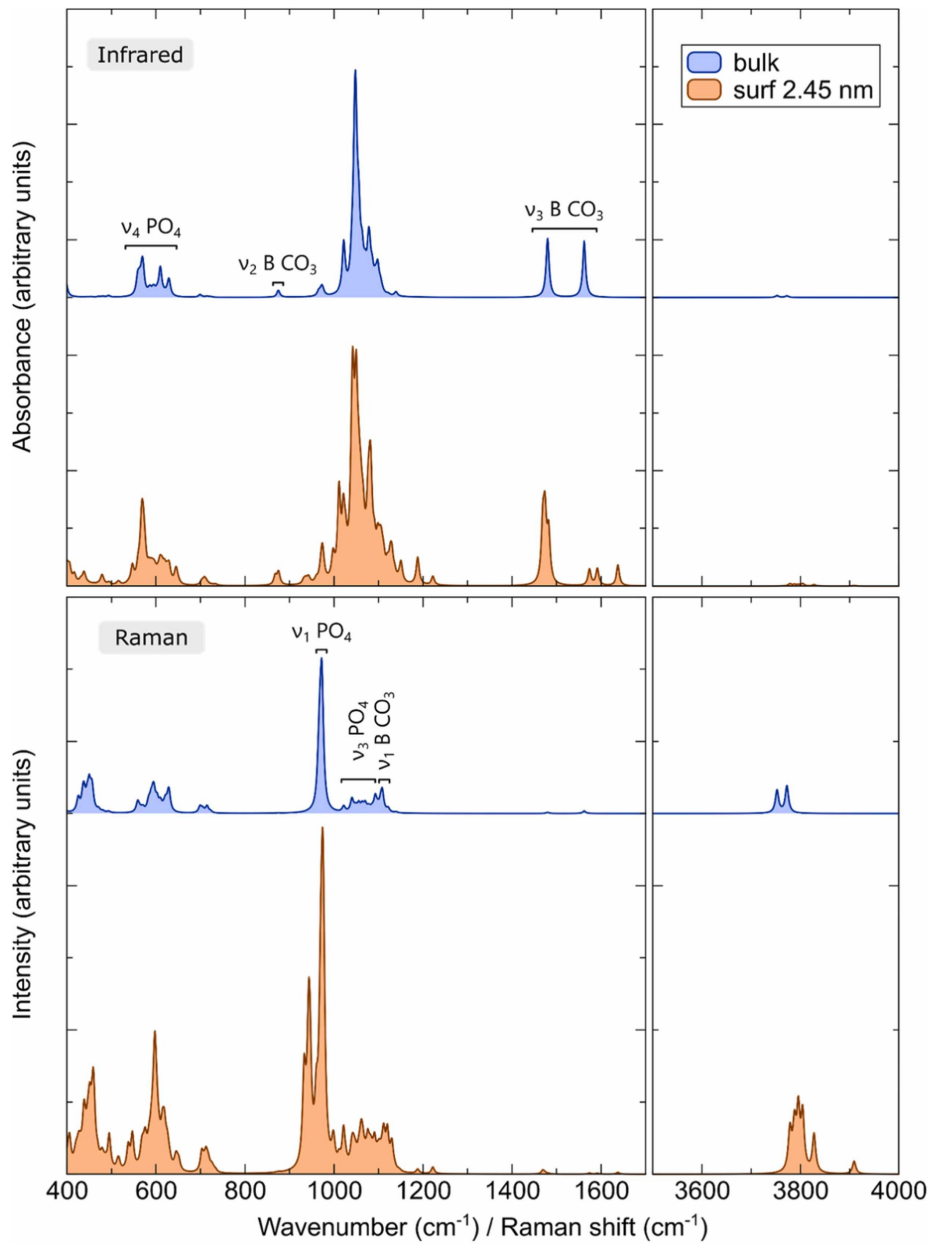
Figure 35: A comparison between the infrared and Raman spectra of B-type carbonated hydroxyapatite for the bulk and slab with thickness of 2.45 nm.
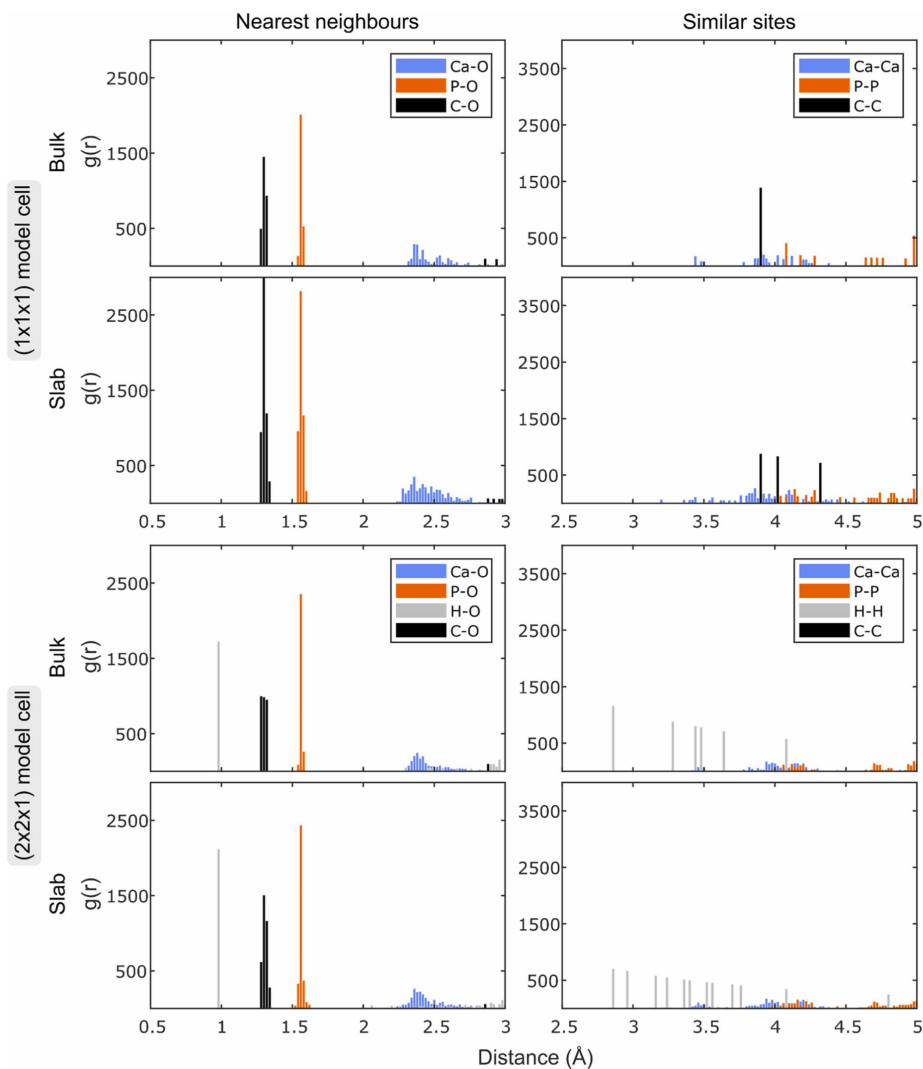
Figure 36: Next site pair distribution functions found for the bulk and slab of the 1×1×1 and 2×2×1 simulation cell sizes of the AB-type carbonated apatite. Note, in the 1×1×1 model all OH groups are substituted by a carbonate group therefore there are no H-H distances to report. Similarly, the C-C distance in the 2×2×1 simulation cell is larger than 5 Å thus was not plotted.

873 and 875 cm^{-1}, respectively. However, in the AB-type structure with the small simulation cell these bands became separated with the A-type carbonate apatite found at higher wave- numbers (891 cm^{-1}). With the larger cell two A-type sites ν_2 bands were found at 887 and 892 cm^{-1}, where the 892 cm^{-1} band had the highest intensity. This is comparable to the relationship between these bands reported in the literature, however, the A-type site is 10 cm^{-1} higher than described previously for synthesised materials[293]. Similarly, the presence of both carbonate in A- and B-sites resulted in the doubling of the bands found in the ν_3 antisymmetric stretching region between 1450 and 1650 cm^{-1}. In the small simulation cell, these bands were found at lower wavenumbers than in the A- or B-type models (Table 10.4.2). Whereas expansion of the model to space the carbonates groups further apart resulted in the ν_3 antisymmetric stretching region that more closely corresponded with the band positions found in the A- and B-type only models. Previous experimental work on AB materials reported six bands in this region within the IR spectra, attributed to two different A-type sites present in the materials synthesized[293]. In the smaller model, A-type carbonate occupies only one site. However, in the larger simulation cell there are indeed two different A-type and 2 different B-type sites present in the bulk, which each produced multiple bands in the ν_3 antisymmetric stretching region (Fig. 37). Thus, the larger simulation cell is a better representation of the structure found in synthetic AB-carbonated apatites. This is further supported by the positioning of the ν_1 symmetric stretch bands, which are expected to be IR and Raman active in this material, albeit with low intensity in the IR spectra. For these bands the position found with the smaller simulation cell showed an erroneously low band position for the A-type carbonate of 1080 cm^{-1} compared to that described from bone and dentine samples [268, 184]. In contrast, the presence of carbonate groups that are spaced further apart in the structure resulted in a shift of the A-type carbonate band back to the same position as found in the A-type only model (Table 10.4.2) that is also consistent with previous observations of AB-type carbonated apatite materials as well as bone and dentine. This is also consistent with the phosphate ν_4 spectral region findings where no bands are predicted between 520 and 530 cm^{-1} in the smaller simulation cell. In contrast, experimental data of bone apatite does show bands in this region [300] as does the 2×2×1 simulation of AB-type carbonated apatite (comparative spectra reported in Fig. S1).

Unlike the A- and B-type carbonate apatite models, termination of the the AB-type carbonated apatite along the (001) plane resulted in the production of a slab with the B-type carbonate exposed at the (100) surface for both simulation cell sizes. In addition, in the larger simulation cell the ($\bar{1}$00) surface contained an A-type group. Introduction of the surfaces follows the same trend as observed before where the number of bands triples for both sizes of simulation cell. As for the OH groups in the hydroxyapatite and B-type carbonate, the carbonate groups exposed at the surface of the smaller simulation cell show the highest energy for the vibration, whereas the bulk groups (deeper than 10 Å into the structure) had a band at the lowest wavenumber for a specific vibrational mode. Although there are many bands in the spectral region between 1000 and 1200
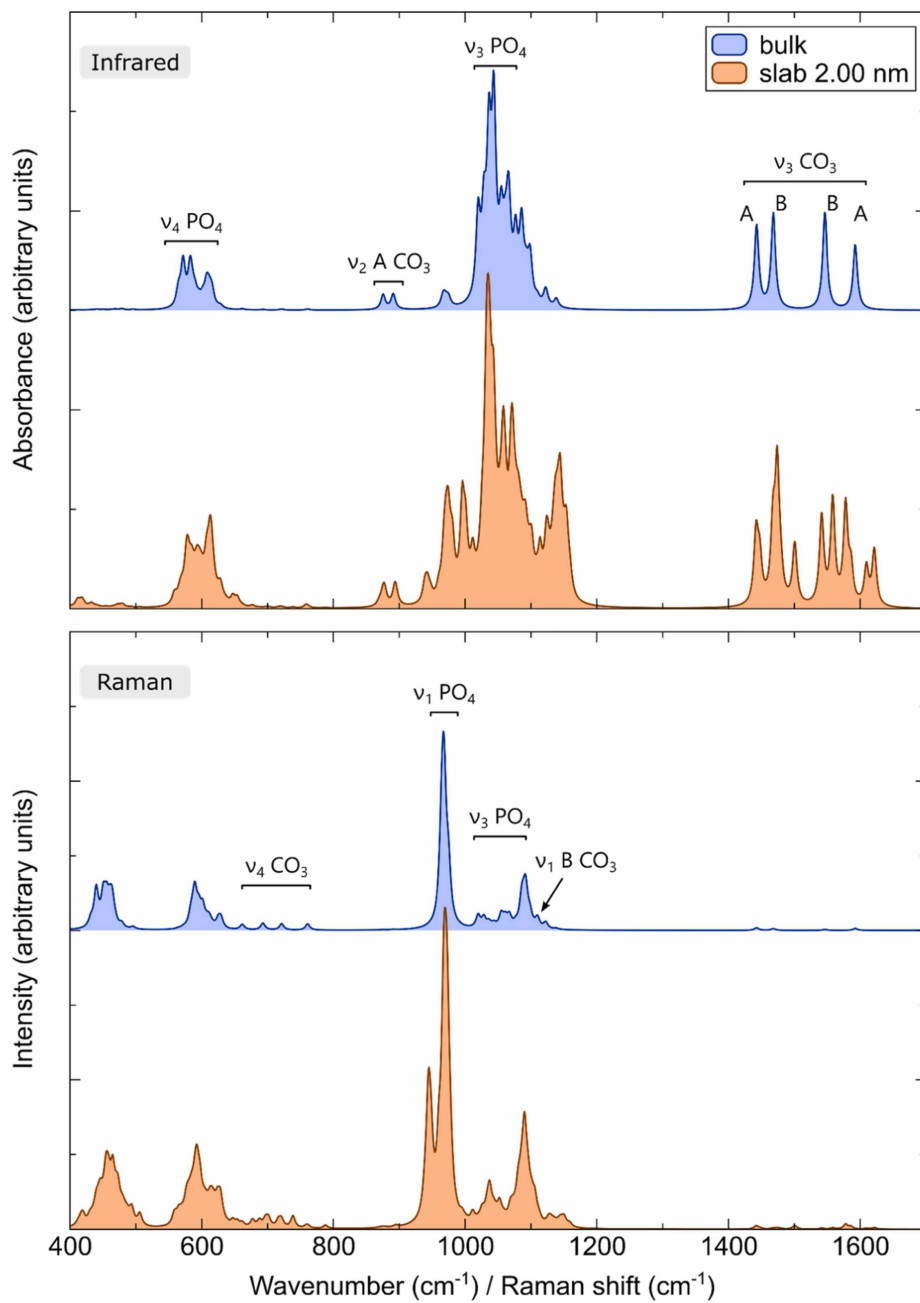
Figure 37: Infrared and Raman spectra of AB-type carbonated apatite modelled in 1×1×1 simulation cell. Spectra are offset for clarity.

cm^{-1} most bands were mixed modes between phosphate antisymmetric stretch and carbonate symmetric stretch modes. For the bulk IR spectra two bands were found for the carbonate ν_2 domain at 875 and 890 cm^{-1}, where the first band corresponds to the B-type carbonate and the second to the equivalent motion of the carbonate in the A-type site. Upon formation of a slab these bands are split (Table 3) where new bands related the carbonate B-site are shifted from the bulk by 5 cm^{-1}. A-type carbonate showed a larger shift of 14 cm^{-1}. This is consistent with a deformation of the carbonate sites where O-C-O angles were originally 114, 120 and 126° or 118, 120 and 122° for A and B bulk-like sites within the slab, respectively. Whereas these became 117, 119 and 124° or 114, 119 and 127° in the surface A and B sites, respectively. For the larger simulation cell A type carbonate showed a shift of the ν_3 and ν_4 surface bands to lower wavenumbers, whereas the ν_2 band was shifted to higher wavenumbers. In contrast, new bands appeared at both higher and lower wavenumbers related to the surface B-type carbonate in the ν_2 spectral region and the band was not affected by changes in the structural environment.

10.4.5 Implications for bone related research

The exact surface configuration related to bone will be more complex than what can be modelled here as surface stabilities are related to the adsorption of organic and inorganic components in the solutions from which the crystals grow, the structural chemical substitutions and how adsorbed and substituted ions vary as the bone/crystallites mature, all of which will affect the final crystal morphology [301, 302]. However, the importance of surface phonons can be evaluated initially by looking at the most stable surfaces of the structures simulated without adsorption effects, as these have the lowest surface energy and thus the least difference to the bulk structure. The Raman ν_1 phosphate mode showed the least overlap with other vibrational modes in the different slab thickness simulations of hydroxyapatite and showed individual bands for the groups directly at each surface and within the centre of the three-layer slabs. Therefore, this band has an intensity that was not influenced by other vibrational modes in the hydroxyapatite model. As the surface phonons were so dominant in the modelled hydroxyapatite, there was only a 1% change in intensity ratio related to bulk and surfaces phonons of this mode between the 1.57 and 2.38 nm thick systems. In the 2.38 nm thick system, the band position for phosphate in the centre of the slab was the same as in the crystal bulk simulation. If the intensity of a vibrational mode can be related to the concentration of a specific group when site symmetry is retained e.g.,[303], then the intensity of the bulk sites should increase linearly with increasing slab thickness. In contrast, the intensity of the bands related to the surface sites would be expected to remain constant as the slab thickness increases. Therefore, it is possible to estimate the importance of the surface phonons on the Raman spectrum in systems with a thicker slab than can be modelled (Fig. 38). In this case, the intensity ratios were found assuming the in- tensities from the 2.38 nm thick slab system but doubling the intensity of the bulk whilst holding the surface phonon intensity constant.

Based on this analysis in the smaller AB-type carbonated apatite system, as the Raman activity cannot be modelled in the larger system, both the carbonate- and phosphate-terminated surfaces would be expected to show a quarter of their intensity when the hydroxyapatite slab thickness reached 8 nm. The contribution of the surface bands then becomes minimal at even larger sizes, consistent with the thin film literature where sintered apatite particles estimated to be $\sim$ 20 nm in size based on X-ray diffraction results and a maximum agglomeration size of 50 nm based on scanning electron microscopy, already show bulk like Raman and IR spectra with no clear evidence of additional bands or significant broadening effects[304].

Given the plate-like structure reported for bone crystallites and their typical thickness in the shortest direction of $\sim$ 5 nm [278, 305], which is perpendicular to the surface with the largest area, surface phonons modelled for hydroxyapatite should be able to influence the measured vibrational spectra. Our simulations demonstrate that both small changes in bond length as well as distortion of site structures has a large effect on the spectral features. Fig. 38 shows that different bands may have varying contributions to the spectrum, but several bands that are used to analyse carbonate content of apatites, e.g., the 1400 cm^{-1} IR bands (ν_3), are expected to be influenced by surface phonon contributions and as the bands studied here reflect the phosphate and carbonate groups exposed at the surface itself, it is expected that phonons related to other apatite surfaces will show a similar behaviour[306].

There is a significant shift related to the Ca-terminated surfaces in the thickest hexagonal HAp system, which could be resolvable in vibrational spectroscopy analysis. For example, reports of nano-apatite indicate that there is a shift to higher wavenumbers for at least one IR phosphate asymmetric stretching band[307], thus this could be a surface phonon effect. Comparison with bone analysis demonstrates that multiple changes occur in the IR spectra that affects both the phosphate and carbonate bands. Firstly, the phosphate ν_4 domain shows evidence for three new bands when poorly crystalline material is present, two in the region between 520 and 530 cm^{-1}, and two between 540 and 550 cm^{-1} that are attributed to HPO_4^+ substitution within apatite. In addition, a labile phosphate environment is invoked to explain additional bands in the $610 - 615$ cm^{-1} region[300]. Whilst the production of a nanometre sized apatite slabs did create new bands at lower wavenumbers, the maximum shift was 5 cm^{-1} in this spectral region. Therefore, previous reports of HPO_4^+ environments in bone apatite based on IR data deconvolution and identification of a band at 550 cm^{-1} cannot be accounted for by the presence of surface phonons. Secondly, additional complexity in the shape of the band envelope for the carbonate ν_2 modes has been attributed to the presence of A, B and non-apatitic carbonate sites within bone crystallites[268]. The spectral positioning of this band is comparable to the surface phonon carbonate ν_2 modes in our B-type model as well as smaller AB-type simulated cell. However, a similar shift was not observed in the larger AB-type simulated system. Therefore, the 'non-apatitic' environment is probably a reflection of the presence of significant proportion of surface sites in bone crystallites that are populated by carbonate groups.

99
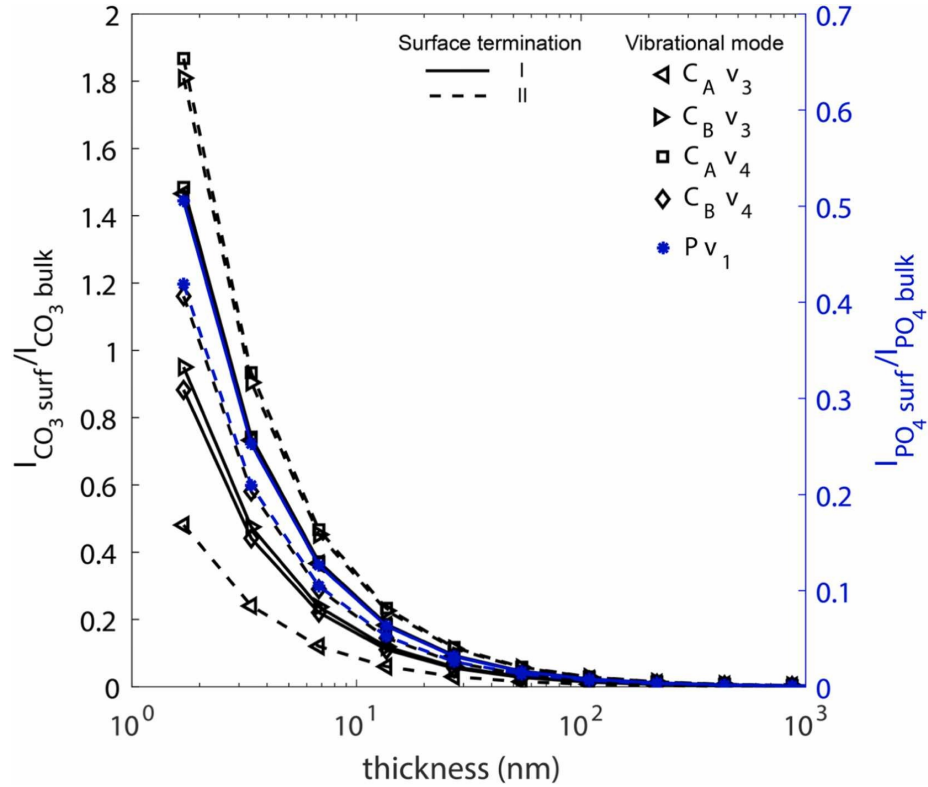
Figure 38: Estimates of the surface phonon contributions to vibration band intensities for different bands with increasing thickness of the slab based on the AB-type simulation. Ratios for the intensities of surface and bulk IR active ν_3 bands as well as Raman active carbonate ν_4 and phosphate ν_1 bands are plotted against slab thickness. C_n refers to the different carbonate sites present in the AB-type carbonated apatite. As there are two different terminations of the slab both cases have been plotted individually where ^{I} refers to the surface terminated with B-carbonate sites and ^{II} corresponds to the surface terminated with phosphate groups.

Similarly, the presence of a surface on the larger AB-carbonated apatite system produces an IR spectrum that has a band with two bands between 540 and 550 cm^{-1} that have a third of the intensity of the 526 cm^{-1} band, demonstrating that the band related to HPO_4^- can also be contributed to by surface phonons. Tissue aging has been reported to produce bone with higher crystallinity [308] with a concomitant decrease in the intensity of the non-apatitic environment signal[309]. Our simulations indicate that increases in crystallite size, which is also expected with aging[310], should produce a similar effect without changing the thickness of the reconstructed surface region, thus apparent loss of the 'non-apatitic' environment.

10.5   Conclusions

Density functional theory calculations of hydroxyapatite and carbonated apatite structures conducted in this work show similar properties to synthesized and natural materials related to their bulk configurations, and therefore are expected to be good first representations of the structures that may be encountered in bone. Surface phonons were found up to 40 cm^{-1} from the position of their bulk counterpart and shift to both higher and lower wavenumbers compared to the bulk depending on the surface termination chemistry of the crystal. This is contrary to quantum confinement effects that should be shifted to lower wavenumbers and only enough to cause a band broadening effect[299]. Generation of slabs shows that the presence of surface phonons can be significant up to nanometre thicknesses. They are estimated to remain visible in the spectra beyond the thickness of apatite crystals in bone, where the largest surface area, thus dominant surface phonons, should correlate with the shortest width of the crystals. Shifts in the bands due to the presence of a surface should be measurable in IR and Raman spectroscopy, however, the bands related to HPO_4^+ substitution cannot be accounted for by surface phonon effects. In contrast, we have observed the 'non-apatitic' environment signature in several of the tested configurations.

10.6   Acknowledgments

10.7   Appendix D. Supplementary material

Supplementary data associated with this article can be found in the online version at doi:10.1016/j.mtcomm.2023.106596.

11 Summary and Outlook

The presented thesis covers two different fields exploiting the power of density functional theory. DSSCs are the promising third generation of photovoltaic devices and their modelling with the support of the DFT can lead to the massive manufacturing process and commercialization. This provides a great opportunity for the community to use cheap and eco-friendly resources and finally get rid of the fossil fuels. Published papers in this thesis on DSSCs are mainly expanding our knowledge with new findings concentrating on the local hybrid functionals and many-electron dynamics. Local hybrids are a great alternative to the other density functional approximations for such heterogeneous systems at approximately the same computational cost as widely used global and range-separated hybrid functionals. Results show that one needs to be very careful using range-separated functionals since it yields unphysical level alignment with wrong HOMO-LUMO description which is confirmed via electron dynamics simulation and it is overestimating the experimental values presented in related papers. This kind of inaccuracy can be related to the dominant long-range charge transfer character and asymptotic behavior. With the local hybrid functionals we notice a more balanced description of the excited states, in the dyes alone and in combination with the semiconductor. The dyes structure needs to be closer examined, especially when it has the two donor groups, concerning the location of the HOMO orbital, if it is just on the one donor, then we need to include more orbitals, near the HOMO, to get the stronger values in the oscillator strengths. Calculated charged injection showed that we have some good candidates for the improvement of the DSSCs with 60% to 80% of efficiency. Since this family of flexible local hybrid functionals are still an ongoing development, we need much more work and comparisons in order to draw some further conclusions. It would be interesting to follow the group of range-separated local hybrids and use them for such studies. Experimentalists are providing new set of dyes on daily basis which are the key component in the whole nomenclature of the system. Their different structure has a significant impact on the efficiency which is showed through the variations of single and double donor dyes. Recent published papers are working on the investigation of the DSSCs with the Graphene Quantum Dots (GQDs), as an incorporated layer inside the structure[311, 312, 313, 314]. Early results until now are showing the great perspective for this kind of an approach. Dyes performance is improved in the sense of the higher oscillator strengths and better light harvesting efficiency (LHE), while the combination with the semiconductor is still an open question and is currently the subject of an ongoing research. Our group is also heading at that direction, together with the hope that the local hybrid functionals can significantly help in order to improve the accuracy of the DFT and LR-TDDFT calculations.

Work on the apatite systems discovered a differentiation in Raman bands in respect to the different orientations of the initial signal and that the presence of the surface phonons can be decisive up to a nanometer size. Parallel oriented laser in respect to the sample are showing the strongest sensitivity at the phosphate and carbonate groups, while perpendicular orientation is showing almost

no bands. The IR and Raman spectra can accurately measure and show shifts in the bands due to the presence of a surface phonons and their behaviour can be divided and detected in comparison to the one in the bulk. The phonons at the surface are found to be shifted to both, higher and lower wavelengths, which is different from the predictions that it should be found only at the lower wavelengths regions. Also, phonons are very important and have significant inflence even when the sample is just a few nanometres thick. These findings represent an important part of a bone regeneration which is still a great mystery in scientific community. Bone structures and minerals are diverse with age which can lead to a serious diseases and non-apatitic environment. As a primary mineral in toot enamel and matrix in bones (around 70% of mass), hydroxyapatite is responsible for a several major parts in our body, such as the strength of the bones and its structure, bone mineralization as a support for the vital organs and toot enamel in order to protect our oral cavity and teeth form the bacteria. Today, it is one of the most used mineral in biomedical applications through bone and dental implants which helps in the bone replacement and regeneration in medicine.

References

[1] P. Hohenberg and W. Kohn. Inhomogeneous electron gas. *Phys. Rev.*, 136:B864–B871, Nov 1964.

[2] W. Kohn and L. J. Sham. Self-consistent equations including exchange and correlation effects. *Phys. Rev.*, 140:A1133–A1138, Nov 1965.

[3] Brian O'Regan and Michael Grätzel. A low-cost, high-efficiency solar cell based on dye-sensitized colloidal titanium-dioxide films. *Nature*, 353:1476–4687, October 1991.

[4] Jozef Szlufcik, S. Sivothaman, and J.F. Nijs. Low cost industrial technologies of crystalline silicon solar cells. *Prac. H. of Photovoltaics: Fund. and App.*, 01 2003.

[5] Michael Grätzel. Solar energy conversion by dye-sensitized photovoltaic cells. *Inorganic Chemistry*, 44(20):6841–6851, 2005. PMID: 16180840.

[6] Michael Grätzel. Dye-sensitized solar cells. *J. of Photochem. and Photobio. C: Photochem. Rev.*, 4(2):145–153, 2003.

[7] Anders Hagfeldt, Gerrit Boschloo, Licheng Sun, Lars Kloo, and Henrik Pettersson. Dye-sensitized solar cells. *Chem. Rev.*, 110(11):6595–6663, 2010. PMID: 20831177.

[8] Gong Jiawei, K. Sumathy, Qiao Qiquan, and Zhou Zhengping. Review on dye-sensitized solar cells (dsscs): Advanced techniques and research trends. *Rene. and Sust. E. Rev.*, 68:234–246, 2017.

[9] Filippo De Angelis, Cristiana Di Valentin, Simona Fantacci, Andrea Vittadini, and Annabella Selloni. Theoretical studies on anatase and less common tio2 phases: Bulk, surfaces, and nanomaterials. *Chem. Rev.*, 114(19):9708–9753, 2014. PMID: 24926899.

[10] Tetsuro Kono, Toshiro Sakae, Hiroshi Nakada, Takashi Kaneda, and Hiroyuki Okada. Confusion between carbonate apatite and biological apatite (carbonated hydroxyapatite) in bone and teeth. *Minerals*, 12(2), 2022.

[11] Hong Zhuang, Arif A. Baig, Jeffrey L. Fox, Zeren Wang, Shane J. Colby, Anil Chhettry, and William I. Higuchi. Metastable equilibrium solubility behavior of carbonated apatites in the presence of solution fluoride. *J. of Colloid and Interface Sci.*, 222(1):90–96, 2000.

[12] Fuzeng Ren, Yonghui Ding, and Yang Leng. Infrared spectroscopic characterization of carbonated apatite: A combined experimental and computational study. *J. of Biomed. Mat. Res. Part A*, 102(2):496–505, 2014.

[13] E. Schrödinger. An undulatory theory of the mechanics of atoms and molecules. *Phys. Rev.*, 28:1049–1070, Dec 1926.

[14] Max Born and Robert Oppenheimer. Zur quantentheorie der molekeln. *Annalen der Physik*, 389(20):457–484, 1927.

[15] Viktor N. Staroverov. *Density-Functional Approximations for Exchange and Correlation*, chapter 6, pages 125–156. John Wiley and Sons, Ltd, 2012.

[16] John C. Slater. A simplification of the hartree-fock method. *Phys. Rev.*, 34(10):1293–1322, 1929.

[17] Douglas R. Hartree. The calculation of atomic structures. *Proc. of the Cam. Philo. Soc.*, 24(3):89–110, 1928.

[18] L. H. Thomas. The calculation of atomic fields. *Math. Proc. of the Cam. Philo. Soc.*, 23(5):542–548, 1927.

[19] E. Fermi. Un metodo statistico per la determinazione di alcune priorieta dell'atome. *Rendiconti della R. Accademia dei Lincei*, 6(6):602–607, 1927.

[20] J. P. Perdew, K. Burke, and M. Ernzerhof. Generalized gradient approximation made simple. *Phys. Rev. L.*, 77(18):3865–3868, 1996.

[21] A. D. Becke. Density-functional thermochemistry. iii. the role of exact exchange. *The J. of Chem. Phys.*, 98(7):5648–5652, 1993.

[22] Matthias Ernzerhof and Gustavo E. Scuseria. Assessment of the perdew–burke–ernzerhof exchange-correlation functional. *The J. of Chem. Phys.*, 110(11):5029–5036, 1999.

[23] D.R. Hartree. The wave mechanics of an atom with a non-coulomb central field. part i. theory and methods. *Math. Proc. of the Cam. Philo. Soc.*, 24(1):89–110, 1928.

[24] D.R. Hartree. The wave mechanics of an atom with a non-coulomb central field. part ii. some results and discussion. *Math. Proc. of the Cam. Philo. Soc.*, 24(1):111–132, 1928.

[25] J.P. Perdew and A. Zunger. Self-interaction correction to density-functional approximations for many-electron systems. *Phys. Rev. B*, 23(10):5048–5079, 1981.

[26] J.P. Perdew, J.A. Chevary, S.H. Vosko, K.A. Jackson, M.R. Pederson, D.J. Singh, and C. Fiolhais. Atoms, molecules, solids, and surfaces: Applications of the generalized gradient approximation for exchange and correlation. *Phys. Rev. B*, 46(11):6671–6687, 1992.

[27] J. Tao, J.P. Perdew, V.N. Staroverov, and G.E. Scuseria. Climbing the density functional ladder: Nonempirical meta-generalized gradient approximation designed for molecules and solids. *Phys. Rev. L.*, 91(14):146401, 2003.

[28] Kieron Burke. Perspective on density functional theory. *The J. of Chem. Phys.*, 136(15), apr 2012.

[29] Daan Frenkel and Berend Smit. *Understanding molecular simulation: from algorithms to applications.* Elsevier, 2023.

[30] John P. Perdew, Adrienn Ruzsinszky, Gábor I. Csonka, Oleg A. Vydrov, Gustavo E. Scuseria, Lucian A. Constantin, Xiaolan Zhou, and Kieron Burke. Restoring the density-gradient expansion for exchange in solids and surfaces. *Phys. Rev. Lett.*, 100:136406, Apr 2008.

[31] Federico G. Cruz, Kin Lam, and Kieron Burke. Exchange-correlation energy density from virial theorem. *J. of Phys. Chem. A*, 102:4911–4917, 1998.

[32] Juanita Jaramillo, Gustavo E. Scuseria, and Matthias Ernzerhof. Local hybrid functionals. *The J. of Chem. Phys.*, 118(3):1068–1073, 01 2003.

[33] Toni M. Maier, Alexei V. Arbuznikov, and Martin Kaupp. Local hybrid functionals: Theory, implementation, and performance of an emerging new tool in quantum chemistry and beyond. *WIREs Comp. Mol. Sc.*, 9(1):e1378, 2019.

[34] Mark E. Casida. Time-dependent density-functional theory for molecules and molecular solids. *J. of Mol. Structure: THEOCHEM*, 914(1):3–18, 2009.

[35] Erich Runge and E. K. U. Gross. Density-functional theory for time-dependent systems. *Phys. Rev. Lett.*, 52:997–1000, Mar 1984.

[36] Michael J. G. Peach, Peter Benfield, Trygve Helgaker, and David J. Tozer. Excitation energies in density functional theory: An evaluation and a diagnostic test. *The J. of Chem. Phys.*, 128(4):044118, 01 2008.

[37] Mark E. Casida. Propagator corrections to adiabatic time-dependent density-functional theory linear response theory. *The J. of Chem. Phys.*, 122(5):054111, 01 2005.

[38] Zhendong Li and Wenjian Liu. Critical assessment of td-dft for excited states of open-shell systems: I. doublet–doublet transitions. *J. of Chem. Theory and Comp.*, 12(1):238–260, 2016. PMID: 26672389.

[39] K. Yabana and G. F. Bertsch. Time-dependent local-density approximation in real time. *Phys. Rev. B*, 54:4484–4487, Aug 1996.

[40] Jeppe Olsen and Poul Jørgensen. Time-dependent response theory with applications to self-consistent field and multiconfigurational self-consistent field wave functions. In *Modern Electronic Structure Theory: Part II*, pages 857–990. World Scientific, 1995.

[41] Toni M. Maier, Hilke Bahmann, and Martin Kaupp. Efficient Semi-numerical Implementation of Global and Local Hybrid Functionals for Time-Dependent Density Functional Theory. *J. Chem. Theory Comput.*, 11(9):4226–4237, 2015.

[42] Miquel Huix-Rotllant, Nicolas Ferré, and Mario Barbatti. *Time-Dependent Density Functional Theory*, chapter 2, pages 13–46. John Wiley and Sons, Ltd, 2020.

[43] Luísa Andrade, Helena Aguilar Ribeiro, and Adélio Mendes. *Dye–Sensitized Solar Cells: An Overview.* John Wiley and Sons, Ltd, 2011.

[44] Bin Li, Liduo Wang, Bonan Kang, Peng Wang, and Yong Qiu. Review of recent progress in solid-state dye-sensitized solar cells. *S. E. Mat. and Solar Cells*, 90(5):549–573, 2006.

[45] T. Nejat Veziroglu. 21st century's energy: Hydrogen energy system. In John W. Sheffield and Çiğdem Sheffield, editors, *Assessment of Hydrogen Energy for Sustainable Development*, pages 9–31, Dordrecht, 2007. Springer Netherlands.

[46] Brian Seger. Global energy consumption: The numbers for now and in the future, 2016. Senest ændret: 23/09/2016.

[47] Daryl M Chapin, Calvin S Fuller, and Gerald L Pearson. A new silicon p-n junction photocell for converting solar radiation into electrical power. *J. of App. Phys.*, 25(5):676–677, 1954.

[48] Jingjing Liu, Yao Yao, Shaoqing Xiao, and Xiaofeng Gu. Review of status developments of high-efficiency crystalline silicon solar cells. *J. of Phys. D: App. Phys.*, 51(12):123001, feb 2018.

[49] Simon Mathew, Aswani Yella, Peng Gao, Robin Humphry-Baker, Basile Curchod, Negar Astani, Ivano Tavernelli, Ursula Rothlisberger, Mohammad Nazeeruddin, and Michael Grätzel. Dye-sensitized solar cells with 13% efficiency achieved through the molecular engineering of porphyrin sensitizers. *Nature chemistry*, 6:242–7, 03 2014.

[50] Norasikin A. Ludin, A.M. Al-Alwani Mahmoud, Abu Bakar Mohamad, Abd. Amir H. Kadhum, Kamaruzzaman Sopian, and Nor Shazlinah Abdul Karim. Review on the development of natural dye photosensitizer for dye-sensitized solar cells. *Ren. and Sus. E. Rev.*, 31:386–396, 2014.

[51] Dongshe Zhang, Suzanne M. Lanier, Jonathan A. Downing, Jason L. Avent, June Lum, and Jeanne L. McHale. Betalain pigments for dye-sensitized solar cells. *J. of Photochem. and Photobio. A: Chemistry*, 195(1):72–80, 2008.

[52] Valeriy Kavun, Merkulov Evgeny, L. Ignat'eva, and Vladimir Goncharuk. Ionic mobility and structure of glasses based on indium and bismuth fluorides from data of ir and19f nmr spectroscopy. *Glass Phys. and Chem.*, 26:199–201, 03 2000.

[53] Umer Mehmood, Saleem-ur Rahman, K. Harrabi, Ibnelwaleed Hussein, and B. Reddy. Recent advances in dye sensitized solar cells. *Ad. in Mat. Sc. and Eng.*, 2014:1–12, 04 2014.

[54] Lupan Oleg, V.M. Guérin, Ion Tiginyanu, Veaceslav Ursaki, Lee Chow, and Helge Heinrich. Vertically-oriented well-aligned zno nanowires arrays electrodeposited on ito-coated glass and their integration in dye-sensitized solar cells. *J. of Photochem. and Photobio. A: Chem.*, 211:65–73, 03 2010.

[55] Deok-Woo Han, Jongkyu Heo, Dong Joo Kwak, Chi-Hwan Han, and Youl Moon Sung. Texture, morphology and photovoltaic characteristics of nanoporous f:sno$_2$ films. *J. of El. Eng. & Tech.*, 4:93–97, 2009.

[56] Yosuke Fukai, Yusuke Kondo, Shogo Mori, and Eiji Suzuki. Highly efficient dye-sensitized sno2 solar cells having sufficient electron diffusion length. *Electrochem. Comm.*, 9(7):1439–1443, 2007.

[57] Christophe Bauer, Gerrit Boschloo, Emad Mukhtar, and Anders Hagfeldt. Ultrafast studies of electron injection in ru dye sensitized sno2 nanocrystalline thin film. *Int. J. of Photoen.*, 4, 01 2002.

[58] Marcos Fernández-García and José A. Rodriguez. *Metal Oxide Nanoparticles.* John Wiley and Sons, Ltd, 2011.

[59] Hua Yu, Shanqing Zhang, Huijun Zhao, Bofei Xue, Porun Liu, and Geoffrey Will. High-performance tio2 photoanode with an efficient electron transport network for dye-sensitized solar cells. *The J. of Phys. Chem. C*, 113(36):16277–16282, 2009.

[60] Mingkui Wang, Carole Grätzel, Shaik Zakeeruddin, and Michael Grätzel. Recent developments in redox electrolytes for dye-sensitized solar cells. *Ene. and Env. Sc.*, 5, 10 2012.

[61] Jiayan Cong, Xichuan Yang, Yan Hao, Lars Kloo, and Licheng Sun. A highly efficient colourless sulfur/iodide-based hybrid electrolyte for dye-sensitized solar cells. *RSC Advances*, 2:3625–3629, 04 2012.

[62] Sambandam Anandan. Recent improvements and arising challenges in dye-sensitized solar cells. *Solar Ene. Mat. and Solar Cells*, 91(9):843–846, 2007.

[63] Muna Don, Piyasiri Ekanayake, Hideki Nakajima, Abdul Mahadi, Chee Lim, and Affiz Atod. Acetylene carbon black-graphite composite as low-cost and efficient counter electrode for dye-sensitized solar cells (dsscs). *Ionics*, 25, 11 2019.

[64] D. Kishore Kumar, Sanjay Kumar Swami, Viresh Dutta, Baixin Chen, Nick Bennett, and H.M. Upadhyaya. Scalable screen-printing manufacturing process for graphene oxide platinum free alternative counter electrodes in efficient dye sensitized solar cells. *FlatChem*, 15:100105, 2019.

[65] Moisés Amâncio, Ellen Raphael, Yonny Romaguera Barcelay, Maria Oneide Silva-Moraes, Camila Ruzo, Raimundo Passos, and Walter Brito. Natural dyes from amazon forest: potential application in dye-sensitized solar cells. *Matéria (Rio de Janeiro)*, 26, 05 2021.

[66] Mariachiara Pastore and Filippo De Angelis. *Modeling Materials and Processes in Dye-Sensitized Solar Cells: Understanding the Mechanism, Improving the Efficiency*, pages 151–236. Springer Berlin Heidelberg, Berlin, Heidelberg, 2014.

[67] Won Rho, Hojin Jeon, Ho-Sub Kim, Woo-Jae Chung, Jung Suh, and Bong-Hyun Jun. Recent progress in dye-sensitized solar cells for improving efficiency: Tio 2 nanotube arrays in active layer. *J. of Nanomat.*, 2015:1–17, 03 2015.

[68] Soni D., P. Parsoya, B. K Menariya, Vyas R., and R. Ameta. Photoelectrochemical cells, solar energy convers. storage. *Photochem. Modes 414*, 2015:29–53, 11 2015.

[69] Laurent Lasser, Enrico Ronca, Mariachiara Pastore, Filippo De Angelis, Jérôme Cornil, Roberto Lazzaroni, and David Beljonne. Energy level alignment at titanium oxide–dye interfaces: Implications for electron injection and light harvesting. *The J. of Phys. Chem. C*, 119(18):9899–9909, 2015.

[70] Juan Bisquert and Francisco Fabregat-Santiago. Impedance spectroscopy: a general introduction and application to dye-sensitized solar cells. In *Dye-sensitized solar cells*, pages 477–574. EPFL Press, 2010.

[71] Kankatala S.V. Gupta, Ji Zhang, Gabriele Marotta, Marri Anil Reddy, Surya Prakash Singh, Ashraful Islam, Liyuan Han, Filippo De Angelis, Malapaka Chandrasekharam, and Mariachiara Pastore. Effect of the anchoring group in the performance of carbazole-phenothiazine dyads for dye-sensitized solar cells. *Dyes and Pigments*, 113:536–545, 2015.

[72] Enrico Ronca, Mariachiara Pastore, Leonardo Belpassi, Francesco Tarantelli, and Filippo De Angelis. Influence of the dye molecular structure on the tio2 conduction band in dye-sensitized solar cells: disentangling charge transfer and electrostatic effects. *Energy Environ. Sc.*, 6:183–193, 2013.

[73] Mariachiara Pastore, Edoardo Mosconi, and Filippo De Angelis. Computational investigation of dye–iodine interactions in organic dye-sensitized solar cells. *The J. of Phys. Chem. C*, 116(9):5965–5973, 2012.

[74] Volodymyr Turkowski, Naseem Ud Din, and Talat S. Rahman. Time-dependent density-functional theory and excitons in bulk and two-dimensional semiconductors. *Computation*, 5(3), 2017.

[75] Frédéric Labat, Tangui Le Bahers, Ilaria Ciofini, and Carlo Adamo. First-principles modeling of dye-sensitized solar cells: Challenges and perspectives. *Acc. of Chem. Res.*, 45(8):1268–1277, 2012. PMID: 22497694.

[76] Daniel R. Jones and Alessandro Troisi. A method to rapidly predict the charge injection rate in dye sensitized solar cells. *Phys. Chem. Chem. Phys.*, 12:4625–4634, 2010.

[77] Oleg V. Prezhdo, Walter R. Duncan, and Victor V. Prezhdo. Dynamics of the photoexcited electron at the chromophore–semiconductor interface. *Acc. of Chem. Res.*, 41(2):339–348, 2008. PMID: 18281950.

[78] Filippo De Angelis, Simona Fantacci, and Annabella Selloni. Alignment of the dye's molecular levels with the titanium-dioxide band edges in dye-sensitized solar cells: a dft–tddft study. *Nanotechnology*, 19(42):424002, sep 2008.

[79] Tangui Le Bahers, Thierry Pauporté, Giovanni Scalmani, Carlo Adamo, and Ilaria Ciofini. A td-dft investigation of ground and excited state properties in indoline dyes used for dye-sensitized solar cells. *Phys. Chem. Chem. Phys.*, 11:11276–11284, 2009.

[80] Denis Jacquemin, Eric A. Perpète, Gustavo E. Scuseria, Ilaria Ciofini, and Carlo Adamo. Td-dft performance for the visible absorption spectra of organic dyes: Conventional versus long - range hybrids. *J. of Chem. Theory and Comp.*, 4(1):123–135, 2008. PMID: 26619986.

[81] Denis Jacquemin, Tangui Le Bahers, Carlo Adamo, and Ilaria Ciofini. What is the "best" atomic charge model to describe through-space charge-transfer excitations? *Phys. Chem. Chem. Phys.*, 14:5383–5388, 2012.

[82] Mariachiara Pastore, Simona Fantacci, and Filippo De Angelis. Modeling excited states and alignment of energy levels in dye-sensitized solar cells: Successes, failures, and challenges. *The J. of Phys. Chem. C*, 117(8):3685–3700, 2013.

[83] Noa Marom, Jonathan E. Moussa, Xinguo Ren, Alexandre Tkatchenko, and James R. Chelikowsky. Electronic structure of dye-sensitized tio_2 clusters from many-body perturbation theory. *Phys. Rev. B*, 84:245115, Dec 2011.

[84] P. Umari, L. Giacomazzi, F. De Angelis, M. Pastore, and Stefano Baroni. Energy-level alignment in organic dye-sensitized TiO2 from GW calculations. *The J. of Chem. Phys.*, 139(1):014709, 07 2013.

[85] Alekos Segalina, Sébastien Lebègue, Dario Rocca, Simone Piccinin, and Mariachiara Pastore. Structure and energetics of dye-sensitized nio interfaces in water from ab initio md and large-scale gw calculations. *J. of Chem. Theory and Comp.*, 17(8):5225–5238, 2021. PMID: 34324810.

[86] Joshua D Elliott, Edoardo Mosconi, Filippo De Angelis, Alberto Ambrosetti, and Paolo Umari. Real space–real time evolution of excitonic states based on the bethe-salpeter equation method. *The J. of Phys. Chem. L.*, 12(30):7261–7269, 2021. PMID: 34314589.

[87] Daniel Escudero, Ivan Duchemin, Xavier Blase, and Denis Jacquemin. Modeling the photochrome–tio2 interface with bethe–salpeter and time-dependent density functional theory methods. *The J. of Phys. Chem. L.*, 8(5):936–940, 2017. PMID: 28178780.

[88] Margherita Marsili, Edoardo Mosconi, Filippo De Angelis, and Paolo Umari. Large-scale gw-bse calculations with N^3 scaling: Excitonic effects in dye-sensitized solar cells. *Phys. Rev. B*, 95:075415, Feb 2017.

[89] Carla Verdi, Edoardo Mosconi, Filippo De Angelis, Margherita Marsili, and P. Umari. Alignment of energy levels in dye/semiconductor interfaces by gw calculations: Effects due to coadsorption of solvent molecules. *Phys. Rev. B*, 90:155410, Oct 2014.

[90] Noa Marom, Thomas Körzdörfer, Xinguo Ren, Alexandre Tkatchenko, and James R. Chelikowsky. Size effects in the interface level alignment of dye-sensitized tio2 clusters. *The J. of Phys. Chem. L.*, 5(14):2395–2401, 2014. PMID: 26277805.

[91] Denis Jacquemin, Ivan Duchemin, and Xavier Blase. Benchmarking the bethe–salpeter formalism on a standard organic molecular set. *J. of Chem. Theory and Comp.*, 11(7):3290–3304, 2015. PMID: 26207104.

[92] Christopher E. Patrick and Feliciano Giustino. Quantitative analysis of valence photoemission spectra and quasiparticle excitations at chromophore-semiconductor interfaces. *Phys. Rev. Lett.*, 109:116801, Sep 2012.

[93] Piotr de Silva and Clémence Corminboeuf. Local hybrid functionals with orbital-free mixing functions and balanced elimination of self-interaction error. *The J. of Chem. Phys.*, 142(7):074112, 02 2015.

[94] Eli Kraisler, Tobias Schmidt, Stephan Kümmel, and Leeor Kronik. Effect of ensemble generalization on the highest-occupied Kohn-Sham eigenvalue. *The J. of Chem. Phys.*, 143(10):104105, 09 2015.

[95] John P. Perdew, Viktor N. Staroverov, Jianmin Tao, and Gustavo E. Scuseria. Density functional with full exact exchange, balanced nonlocality of correlation, and constraint satisfaction. *Phys. Rev. A*, 78:052513, Nov 2008.

[96] Hilke Bahmann, Alexander Rodenberg, Alexei V. Arbuznikov, and Martin Kaupp. A thermochemically competitive local hybrid functional without gradient corrections. *The J. of Chem. Phys.*, 126(1):011103, 01 2007.

[97] Tamotsu Horiuchi, Hidetoshi Miura, and Satoshi Uchida. Highly-efficient metal-free organic dyes for dye-sensitized solar cells. *ChemInform*, 35(15), 2004.

[98] Matthias Batzill. Fundamental aspects of surface engineering of transition metal oxide photocatalysts. *Energy Environ. Sci.*, 4:3275–3286, 2011.

[99] Mariachiara Pastore and Filippo De Angelis. Computational modelling of tio2 surfaces sensitized by organic dyes with different anchoring groups: adsorption modes, electronic structure and implication for electron injection/recombination. *Phys. Chem. Chem. Phys.*, 14:920–928, 2012.

[100] Natalia Martsinovich, Daniel R. Jones, and Alessandro Troisi. Electronic structure of tio2 surfaces and effect of molecular adsorbates using different dft implementations. *The J. of Phys. Chem. C*, 114(51):22659–22670, 2010.

[101] Axel D. Becke. A new mixing of Hartree–Fock and local density-functional theories. *The J. of Chem. Phys.*, 98(2):1372–1377, 01 1993.

[102] Hilke Bahmann. From global to local – hybrid density functionals for weak and strong correlation. In *Chemical Modelling: Volume 16*. The Royal Soc. of Chem., 05 2021.

[103] Andreas Dreuw, Jürgen Plötner, Michael Wormit, Martin Head-Gordon, and Anthony Dean Dutoi. An additive long-range potential to correct for the charge-transfer failure of time-dependent density functional theory. *Zeitschrift für Physikalische Chemie*, 224(3-4):311–324, 2010.

[104] Andreas Dreuw and Martin Head-Gordon. Failure of time-dependent density functional theory for long-range charge-transfer excited states the zincbacteriochlorinbacteriochlorin and bacteriochlorophyllspheroidene complexes. *J. of the Ame. Chem. Soc.*, 126(12):4007–4016, 2004. PMID: 15038755.

[105] Andreas Dreuw, Jennifer L. Weisman, and Martin Head-Gordon. Long-range charge-transfer excited states in time-dependent density functional theory require non-local exchange. *The J. of Chem. Phys.*, 119(6):2943–2946, 07 2003.

[106] A. Karolewski, T. Stein, R. Baer, and S. Kümmel. Communication: Tailoring the optical gap in light-harvesting molecules. *The J. of Chem. Phys.*, 134(15):151101, 04 2011.

[107] Alexei V. Arbuznikov, Hilke Bahmann, and Martin Kaupp. Local hybrid functionals with an explicit dependence on spin polarization. *The J. of Phys. Chem. A*, 113(43):11898–11906, 2009. PMID: 19848429.

[108] Alexei V. Arbuznikov and Martin Kaupp. Local hybrid exchange-correlation functionals based on the dimensionless density gradient. *Chem. Phys. L.*, 440(1):160–168, 2007.

[109] Martin Kaupp, Hilke Bahmann, and Alexei V. Arbuznikov. Local hybrid functionals: An assessment for thermochemical kinetics. *The J. of Chem. Phys.*, 127(19):194102, 11 2007.

[110] Tobias Schmidt and Stephan Kümmel. One- and many-electron self-interaction error in local and global hybrid functionals. *Phys. Rev. B*, 93:165120, Apr 2016.

[111] Toni M. Maier, Hilke Bahmann, Alexei V. Arbuznikov, and Martin Kaupp. Validation of local hybrid functionals for TDDFT calculations of electronic excitation energies. *The J. of Chem. Phys.*, 144(7):074106, 02 2016.

[112] Tobias Schmidt, Eli Kraisler, Leeor Kronik, and Stephan Kümmel. One-electron self-interaction and the asymptotics of the kohn–sham potential: an impaired relation. *Phys. Chem. Chem. Phys.*, 16:14357–14367, 2014.

[113] Alexei V. Arbuznikov and Martin Kaupp. Importance of the correlation contribution for local hybrid functionals: Range separation and self-interaction corrections. *The J. of Chem. Phys.*, 136(1):014111, 01 2012.

[114] Pedro Borlido, Miguel A. L. Marques, and Silvana Botti. Local hybrid density functional for interfaces. *J. of Chem. Theory and Comp.*, 14(2):939–947, 2018. PMID: 29227686.

[115] Gunter Hermann and Jean Christophe Tremblay. Ultrafast photoelectron migration in dye-sensitized solar cells: Influence of the binding mode and many-body interactions. *The J. of Chem. Phys.*, 145:174704, 11 2016.

[116] Stefan Klinkusch and Jean Christophe Tremblay. Resolution-of-identity stochastic time-dependent configuration interaction for dissipative electron dynamics in strong fields. *The J. of Chem. Phys.*, 144(18):184108, 05 2016.

[117] Pascal Krause, Jean Christophe Tremblay, and Annika Bande. Atomistic simulations of laser-controlled exciton transfer and stabilization in symmetric double quantum dots. *The J. of Phys. Chem. A*, 125(22):4793–4804, 2021. PMID: 34047560.

[118] Jean Christophe Tremblay, Tillmann Klamroth, and Peter Saalfrank. Time-dependent configuration-interaction calculations of laser-driven dynamics in presence of dissipation. *The J. of Chem. Phys.*, 129:084302, 09 2008.

[119] Jean Christophe Tremblay, Pascal Krause, Tillmann Klamroth, and Peter Saalfrank. Time-dependent response of dissipative electron systems. *Phys. Rev. A*, 81:063420, Jun 2010.

[120] Jean Christophe Tremblay, Stefan Klinkusch, Tillmann Klamroth, and Peter Saalfrank. Dissipative many-electron dynamics of ionizing systems. *The J. of Chem. Phys.*, 134(4):044311, 01 2011.

[121] G. Lindblad. On the generators of quantum dynamical semigroups. *Commun. Math. Phys.*, 48:119, 1976.

[122] Vittorio Gorini, Andrzej Kossakowski, and E. C. G. Sudarshan. Completely positive dynamical semigroups of N-level systems. *J. of Math. Phys.*, 17(5):821–825, 08 2008.

[123] Vittorio Gorini and Andrzej Kossakowski. N-level system in contact with a singular reservoir. *J. of Math. Phys.*, 17(7):1298–1305, 08 2008.

[124] G. Hermann and J. C. Tremblay. Laser-driven hole trapping in a ge/si core–shell nanocrystal: An atomistic configuration interaction perspective. *The J. of Phys. Chem. C*, 119(45):25606–25614, 2015.

[125] Fabian Weber, Jean Christophe Tremblay, and Annika Bande. Proton-coupled electron-transfer dynamics of water oxidation at n-doped graphene oxides. *The J. of Phys. Chem. C*, 124(49):26688–26698, 2020.

[126] Jean Christophe Tremblay and Tucker Carrington. Using preconditioned adaptive step size runge-kutta methods for solving the time-dependent schrödinger equation. *The J. of Chem. Phys.*, 121:11535–41, 01 2005.

[127] Jean Christophe Tremblay and Peter Saalfrank. Guided locally optimal control of quantum dynamics in dissipative environments. *Phys. Rev. A*, 78:063408, Dec 2008.

[128] Sree Ganesh Balasubramani, Guo P. Chen, Sonia Coriani, Michael Diedenhofen, Marius S. Frank, Yannick J. Franzke, Filipp Furche, Robin Grotjahn, Michael E. Harding, Christof Hättig, Arnim Hellweg, Benjamin Helmich-Paris, Christof Holzer, Uwe Huniar, Martin Kaupp, Alireza Marefat Khah, Sarah Karbalaei Khani, Thomas Müller, Fabian Mack, Brian D. Nguyen, Shane M. Parker, Eva Perlt, Dmitrij Rappoport, Kevin Reiter, Saswata Roy, Matthias Rückert, Gunnar Schmitz, Marek Sierka, Enrico Tapavicza, David P. Tew, Christoph van Wüllen, Vamsee K. Voora, Florian Weigend, Artur Wodyński, and Jason M. Yu. TURBOMOLE: Modular program suite for ab initio quantum-chemical and condensed-matter simulations. *The J. of Chem. Phys.*, 152(18):184107, 05 2020.

[129] Carlo Adamo and Vincenzo Barone. Toward reliable density functional methods without adjustable parameters: The PBE0 model. *The J. of Chem. Phys.*, 110(13):6158–6170, 04 1999.

[130] A new hybrid exchange–correlation functional using the coulomb-attenuating method (cam-b3lyp). *Chem. Phys. L.*, 393(1):51–57, 2004.

[131] Ansgar Schäfer, Hans Horn, and Reinhart Ahlrichs. Fully optimized contracted Gaussian basis sets for atoms Li to Kr. *The J. of Chem. Phys.*, 97(4):2571–2577, 08 1992.

[132] Oliver Treutler and Reinhart Ahlrichs. Efficient molecular numerical integration schemes. *The J. of Chem. Phys.*, 102(1):346–354, 01 1995.

[133] Gunter Hermann, Vincent Pohl, Jean Christophe Tremblay, Beate Paulus, Hans-Christian Hege, and Axel Schild. Orbkit: A modular python toolbox for cross-platform postprocessing of quantum chemical wavefunction data. *J. of Comp. Chem.*, 37(16):1511–1520, 2016.

[134] Vincent Pohl, Gunter Hermann, and Jean Christophe Tremblay. An open-source framework for analyzing n-electron dynamics. i. multideterminantal wave functions. *J. of Comp. Chem.*, 38(17):1515–1527, 2017.

[135] Gunter Hermann, Vincent Pohl, and Jean Christophe Tremblay. An open-source framework for analyzing n-electron dynamics. ii. hybrid density functional theory/configuration interaction methodology. *J. of Comp. Chem.*, 38(28):2378–2387, 2017.

[136] L. Schmidt-Mende, U. Bach, R. Humphry-Baker, T. Horiuchi, H. Miura, S. Ito, S. Uchida, and M. Grätzel. Organic dye for highly efficient solid-state dye-sensitized solar cells. *Adv. Materials*, 17(7):813–815, 2005.

[137] Lingamallu Giribabu, Ravi Kumar Kanaparthi, and Veerapandian Velkannan. Molecular engineering of sensitizers for dye-sensitized solar cell applications. *The Chem. Record*, 12(3):306–328, 2012.

[138] L. Kavan, M. Grätzel, S. E. Gilbert, C. Klemenz, and H. J. Scheel. Electrochemical and photoelectrochemical investigation of single-crystal anatase. *J. of the Am. Chem. Soc.*, 118(28):6716–6723, 1996.

[139] Jochen Heyd and Gustavo E. Scuseria. Efficient hybrid density functional calculations in solids: Assessment of the Heyd–Scuseria–Ernzerhof screened Coulomb hybrid functional. *The J. of Chem. Phys.*, 121(3):1187–1192, 07 2004.

[140] Kerstin Hummer, Judith Harl, and Georg Kresse. Heyd-scuseria-ernzerhof hybrid functional for calculating the lattice dynamics of semiconductors. *Phys. Rev. B*, 80:115205, Sep 2009.

[141] Miguel A. L. Marques, Julien Vidal, Micael J. T. Oliveira, Lucia Reining, and Silvana Botti. Density-based mixing parameter for hybrid functionals. *Phys. Rev. B*, 83:035119, Jan 2011.

[142] Yanhong Luo, Dongmei Li, and Qingbo Meng. Towards optimization of materials for dye-sensitized solar cells. *Adv. Mater.*, 21(45):4647–4651, 2009.

[143] Zhaoyang Yao, Min Zhang, Heng Wu, Lin Yang, Renzhi Li, and Zhepeng Wang. A donor-acceptor indenoperylene dye for highly efficient organic dye-sensitized solar cells. *J. Amer. Chem. Soc.*, 137, 03 2015.

[144] Zhijun Ning, Qiong Zhang, Wenjun Wu, Hongcui Pei, Bo Liu, and He Tian. Starburst triarylamine based dyes for efficient dye-sensitized solar cells. *The J. of Org. Chem.*, 73(10):3791–3797, 2008. PMID: 18412319.

[145] Panpan Dai, Lin Yang, Mao Liang, Huanhuan Dong, Peng Wang, Chunyao Zhang, Zhe Sun, and Song Xue. Influence of the terminal electron donor in d–d-π–a organic dye-sensitized solar cells: dithieno [3, 2-b: 2', 3'-d] pyrrole versus bis (amine). *ACS App. Mat. & Interfaces*, 7(40):22436–22447, 2015. PMID: 26394089.

[146] Zhongquan Wan, Chunyang Jia, Yandong Duan, Linlei Zhou, Yuan Lin, and Yu Shi. Phenothiazine-triphenylamine based organic dyes containing various conjugated linkers for efficient dye-sensitized solar cells. *J. Mater. Chem.*, 22(48):25140–25147, 2012.

[147] Chundan Lin, Yanbing Liu, Di Shao, Guochen Wang, Huiying Xu, Changjin Shao, Wansong Zhang, and Zhenqing Yang. Density functional theory design of double donor dyes and electron transfer on dye/TiO_2(101) composite systems for dye-sensitized solar cells. *RSC Adv.*, 11(5):3071–3078, 2021.

[148] Mark E. Casida, Christine Jamorski, Kim C. Casida, and Dennis R. Salahub. Molecular excitation energies to high-lying bound states from time-dependent density-functional response theory. characterization and correction of the time-dependent local density approximation ionization threshold. *J. Chem. Phys.*, 108(11):4439–4449, 1998.

[149] D. Gemeri, J. C. Tremblay, M. Pastore, and H. Bahmann. Electronic structure, optical properties, and electron dynamics in organic dye-sensitized TiO_2 interfaces by local hybrid density functionals. *Chem. Phys.*, 559(March):111521, 2022.

[150] Filipp Furche and Reinhart Ahlrichs. Adiabatic time-dependent density functional methods for excited state properties. *The J. of Chem. Phys.*, 117(16):7433–7447, 2002.

[151] Marcus Hanwell, Donald Curtis, David Lonie, Tim Vandermeersch, Eva Zurek, and Geoffrey Hutchison. Avogadro: an advanced semantic chemical editor, visualization, and analysis platform. *J. Cheminform.*, 4:17, 08 2012.

[152] Koichi Momma and Fujio Izumi. VESTA 3 for three-dimensional visualization of crystal, volumetric and morphology data. *J. Appl. Cryst.*, 44(6):1272–1276, 2011.

[153] Vitaly A. Rassolov, John A. Pople, Mark A. Ratner, and Theresa L. Windus. 6-31g* basis set for atoms k through zn. *J. Chem. Phys.*, 109(4):1223–1229, 1998.

[154] Chengteh Lee, Weitao Yang, and Robert G. Parr. Development of the Colle-Salvetti correlation-energy formula into a functional of the electron density. *Phys. Rev. B*, 37(2):785–789, 1 1988.

[155] Oliver Treutler and Reinhart Ahlrichs. Efficient molecular numerical integration schemes. *J. Chem. Phys.*, 102(1):346–354, 1995.

[156] Hilke Bahmann and Martin Kaupp. Efficient Self-Consistent Implementation of Local Hybrid Functionals. *J. Chem. Theory Comput.*, 11(4):1540–1548, 2015.

[157] Mariachiara Pastore. First principle modelling of materials and processes in dye-sensitized photoanodes for solar energy and solar fuels. *Computation*, 5(1), 2017.

[158] J. C. Tremblay, P. Krause, T. Klamroth, and P. Saalfrank. The effect of energy and phase relaxation on dynamic polarizability calculations. *Phys. Rev. A*, 81:063420:1–10, 2010.

[159] Susanne Fuerst, Matthias Haasler, Robin Grotjahn, and Martin Kaupp. Full implementation, optimization, and evaluation of a range-separated local hybrid functional with wide accuracy for ground and excited states. *J. Chem. Theory Comput.*, 19(2):488–502, 2023.

[160] Moritz Brütting, Hilke Bahmann, and Stephan Kümmel. Hybrid functionals with local range separation: Accurate atomization energies and reaction barrier heights. *J. Chem. Phys.*, 156(10):104109, 2022.

[161] Sascha Klawohn and Hilke Bahmann. Self-consistent implementation of hybrid functionals with local range separation. *J. Chem. Theory Comput.*, 16(2):953–963, 2020.

[162] Toshiro Sakae, Hiroshi Nakada, and John Legeros. Historical review of biological apatite crystallography. *J. of Hard Tissue Bio.*, 24:111–122, 04 2015.

[163] WF Bale, HC Hodge, and SL Warren. Roentgenray diffraction studies of enamel and dentin. *Am. J. of Roentgenology and Radium Therapy*, 32(3):369–376, 1934.

[164] Otto R. Trautz. X-ray diffraction of biological and synthetic apatites. *Annals of the New York Academy of Sci.*, 60(4):697–712, 1955.

[165] M. I. Kay, R. A. Young, and A. S. Posner. Crystal structure of hydroxyapatite. *Nature*, 204(4963):1050–1053, 1964.

[166] K. Sudarsanan and R. A. Young. Significant precision in crystal structure details: Holly springs hydroxyapatite. *Acta Crystall. Sec. B*, 25(8):1534–1543, 1969.

[167] Robert A. Young and Peter E. Mackie. Crystallography of human tooth enamel: initial structure refinement. *Materials Res. Bulletin*, 15(12):1729, 1980.

[168] Sergey V. Dorozhkin. Calcium orthophosphates in nature, biology and medicine. *Materials*, 2(2):399–498, 2009.

[169] M. Epple, K. Ganesan, R. Heumann, J. Klesing, A. Kovtun, S. Neumann, and V. Sokolova. Application of calcium phosphate nanoparticles in biomedicine. *J. Mater. Chem.*, 20:18–23, 2010.

[170] Sergey V. Dorozhkin. Am. j. biomed. eng. *Am. J. of Biomed. Eng.*, 2:48–97, 2012.

[171] Hiroaki Suda, Masatomo Yashima, Masato Kakihana, and Masahiro Yoshimura. J. phys. chem. *J. of Phys. Chem.*, 99:6752–6754, 1995.

[172] Vuk Uskoković and Dragan P. Uskoković. Nanosized hydroxyapatite and other calcium phosphates: Chemistry of formation and application as drug and gene delivery agents. *J. of Biomed. Mat. Res. Part B: App. Biomat.*, 96B(1):152–191, 2011.

[173] V. S. Bystrov, E. Paramonova, Yu Dekhtyar, A. Katashev, A. Karlov, N. Polyaka, A. V. Bystrova, A. Patmalnieks, and A. L. Kholkin. Computational and experimental studies of size and shape related physical properties of hydroxyapatite nanoparticles. *J. of Phys.: Condensed Matter*, 23(6):065302, 2011.

[174] J. C. Elliot. *Structure and Chemistry of the Apatites and Other Calcium Phosphates.* Elsevier, Amsterdam, 1994.

[175] J. C. Elliott, P. E. Mackie, and R. A. Young. Monoclinic hydroxyapatite. *Science*, 180(4090):1055–1057, 1973.

[176] Toshiyuki Ikoma, Atsushi Yamazaki, Satoshi Nakamura, and Masaru Akao. Preparation and structure refinement of monoclinic hydroxyapatite. *J. of Solid State Chem.*, 144(2):272–276, 1999.

[177] Guobin Ma and Xiang Yang Liu. Hydroxyapatite: Hexagonal or monoclinic? *Crystal Growth & Design*, 9(7):2991–2994, 2009.

[178] Dirk Zahn and Oliver Hochrein. The role of substitutional defects in orderdisorder phenomena of ohions in hydroxyapatite. *Zeitschrift für anorganische und allgemeine Chemie*, 632(1):79–83, 2006.

118

[179] J. M. Hughes, M. Cameron, and K. D. Crowley. Am. mineral. *American Mineralogist*, 74:870–876, 1989.

[180] Duncan McConnell. *Physical Properties*, pages 11–16. Springer Vienna, Vienna, 1973.

[181] Marie-José Dallemagne and Lucien J. Richelle. Inorganic chemistry of bone. In Ira Zipkin, editor, *Biological Mineralization*, pages 23–42. Wiley Interscience, John Wiley & Sons, New York, 1973.

[182] R. A. D. Williams and J. C. Elliott. *Basic and applied dental biochemistry / R. A. D. Williams, J. C. Elliott.* Churchill Livingstone ; distributed by Longman Edinburgh ; New York : New York, 1979.

[183] Wojciech L Suchanek, Pavel Shuk, Kullaiah Byrappa, Richard E Riman, Kevor S TenHuisen, and Victor F Janas. Mechanochemical-hydrothermal synthesis of carbonated apatite powders at room temperature. *Biomaterials*, 23(3):699—710, February 2002.

[184] Guillaume Penel, Guillaume Leroy, Christian Rey, and et al. Microraman spectral study of the po4 and co3 vibrational modes in synthetic and biological apatites. *Calcified Tissue Int.*, 63(5):475–481, 1998.

[185] Dejan Gemeri, Aleksandar Živković, I. Lukačević, Hilke Bahmann, and Helen King. Density functional theory demonstrates orientation effects in the raman spectra of hydroxy- and carbonated apatite. *J. of Raman Spec.*, 54, 10 2022.

[186] Aleksandar Živković, Dejan Gemeri, Hilke Bahmann, Igor Lukačević, and Helen King. Identifying surface phonons in the vibrational spectra of carbonated apatite using density functional theory. *Mat. Today Comm.*, 36:106596, 07 2023.

[187] William C. Herapath. On the power of bodies to radiate heat at different temperatures. *Philosophical Magazine*, 61(353):359–365, 1822.

[188] Robert W. Wood. Infrared spectroscopy and the structure of organic compounds. *Chem. Rev.*, 37(2):95–115, 1945.

[189] Sir C. V. Raman and K. S. Krishnan. A new type of secondary radiation. *Nature*, 121(3048):501–502, 1928.

[190] Peter Larkin. Chapter 2 - basic principles. In Peter Larkin, editor, *Infrared and Raman Spectroscopy*, pages 7–25. Elsevier, Oxford, 2011.

[191] R. McWeeny and C. A. Coulson. Quantum mechanics of the anharmonic oscillator. *Math. Proc. of the Cam. Philo. Soc.*, 44(3):413–422, 1948.

[192] David O. Harris, Gail G. Engerholm, and William D. Gwinn. Calculation of Matrix Elements for One-Dimensional Quantum-Mechanical Problems and the Application to Anharmonic Oscillators. *The J. of Chem. Phys.*, 43(5):1515–1517, 05 2004.

[193] F M Fernandez and R Guardiola. Accurate eigenvalues and eigenfunctions for quantum-mechanical anharmonic oscillators. *J. of Phys. A: Mathe. and General*, 26(23):7169, dec 1993.

[194] Alan Campion. *Raman Spectroscopy*, pages 345–415. Springer US, Boston, MA, 1987.

[195] Frank L. Pedrotti and Leno M. Pedrotti. *Introduction to Optics.* Prentice Hall, 1993.

[196] Max Born and Emil Wolf. *Principles of Optics: Electromagnetic Theory of Propagation, Interference and Diffraction of Light.* Cambridge University Press, 2013.

[197] David J. Griffiths. *Introduction to Quantum Mechanics.* Cambridge University Press, 2018.

[198] Masamichi Tsuboi, João Marcelo Benevides, and George J Jr. Thomas. Raman tensors and their application in structural studies of biological systems. *Proc. Phys. Biol. Sci.*, 85(3):83–97, 2009.

[199] Tetsuro Kono, Toshiro Sakae, Hiroshi Nakada, Takashi Kaneda, and Hiroyuki Okada. Confusion between carbonate apatite and biological apatite (carbonated hydroxyapatite) in bone and teeth. *Minerals*, 12(2), 2022.

[200] A. A. Baig, J. L. Fox, J. Hsu, Z. Wang, M. Otsuka, W. I. Higuchi, and R. Z. LeGeros. J. colloid interface sci. 179:608, 1996.

[201] John D. P. McElderry, Peizhi Zhu, Kamal H. Mroue, Jingwei Xu, Barbara Pavan, Meiyue Fang, Ge Zhao, Erin McNerny, David H. Kohn, Renny T. Franceschi, Mark M. B. Holl, Mary M. J. Tecklenburg, Ayyalusamy Ramamoorthy, and Michael D. Morris. Crystallinity and compositional changes in carbonated apatites: Evidence from ^{31}P solid-state NMR, Raman, and AFM analysis. *J. of Solid State Chem.*, 206:192–198, 2013.

[202] Sergio Bertazzo, Eileen Gentleman, Kristy L. Cloyd, Adrian H. Chester, Magdi H. Yacoub, and Molly M. Stevens. Nano-analytical electron microscopy reveals fundamental insights into human cardiovascular tissue calcification. *Nature Materials*, 12(6):576–583, June 2013.

[203] Adele L. Boskey and Richard Mendelsohn. Infrared analysis of bone in health and disease. *J. of Biomed. Optics*, 10(3):031102–0311029, 2005.

[204] Bo Wan, Rui Wang, Yuyu Sun, Jing Cao, Hongjun Wang, Jia Guo, and Dongsheng Chen. Frontiers in bioengineering and biotechnology. *Front. in Bioeng. and Biotech.*, 8:1176, 2020.

[205] Takuya Ishimoto, Takayoshi Nakano, Yukichi Umakoshi, Masaya Yamamoto, and Yasuhiko Tabata. Degree of biological apatite c-axis orientation rather than bone mineral density controls mechanical function in bone regenerated using recombinant bone morphogenetic protein-2. *J. of Bone and Mineral Research*, 28(5):1170–1179, 2013.

[206] Brigitte Wopenka and Jill D. Pasteris. A mineralogical perspective on the apatite in bone. *Mat. Sci. and Engin.: C*, 25(2):131–143, 2005. NATO Advanced Study Institute (ASI on Learning from Nature How to design New Implantable Biomaterials: From Biomineralization Fundamentals to Biomimetic Materials and Processing Routes).

[207] Metin Kazanci, H. Daniel Wagner, I. N. Manjubala, Himadri S. Gupta, Eleftherios Paschalis, Paul Roschger, and Peter Fratzl. Raman imaging of two orthogonal planes within cortical bone. *Bone*, 41(3):456–461, 2007.

[208] Jeffry S Nyman, Alexander J Makowski, Chetan A Patil, T Philip Masui, Elizabeth C O'Quinn, Xiaohong Bi, Scott A Guelcher, Daniel P Nicollela, and Anita Mahadevan-Jansen. Measuring differences in compositional properties of bone tissue by confocal raman spectroscopy. *Calcified tissue Int.*, 89(2):111—122, August 2011.

[209] Sonja Gamsjaeger, Admir Masic, Paul Roschger, Metin Kazanci, John W. C. Dunlop, Klaus Klaushofer, Eleftherios P. Paschalis, and Peter Fratzl. Cortical bone composition and orientation as a function of animal and tissue age in mice by raman spectroscopy. *Bone*, 47(2):392–399, 2010.

[210] Mekhala Raghavan, Nirit D. Sahar, Robert H. Wilson, Mary-Ann Mycek, Nancy Pleshko, David H. Kohn, and Michael D. Morris. Quantitative polarized raman spectroscopy in highly turbid bone tissue. *J. of Biomed. Optics*, 15(3):037001, 2010.

[211] Elizabeth A. Taylor, Christopher J. Mileti, Subhashree Ganesan, and et al. Measures of bone mineral carbonate content and mineral maturity/crystallinity for ft-ir and raman spectroscopic imaging differentially relate to physical–chemical properties of carbonate-substituted hydroxyapatite. *Calcified Tissue Int.*, 109:77–91, 2021.

[212] Karen Esmonde-White and Francis Esmonde-White. *Raman spectroscopy in biomineralization*, pages 59–71. 03 2014.

[213] Pavel Matousek, Edward R. C. Draper, Allen E. Goodship, Ian P. Clark, Kate L. Ronayne, and Anthony W. Parker. Noninvasive raman spectroscopy of human tissue in vivo. *App. Spec.*, 60(7):758–763, 2006. PMID: 16854263.

[214] Kevin Buckley, Jemma G. Kerns, Helen L. Birch, Panagiotis D. Gikas, Anthony W. Parker, Pavel Matousek, and Allen E. Goodship. Functional

adaptation of long bone extremities involves the localized "tuning" of the cortical bone composition; evidence from raman spectroscopy. *J. of Biomed. Optics*, 19(11):111602–111602, May 2014.

[215] G. Leroy, G. Penel, N. Leroy, and E. Brès. Human tooth enamel: A raman polarized approach. *Appl. Spectrosc.*, 56(8):1030–1034, Aug 2002.

[216] H. Tsuda and J. Arends. Orientational micro-raman spectroscopy on hydroxyapatite single crystals and human enamel crystallites. *J. of Dental Res.*, 73(11):1703–1710, 1994.

[217] Marios Georgiadis, Ralph Müller, and Philipp Schneider. Techniques to assess bone ultrastructure organization: orientation and arrangement of mineralized collagen fibrils. *J. of The Royal Soc. Interface*, 13(119):20160088, 2016.

[218] Camila de Carvalho Almança Lopes, Pedro Henrique Justino Oliveira Limirio, Veridiana Resende Novais, and Paula Dechichi. Fourier transform infrared spectroscopy (ftir) application chemical characterization of enamel, dentin and bone. *App. Spec. Rev.*, 53:747 – 769, 2018.

[219] Guy Daculsi, Jean Menanteau, Louis-Marie Kerebel, and et al. Length and shape of enamel crystals. *Calcified Tissue Int.*, 36:550–555, 1984.

[220] Jill D. Pasteris, Brigitte Wopenka, Joseph J. Freeman, Kay Rogers, Eugenia Valsami-Jones, Justin A. M. van der Houwen, and Martin J. Silva. Lack of OH in nanocrystalline apatite as a function of degree of atomic order: Implications for bone and biomaterials. *Biomaterials*, 25(2):229–238, 2004.

[221] Roberto Dovesi, Roberto Orlando, Alessandro Erba, Claudio M. Zicovich-Wilson, Bartolomeo Civalleri, Silvia Casassa, Lorenzo Maschio, Matteo Ferrabone, Marco De La Pierre, Philippe D'Arco, Yves Noël, Mauro Causà, Michel Rérat, and Bernard Kirtman. Crystal14: A program for the ab initio investigation of crystalline solids. *Int. J. of Q. Chem.*, 114(19):1287–1317, 2014.

[222] Roberto Dovesi, Alessandro Erba, Roberto Orlando, Claudio M. Zicovich-Wilson, Bartolomeo Civalleri, Lorenzo Maschio, Michel Rérat, Silvia Casassa, Jacopo Baima, Simone Salustro, and Bernard Kirtman. Quantum-mechanical condensed matter simulations with crystal. *WIREs Comp. Mol. Sci.*, 8(4):e1360, 2018.

[223] Loredana Valenzano, Fernando J. Torres, Klaus Doll, Fabien Pascale, Claudio M. Zicovich-Wilson, and Roberto Dovesi. Ab initio study of the vibrational spectrum and related properties of crystalline compounds; the case of caco3 calcite. *Zeitschrift für Physikalische Chemie*, 220(7):893–912, 2006.

[224] Claudio M. Zicovich-Wilson, Alberto Bert, Carla Roetti, Roberto Dovesi, and Victor R. Saunders. Characterization of the electronic structure of crystalline compounds through their localized Wannier functions. *The J. of Chem. Phys.*, 116(3):1120–1127, 01 2002.

[225] Marta Corno, Claudia Busco, Bartolomeo Civalleri, and Piero Ugliengo. Periodic ab initio study of structural and vibrational features of hexagonal hydroxyapatite ca10(po4)6(oh) 2. *Phys. Chem. Chem. Phys. : PCCP*, 8:2464–72, 07 2006.

[226] C. Gatti, V. R. Saunders, and C. Roetti. Crystal field effects on the topological properties of the electron density in molecular crystals: The case of urea. *The J. of Chem. Phys.*, 101(12):10686–10696, 12 1994.

[227] M. Catti, A. Pavese, R. Dovesi, and V. R. Saunders. Static lattice and electron properties of mgco$_3$ (magnesite) calculated by ab initio periodic hartree-fock methods. *Phys. Rev. B*, 47:9189–9198, Apr 1993.

[228] R. Dovesi, C. Roetti, C. Freyria-Fava, M. Prencipe, and V.R. Saunders. On the elastic properties of lithium, sodium and potassium oxide. an ab initio study. *Chem. Phys.*, 156(1):11–19, 1991.

[229] Lorenzo Maschio, Bernard Kirtman, Michel Rérat, Roberto Orlando, and Roberto Dovesi. Comment on "Ab initio analytical infrared intensities for periodic systems through a coupled perturbed Hartree-Fock/Kohn-Sham method" [J. Chem. Phys. 137, 204113 (2012)]. *The J. of Chem. Phys.*, 139(16):167101, 10 2013.

[230] R. Dovesi, B. Kirtman, L. Maschio, J. Maul, F. Pascale, and M. Rérat. Calculation of the infrared intensity of crystalline systems. a comparison of three strategies based on berry phase, wannier function, and coupled-perturbed kohn–sham methods. *The J. of Phys. Chem. C*, 123(13):8336–8346, 2019.

[231] Lorenzo Maschio, Bernard Kirtman, Michel Rérat, Roberto Orlando, and Roberto Dovesi. Ab initio analytical raman intensities for periodic systems through a coupled perturbed hartree-fock/kohn-sham method in an atomic orbital basis. ii. validation and comparison with experiments. *The J. of Chem. Phys.*, 139(16):164102, 2013.

[232] Marta Corno, Claudia Busco, Vera Bolis, Sergio Tosoni, and Piero Ugliengo. Water adsorption on the stoichiometric (001) and (010) surfaces of hydroxyapatite: A periodic b3lyp study. *Langmuir*, 25(4):2188–2198, 2009. PMID: 19161264.

[233] Gianfranco Ulian and Giovanni Valdrè. Effect of mechanical stress on the raman and infrared bands of hydroxylapatite: A quantum mechanical first principle investigation. *J. of the Mech. Behavior of Biomed. Mat.*, 77:683–692, 2018.

[234] Gianfranco Ulian, Giovanni Valdre, Marta Corno, and Piero Ugliengo. Periodic ab initio bulk investigation of hydroxylapatite and type a carbonated apatite with both pseudopotential and all-electron basis sets for calcium atoms. *Am. Mineralogist*, 98:410–416, 02 2013.

[235] Gianfranco Ulian, Giovanni Valdrè, Marta Corno, and Piero Ugliengo. Dft investigation of structural and vibrational properties of type b and mixed a-b carbonated hydroxylapatite. *Am. Mineralogist*, 99(1):117–127, 2014.

[236] Fabien Pascale, Sergio Tosoni, Claudio Zicovich-Wilson, Piero Ugliengo, Roberto Orlando, and Roberto Dovesi. Vibrational spectrum of brucite, mg(oh) 2: A periodic ab initio quantum mechanical calculation including oh anharmonicity. *Chem. Phys. L.*, 396:308–315, 10 2004.

[237] Piero Ugliengo, Fabien Pascale, Mohammadou Mérawa, Pierre Labéguerie, Sergio Tosoni, and Roberto Dovesi. Infrared spectra of hydrogen-bonded ionic crystals: Ab initio study of mg(oh)2 and be(oh)2. *The J. of Phys. Chem. B*, 108(36):13632–13637, 2004.

[238] Stefan Grimme, Jens Antony, Stephan Ehrlich, and Helge Krieg. A consistent and accurate ab initio parametrization of density functional dispersion correction (DFT-D) for the 94 elements H-Pu. *The J. of Chem. Phys.*, 132(15):154104, 2010.

[239] Stefan Grimme, Stephan Ehrlich, and Lars Goerigk. Effect of the damping function in dispersion corrected density functional theory. *J. of Comp. Chem.*, 32:1456–1465, 2011.

[240] Stefan Grimme, Andreas Hansen, Jan Gerit Brandenburg, and Christoph Bannwarth. Dispersion-corrected mean-field electronic structure methods. *Chem. Rev.*, 116(9):5105–5154, 2016. PMID: 27077966.

[241] Vei Wang, Nan Xu, Jin-Cheng Liu, Gang Tang, and Wen-Tong Geng. VASPKIT: A user-friendly interface facilitating high-throughput computing and analysis using VASP code. *Computer Phys. Comm.*, 267:108033, oct 2021.

[242] Soumya S. Bhat, Umesh V. Waghmare, and Upadrasta Ramamurty. First-principles study of structure, vibrational, and elastic properties of stoichiometric and calcium-deficient hydroxyapatite. *Crystal Growth & Design*, 14(6):3131–3141, 2014.

[243] Fuzeng Ren, Xiong Lu, and Yang Leng. Ab initio simulation on the crystal structure and elastic properties of carbonated apatite. *J. of the Mech. Behavior of Biomed. Mat.*, 26:59–67, 2013.

[244] Dino Aquilano, Marco Bruno, Marco Rubbo, Francesco Roberto Massaro, and Linda Pastero. Low symmetry polymorph of hydroxyapatite. theoretical equilibrium morphology of the monoclinic ca5(oh)(po4)3. *Crystal Growth & Design*, 14(6):2846–2852, 2014.

[245] Bartolomeo Civalleri, Claudio M. Zicovich-Wilson, Loredana Valenzano, and Piero Ugliengo. B3lyp augmented with an empirical dispersion term (b3lyp-d*) as applied to molecular crystals. *CrystEngComm*, 10:405–410, 2008.

[246] Gianfranco Ulian, Giovanni Valdrè, Marta Corno, and Piero Ugliengo. The vibrational features of hydroxylapatite and type a carbonated apatite: A first principle contribution. *Am. Mineralogist*, 98(4):752–759, 2013.

[247] Z. Iqbal, V.P. Tomaselli, O. Fahrenfeld, K.D. Möller, F.A. Ruszala, and E. Kostiner. Polarized raman scattering and low frequency infrared study of hydroxyapatite. *J. of Phys. and Chem. of Solids*, 38(8):923–927, 1977.

[248] Francesca Peccati, Marta Corno, Massimo Delle Piane, Gianfranco Ulian, Piero Ugliengo, and Giovanni Valdrè. Co32– mobility in carbonate apatite as revealed by density functional modeling. *The J. of Phys. Chem. C*, 118:1364–1369, 12 2013.

[249] K. benataya, M. Lakrat, L.L. Elansari, and E. Mejdoubi. Synthesis of b-type carbonated hydroxyapatite by a new dissolution-precipitation method. *Mat. Today: Proceedings*, 31:S83–S88, 2020. International Conference on Advanced Materials, Nanosciences and Applications Training School in Spectroscopies for Environment and Nanochemistry.

[250] Mathilde Granke, Aurélien Gourrier, Fabienne Rupin, Kay Raum, Françoise Peyrin, Manfred Burghammer, Amena Saïed, and Pascal Laugier. Microfibril orientation dominates the microelastic properties of human bone tissue at the lamellar length scale. *PLOS ONE*, 8(3):1–11, 03 2013.

[251] Daniel Jaschouz, Oskar Paris, Paul Roschger, Hae-Sook Hwang, and Peter Fratzl. Pole figure analysis of mineral nanoparticle orientation in individual trabecula of human vertebral bone. *J. of App. Crystall.*, 36(3 Part 1):494–498, Jun 2003.

[252] Noboru Sasaki, Norio Matsushima, Takeshi Ikawa, Hisao Yamamura, and Akira Fukuda. Orientation of bone mineral and its role in the anisotropic mechanical properties of bone–transverse anisotropy. *J. of Biomech.*, 22(2):157–164, 1989.

[253] Metin Kazanci, Paul Roschger, Eleftherios P. Paschalis, Klaus Klaushofer, and Peter Fratzl. Bone osteonal tissues by raman spectral mapping: Orientation-composition. *J. of Struc. Biology*, 156(3):489–496, 2006.

[254] Yuichi Takano, Charles H. Turner, and David B. Burr. Mineral anisotropy in mineralized tissues is similar among species and mineral growth occurs independently of collagen orientation in rats: Results from acoustic velocity measurements. *J. of Bone and Mineral Res.*, 11(9):1292–1301, 1996.

[255] Guillaume Falgayrac, Sébastien Facq, Gérard Leroy, Bernard Cortet, and Guillaume Penel. New method for raman investigation of the orientation of collagen fibrils and crystallites in the haversian system of bone. *Appl. Spectrosc.*, 64(7):775–780, Jul 2010.

[256] Mikael J. Turunen, Jørgen D. Kaspersen, Ulf Olsson, Manuel Guizar-Sicairos, Martin Bech, Florian Schaff, Simone E. Hieber, Alberto Bravin, Franz Pfeiffer, Jesper S. Thomsen, and Hanna Isaksson. Bone mineral crystal size and organization vary across mature rat bone cortex. *J. of Struc. Biology*, 195(3):337–344, 2016.

[257] S. Chatterji, J. C. Wall, and J. W. Jeffery. Age-related changes in the orientation and particle size of the mineral phase in human femoral cortical bone. *Calcified Tissue Int.*, 33:567–574, 1981.

[258] Wilfried Tesch, Tabitha Vandenbos, Paul Roschger, Nadja Fratzl-Zelman, Klaus Klaushofer, Wim Beertsen, and Peter Fratzl. Orientation of mineral crystallites and mineral density during skeletal development in mice deficient in tissue nonspecific alkaline phosphatase. *J. of Bone and Mineral Res.*, 18(1):117–125, 2003.

[259] Michael D. Morris and Gurjit S. Mandair. Raman assessment of bone quality. *Clinical Orthopaedics and Related Res.*, 469(8):2160–2169, August 2011.

[260] Helen E. King, Dorothea C. Mattner, Oliver Plümper, Thorsten Geisler, and Andrew Putnis. Forming cohesive calcium oxalate layers on marble surfaces for stone conservation. *Crystal Growth & Design*, 14(8):3910–3917, 2014.

[261] Ramana M. Pidaparti, Arun Chandran, Yuichi Takano, and Charles H. Turner. Bone mineral lies mainly outside collagen fibrils: Predictions of a composite model for osteonal bone. *J. of Biomech.*, 29(7):909–916, 1996.

[262] Akinwande Awonusi, Michael D. Morris, and Mary M. J. Tecklenburg. Carbonate assignment and calibration in the raman spectrum of apatite. *Calcified Tissue Int.*, 81(1):46–52, 2007.

[263] Helen E. King, Steven M. Tommasini, Alejandro B. Rodriguez-Navarro, Brandon Q. Mercado, and H. Catherine W. Skinner. Correlative vibrational spectroscopy and 2D X-ray diffraction to probe the mineralization of bone in phosphate-deficient mice. *J. of App. Crystall.*, 52(5):960–971, Oct 2019.

[264] Mengmeng Wang, Rui Qian, Min Bao, Chenxi Gu, and Peizhi Zhu. Raman, ft-ir and xrd study of bovine bone mineral and carbonated apatites with different carbonate levels. *Materials L.*, 210:203–206, 2018.

[265] Gyunggoo Cho, Yaotang Wu, and Jerome L. Ackerman. Detection of hydroxyl ions in bone mineral by solid-state nmr spectroscopy. *Science*, 300(5622):1123–1127, 2003.

[266] Athanasios Antonakos, Evangelos Liarokapis, and Theodora Leventouri. Micro-raman and ftir studies of synthetic and natural apatites. *Biomaterials*, 28(19):3043–3054, 2007.

[267] Gianfranco Ulian, Daniele Moro, and Giovanni Valdrè. Hydroxylapatite and related minerals in bone and dental tissues: Structural, spectroscopic and mechanical properties from a computational perspective. *Biomolecules*, 11(5):728, 2021.

[268] C. Rey, B. Collins, T. Goehl, I. R. Dickson, and M. J. Glimcher. The carbonate environment in bone mineral: A resolution-enhanced fourier transform infrared spectroscopy study. *Calcified Tissue Int.*, 45(3):157–164, 1989.

[269] M.S. Amin, L.K. Randeniya, A. Bendavid, P.J. Martin, and E.W. Preston. Biomimetic apatite growth from simulated body fluid on various oxide containing dlc thin films. *Diamond and Related Mat.*, 21:42–49, 2012.

[270] Michele Bianchi, Alessandro Gambardella, Gabriela Graziani, Fabiola Liscio, Maria Cristina Maltarello, Marco Boi, Matteo Berni, Devis Bellucci, Gregorio Marchiori, Francesco Valle, Alessandro Russo, and Maurilio Marcacci. Plasma-assisted deposition of bone apatite-like thin films from natural apatite. *Materials L.*, 199:32–36, 2017.

[271] Hirofumi Miyaji, Ayako Oyane, and Aiko Narazaki. Biological modification of tooth surface by laser-based apatite coating techniques. *J. of Oral Biosciences*, 64(2):217–221, 2022.

[272] Ozlen F. Yasar, Wei-Chih Liao, Renny Mathew, Yang Yu, Baltzar Stevensson, Yihong Liu, Zhijian Shen, and Mattias Edén. The carbonate and sodium environments in precipitated and biomimetic calcium hydroxycarbonate apatite contrasted with bone mineral: Structural insights from solid-state nmr. *The J. of Phys. Chem. C*, 125(19):10572–10592, 2021.

[273] Eva Amenta, Helen E. King, Holger Petermann, Vuk Uskoković, Steven M. Tommasini, and Carolyn M. Macica. Vibrational spectroscopic analysis of hydroxyapatite in hyp mice and individuals with x-linked hypophosphatemia. *Therapeutic Adv. in Chronic Disease*, 9(12):268–281, 2018. PMID: 30719271.

[274] Carolyn M. Macica, Helen E. King, Meina Wang, Courtney L. McEachon, Catherine W. Skinner, and Steven M. Tommasini. Novel anatomic adaptation of cortical bone to meet increased mineral demands of reproduction. *Bone*, 85:59–69, 2016.

[275] C. Combes and C. Rey. Amorphous calcium phosphates: Synthesis, properties and uses in biomaterials. *Acta Biomaterialia*, 6(9):3362–3378, 2010.

[276] Stanislas Von Euw, Yimin Wang, Guillaume Laurent, Christophe Drouet, Florence Babonneau, Nadine Nassif, and Thierry Azaïs. Bone mineral: New insights into its chemical composition. *Sci. Reports*, 9(1):8456, 2019.

[277] Sandra M. Londoño-Restrepo, Luis F. Zubieta-Otero, Rodrigo Jeronimo-Cruz, Maria Antonieta Mondragon, and Mario E. Rodriguez-García. Effect of the crystal size on the infrared and raman spectra of bio hydroxyapatite of human, bovine, and porcine bones. *J. of Raman Spec.*, 50(8):1120–1129.

[278] Sandra M. Londoño-Restrepo, Rafael Jeronimo-Cruz, Beatriz M. Millán-Malo, and et al. Effect of the nano crystal size on the x-ray diffraction patterns of biogenic hydroxyapatite from human, bovine, and porcine bones. *Sci. Reports*, 9:5915, 2019.

[279] Akhilesh K. Arora, M. Rajalakshmi, T. R. Ravindran, and V. Sivasubramanian. Raman spectroscopy of optical phonon confinement in nanostructured materials. *J. of Raman Spec.*, 38(6):604–617, 2007.

[280] Furqan A. Shah. Towards refining raman spectroscopy-based assessment of bone composition. *Sci. Reports*, 10:16662, 2020.

[281] I.H. Campbell and P.M. Fauchet. The effects of microcrystal size and shape on the one phonon raman spectra of crystalline semiconductors. *Solid State Comm.*, 58(10):739–741, 1986.

[282] J. Muscat, A. Wander, and N.M. Harrison. On the prediction of band gaps from hybrid functional theory. *Chem. Phys. L.*, 342(3):397–401, 2001.

[283] Christine L. Bailey, Leandro Liborio, Giuseppe Mallia, Stanko Tomić, and Nicholas M. Harrison. Defect physics of $cugas_2$. *Phys. Rev. B*, 81:205214, May 2010.

[284] S. Tomić, B. Montanari, and N.M. Harrison. The group iii–v's semiconductor energy gaps predicted using the b3lyp hybrid functional. *Phys. E: Low-dimensional Systems and Nanost.*, 40(6):2125–2127, 2008.

[285] V. Gava, A. L. Martinotto, and C. A. Perottoni. First-principles mode gruneisen parameters and negative thermal expansion in $\alpha-zrw_2o_8$. *Phys. Rev. Lett.*, 109:195503, Nov 2012.

[286] Andrew D. Rowan, Charles H. Patterson, and L. V. Gasparov. Hybrid density functional theory applied to magnetite: Crystal structure, charge order, and phonons. *Phys. Rev. B*, 79:205103, May 2009.

[287] E. Talebian and M. Talebian. The calculation of the energies of phonon normal modes in the alpha-quartz crystal by analyzing the change of forces on atoms in the hydrogen-passivated small cluster of h16si7o6. *Optik*, 125(1):224–227, 2014.

[288] Lorenzo Maschio, Bernard Kirtman, Roberto Orlando, and Michel Rèrat. Ab initio analytical infrared intensities for periodic systems through a coupled perturbed hartree-fock/kohn-sham method. *J. of Chem. Phys.*, 137(20):204113, 2012.

[289] C. M. Zicovich-Wilson, F. Pascale, C. Roetti, V. R. Saunders, R. Orlando, and R. Dovesi. Calculation of the vibration frequencies of alfa-quartz: The effect of hamiltonian and basis set. *J. of Comp. Chem.*, 25(15):1873–1881, 2004.

[290] Alexander Stukowski. Visualization and analysis of atomistic simulation data with ovito–the open visualization tool. *Modelling and Sim. in Mat. Sci. and Eng.*, 18(1):015012, dec 2009.

[291] P W Tasker. The stability of ionic crystal surfaces. *J. of Phys. C: Solid State Phys.*, 12(22):4977, nov 1979.

[292] Marta Corno, Albert Rimola, Vera Bolis, and Piero Ugliengo. Hydroxyapatite as a key biomaterial: quantum-mechanical simulation of its surfaces in interaction with biomolecules. *Phys. Chem. Chem. Phys.*, 12:6309–6329, 2010.

[293] Michael E. Fleet. Infrared spectra of carbonate apatites: Region bands. *Biomaterials*, 30(8):1473–1481, 2009.

[294] K. C. BLAKESLEE and ROBERT A. CONDRATE SR. Vibrational spectra of hydrothermally prepared hydroxyapatites. *J. of the Am. Ceramic Soc.*, 54(11):559–563, 1971.

[295] H.D. Lutz and H. Haeuseler. Infrared and raman spectroscopy in inorganic solids research. *J. of Mol. Struc.*, 511-512:69–75, 1999.

[296] Helen King and Thorsten Geisler. Tracing mineral reactions using confocal raman spectroscopy. *Minerals*, 8(4):158, Apr 2018.

[297] Ki Dong Oh, J. Ranade, V. Arya, A. Wang, and R.O. Claus. Optical fiber fabry-perot interferometric sensor for magnetic field measurement. *IEEE Photonics Tech. L.*, 9(6):797–799, 1997.

[298] H. Chessin, W. C. Hamilton, and B. Post. Position and thermal parameters of oxygen atoms in calcite. *Acta Crystall.*, 18(4):689–693, Apr 1965.

[299] S. Osswald, V. N. Mochalin, M. Havel, G. Yushin, and Y. Gogotsi. Phonon confinement effects in the raman spectrum of nanodiamond. *Phys. Rev. B*, 80:075419, Aug 2009.

[300] Christian Rey, Masakazu Shimizu, Bill Collins, and Melvin J Glimcher. Resolution-enhanced fourier transform infrared spectroscopy study of the environment of phosphate ions in the early deposits of a solid phase of calcium-phosphate in bone and enamel, and their evolution with age. i: Investigations in the upsilon 4 po4 domain. *Calcified Tissue Int.*, 46(6):384–394, Jun 1990.

[301] Arunima Dey, Pauline HM Bomans, Frank A Müller, Jürgen Will, Peter M Frederik, Gijsbertus de With, and Nico AM Sommerdijk. The role of prenucleation clusters in surface-induced calcium phosphate crystallization. *Nature Materials*, 9(12):1010–1014, 2010.

[302] Vijay Kumar Mishra, Birendra Nath Bhattacharjee, Om Parkash, Devendra Kumar, and Shyam Bahadur Rai. Mg-doped hydroxyapatite nanoplates for biomedical applications: A surfactant assisted microwave synthesis and spectroscopic investigations. *J. of Alloys and Comp.*, 614:283–288, 2014.

[303] Mohamed Mathlouthi and Dang Vinh Luu. Laser-raman spectra of d-glucose and sucrose in aqueous solution. *Carbohydrate Res.*, 81(2):203–212, 1980.

[304] Durgalakshmi Dhinasekaran, Gobi Saravanan Kaliaraj, Mohanraj Jagannathan, Ajay Rakkesh Rajendran, Aruna Prakasarao, Singaravelu Ganesan, and Balakumar Subramanian. Pulsed laser deposition of nanostructured bioactive glass and hydroxyapatite coatings: Microstructural and electrochemical characterization. *Mat. Sci. and Eng.: C*, 130:112459, 2021.

[305] Elizabeth A. McNally, Henry P. Schwarcz, Gianluigi A. Botton, and A. Larry Arsenault. A model for the ultrastructure of bone based on electron microscopy of ion-milled sections. *PLOS ONE*, 7(1):1–12, 01 2012.

[306] H. Ou-Yang, E. P. Paschalis, W. E. Mayo, A. L. Boskey, and R. Mendelsohn. Infrared microscopic imaging of bone: Spatial distribution of co32. *J. of Bone and Mineral Res.*, 16(5):893–900, 2001.

[307] Luis F. Zubieta-Otero, Sandra M. Londoño-Restrepo, Gilberto Lopez-Chavez, Ezequiel Hernandez-Becerra, and Mario E. Rodriguez-Garcia. Comparative study of physicochemical properties of bio-hydroxyapatite with commercial samples. *Mat. Chem. and Phys.*, 259:124201, 2021.

[308] Anne B Barry, Abdul A Baig, Steven C Miller, and William I Higuchi. Effect of age on rat bone solubility and crystallinity. *Calcified Tissue Int.*, 71(2):167–171, Aug 2002.

[309] Christian Rey, V Renugopalakrishnan, Bill Collins, and Melvin J Glimcher. Fourier transform infrared spectroscopic study of the carbonate ions

in bone mineral during aging. *Calcified Tissue Int.*, 49(4):251–258, Oct 1991.

[310] Wei Tong, Melvin J Glimcher, Jerold L Katz, Liisa Kuhn, and Steven J Eppell. Size and shape of mineralites in young bovine bone measured by atomic force microscopy. *Calcified Tissue Int.*, 72(5):592–598, May 2003.

[311] Anjan Kumar, Sabah Auda Abdul Ameer, Sura Mohammad Mohealdeen, Ahmed Hasoon, Yousra Ali Abdulsayed, Abdelmajeed Adam Lagum, Alaa M. Al-Ma'abreh, and Mustafa M. Kadhim. Performance enhancement of dye-sensitized solar cells based on nitrogen-doped graphene quantum dots. *Comp. and Theoretical Chem.*, 1226:114180, 2023.

[312] Xiaoli Fang, Meiya Li, Kaimo Guo, Jun Li, Muchen Pan, Lihua Bai, Mengdai Luoshan, and Xingzhong Zhao. Graphene quantum dots optimization of dye-sensitized solar cells. *Electrochimica Acta*, 137:634–638, 2014.

[313] Feng Gao, Chuan-Lu Yang, Mei-Shan Wang, Xiao-Guang Ma, and Wen-Wang Liu. Theoretical insight on hybrid nanocomposites of graphene quantum dot and carbazole–carbazole dyes as an efficient sensitizer of dssc. *Spectrochimica Acta Part A: Molecular and Biomolecular Spectroscopy*, 216:69–75, 2019.

[314] Feng Gao, Chuan-Lu Yang, and Gang Jiang. Effects of the coupling between electrode and gqd-anthoxanthin nanocomposites for dye-sensitized solar cell: Dft and td-dft investigations. *J. of Photochem. and Photobio. A: Chem.*, 407:113080, 2021.